The Surface Electronic Structure of Y(0001)

A thesis submitted in accordance with the requirements of the

University of Liverpool

for the degree of

Doctor in Philosophy

by

Christopher Searle

of the

Surface Science Research Centre

December 1998

PAGE NUMBERING AS ORIGINAL

Abstract

Yttrium has been grown epitaxially on W(110). The growth was monitored by using photoemission spectroscopy with a synchrotron radiation source.

The film thickness has been gauged by the attenuation of the W 4f 7/2 bulk component. The films have been grown reproducibly and show a prominent surface state which is indicative of good order and low contamination

Angle-Resolved Ultra-Violet Photoemission Spectroscopy has been used to examine the valence band of these ultra-thin films. The films show a very different structure to the valence band of a bulk crystal of yttrium.

The differences have been investigated by a series of model calculations using the LMASA-46 tight-binding LMTO program. The calculations suggest that the ultra-thin film surface state may be hybridised with a tungsten orbital having $(x^2 - y^2)$ character.

Contents

page

Acknowledgements

The Buddha took a few leaves and asked his disciples "Which is more? These few leaves in my hand or the leaves in the forest over here?"

(They replied) "... very few are the leaves in the hand of the Blessed One, ... the leaves in the forest are very much more abundant."

"Even so, ... of what I have known I have told you only a little, what I have not told you is very much more. And why have I not told you those things? Because that is not useful ..."

W. Rahula,"What the Buddha Taught".

Amongst those that I have to thank for steering me through the darkest of thickets during my studies, the biggest thanks goes to my supervisor Steve Barrett, for his friendship as much as for his guidance, enthusiasm and generosity. Cheers Steve! I would also like to express my thanks to Daresbury's senior theorist, Paul Durham, for giving me the opportunity to see photoemission from a whole new angle. Next, I would like to thank those of the REG who showed me how to handle the tools: Rob Blyth, Sarnjeet Dhesi, Richard White, Myoung Ho Lee and Nigel Tucker. Truly great blokes, all round! Ohran Zeybek and Nasser Moslemzadah are to be thanked for keeping me sane during my write-up, and I am indebted to Colin Mason for his coding expertise, and for taking the trouble to proof-read this thesis. Lastly, I would like to thank John Murray and all at the Liverpool IRC who keep the place running smoothly. Amongst the theorists at Daresbury I would like to express my thanks to Walter Temmerman, Zdzislawa Szotek, Guang Y Guo and Arthur Ernst. Others who should be thanked include Eric Hines from Florida Atlantic University, Micheal Methfessel for tutoring me on his code at Trieste, and Claudio Verdozzi for helping me through the literature on many-body theory. Amongst the friends I made at Liverpool, a special thanks goes to Neil Brooks, Micheal Jackson and Nick Prince for some remarkably creative evenings. Lastly, I'd like to thank my mother for her constant support and I'd like to thank Lisa, my wife, for putting up with my desperate struggles to find those few leaves that I needed for this thesis. I'm glad we got through it together!

Chapter 1

Yttrium and Rare-Earth Metal Surfaces

The purpose of this chapter is to explain the motivation for this thesis, and to present a brisk overview of its study and organisation.

1.1 Introduction

The first question that can be asked of this thesis is: "What's so special about yttrium?" Named from the earth yttria, which was discovered by Gadolin in 1794 in a quarry close to the Swedish village of Ytterby, yttrium was first isolated by Mosander in 1843. Having the electronic configuration $[Kr](4d5s)^3$, yttrium lies in the 4d row of the transition metals beneath scandium, with its configuration $[Ar](3d4s)^3$, and above the strongly magnetic lanthanide series with their $[Xe]4f^x(5d6s)^y$ configurations, where $x = 0, 1, ..., 14$ and $y = 2, 3$.

Yttrium thus sits squarely in the domain of the transition metals and we can expect to understand its material properties, such as its room temperature hexagonal close packed (HCP) crystal structure, through the electronic structure of its bands - an approach which has proved successful in numerous studies of other transition metals [1.1, 1.2].

However, despite its apparent designation as a 4d metal, yttrium shares its chemistry more closely with scandium and the lanthanides, and together these elements comprise the rare-earth metals, a highly reactive chemical group that has posed problems in both experimental and

theoretical studies for over two hundred years.

Whilst the initial difficulties in rare-earth studies were experienced by metallurgists, whose struggles to isolate the individual members of the rare-earth family lasted into the early years of this century, in more recent years it has been the theorists who have laboured to understand the rôle of the 4f electrons in the lanthanide series. The lanthanides derive their strong magnetic character from the partial occupancy of the 4f shell, and the degree to which the 4f electrons can be considered to be delocalised (band-like), or localised (retaining their atomic orbital structure) is still undecided.

Yttrium is therefore very useful in rare-earth metal studies, since the absence of any 4f structure provides an effective measure for identifying the 4f related features in the electronic structure of the lanthanides. While this is also true for scandium and lanthanum, we shall see shortly that yttrium single crystals may be purified to a higher degree than these other metals.

Yttrium is also commercially important; its oxide is used in the europium phosphors that produce the red colour in television screens, and yttrium iron, aluminium and gadolinium garnets have found a variety of uses, most notably as microwave filters, acoustic transducers and synthetic gemstones. The discovery of the high temperature superconductor YBaCuO in 1987 suggests that future commercial avenues may be available to yttrium.

1.2 The Surfaces of Metals

One of the most remarkable properties of metal crystals is the regularity and stability of their structure. We can understand this through the usual gross approximation for a metal as a regular array of positively

charged ions immersed in a sea of valence electrons. It is through the interaction of the opposed electrical charges that we gain a repeating crystal structure, since this configuration secures a total energy minimum for the system when filling all space.

At the surface of a metal crystal, however, we find a unique environment; the subtle balance of forces that sustains the three dimensional crystal structure is broken, and a new equilibrium must be established.

The loss of symmetry at the surface invariably demands a new energy minimum to exist, and both the geometrical structure and the chemical activity of the crystal may change within the surface region. The exact extent of this surface region, however, is dependent on local bonding and since each crystal plane has its own local bonding criteria to satisfy, the extent of the surface is correlated with specific crystal faces.

The importance of these points cannot be over-stressed; the electronic structure of a crystal is intimately linked with its spatial symmetry and the reduced symmetry at the surface invariably leads to a new surface electronic structure.

1.3 Photoemission Spectroscopy

The electronic structure of matter can be explored experimentally by the technique of photoemission spectroscopy (PES), in which an electron is excited from a bound state with the assistance of a photon. To extract useful data from a photoemission experiment, it is obviously important that contamination is minimised. For surface electronic structure this is achieved when the experiment is performed in ultra-high vacuum (UHV). Since photons are only able to promote electron transitions with a probability that depends on the available electron

population, we are led to the naïve interpretation of PES which views photoemission as a mapping from the occupied density of states to the measured spectrum.

The different energy regimes for the photons, and the exact method used for electron detection, has given rise to a family of photoemission spectroscopies: ultraviolet (UPS) within the range 5-100 eV, soft x-ray (soft XPS) within the range 100-1000 eV, and x-ray (XPS) for energies above 1000 eV. The earliest photoemission spectroscopy was simply interested in the intensity of the emitted electrons as a function of the incident radiation, a technique which is now called angle-integrated PES. With the advent of single crystal studies came the first angle-resolved PES experiments that mapped the dispersion of electron states, and more recently [1.3], spin-resolved experiments have been probing magnetic structures by identifying the relative populations of electron spin states.

The most useful of these spectroscopies for surface electronic structure is UPS, because low binding-energy electrons that are excited over this range of energies are strongly scattered within the crystal, producing a short mean free path λ so that only the first few atomic layers can contribute electrons to the spectra (see figure 1.a, overleaf).

In order to interpret photoemission spectra more precisely and thus identify the origin of particular spectral features, we must assume a model behaviour for the electrons that is amenable to calculation. These calculated electronic structures are necessarily approximate and ultimately justified by their agreement with experiment. Consequently, we have a symbiosis of experiment and theory in the determination of electronic structure, and we expect this dual approach to converge towards actual electronic structures in an almost 'self-consistent' manner.

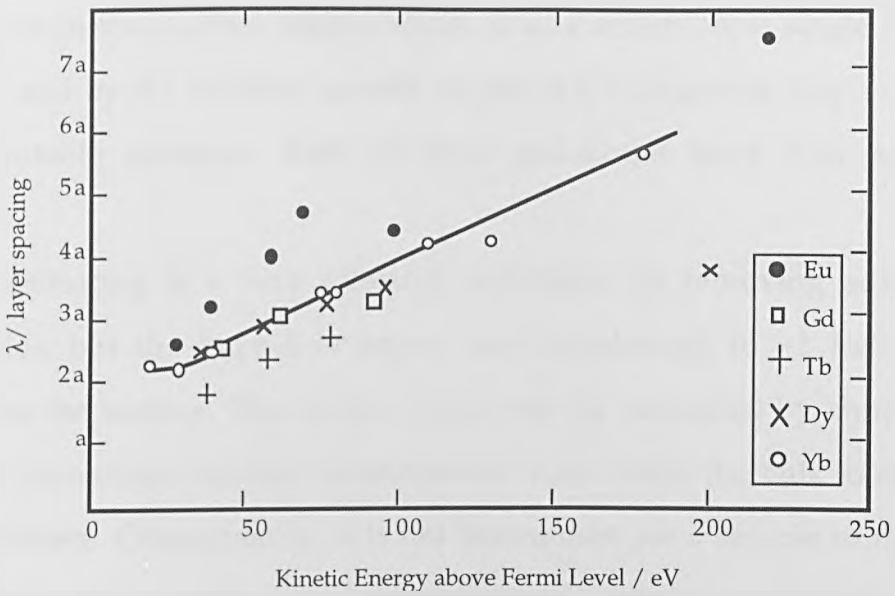

Figure 1.a. The electron's mean free path λ as a function of kinetic energy for various lanthanides. The parameter a signifies the thickness of a single monolayer. Adapted from Gerken *et al* [1.4].

1.4 The Surface Electronic Structure of Yttrium

The first high purity single crystal rare-earth metals became available in the 1980's from laboratories in America (Ames Laboratory, Iowa State University) and from England (The Centre for Materials Science, University of Birmingham). The purity of these samples can be gauged by their residual resistance ratio (RRR), a measure of the resistance of a material at the two convenient temperatures of 300 K and 4.2 K. For unpurified yttrium, a typical RRR value is ~10, whereas high purity yttrium samples have recorded a RRR value in excess of 1000 [1.5]. This may be contrasted with a value of ~520 for scandium obtained through the same purification process (solid state electrotransport). Single crystal samples of lanthanum are difficult to prepare, therefore RRR values are typically lower, and achieve at best ~250 .

In order to probe the surface electronic structure of rare-earth metals, we need an atomically clean surface in UHV. This may currently be achieved in two different ways; by argon ion bombardment (sputtering)

to remove in-situ surface contaminants from a macroscopic single crystal sample, and by the epitaxial growth in-situ of a microscopic single crystal on a suitable substrate. Both of these techniques have their relative merits.

Sputtering is a very effective technique for removing adsorbed molecules, but the impact of argon ions (accelerated to ~2 KeV) also disorders the surface. The surface order may be recovered by annealing, but this encourages residual contaminants from within the bulk to diffuse to the surface. Consequently, it is not uncommon for a sample to receive at least 40 hours worth of 'sputter and anneal' cleaning cycles before the surface is deemed to be both clean and ordered.

By contrast, a deposition rate as slow as one monolayer every 20 minutes can produce reproducible ultrathin films, that show little contamination and form a well ordered (0001) surface after careful annealing. However, these films are formed in the presence of a substrate and this will necessarily introduce a lattice strain into the thin film that may not be relieved until the film's thickness approaches ~100 Å [1.6].

The most suitable substrates for rare-earth thin film growth are the refractory metals, with the (110) surface of tungsten having properties which make it particularly useful; tungsten, with electronic configuration $[Xe]5d^4 6s^2$ is typical of the refractory metals and has a high surface energy. Tungsten possesses the greatest melting point and lowest vapour pressure of all metals, its surface is therefore rigid in comparison to a deposited rare-earth thin film and no alloying occurs at the rare-earth/tungsten interface [1.7]. Tungsten has a body-centred cubic (BCC) crystal structure, and since the (110) plane has a packing density similar to the (0001) plane of HCP metals, tungsten (110) gives rise to (0001) rare-earth crystals.

Although we would not expect the two different methods of

surface preparation to produce identical photoemission spectra, we do expect representative surfaces to exhibit recognisable similarities. Unfortunately, as figure 1.b shows below, this is not the case.

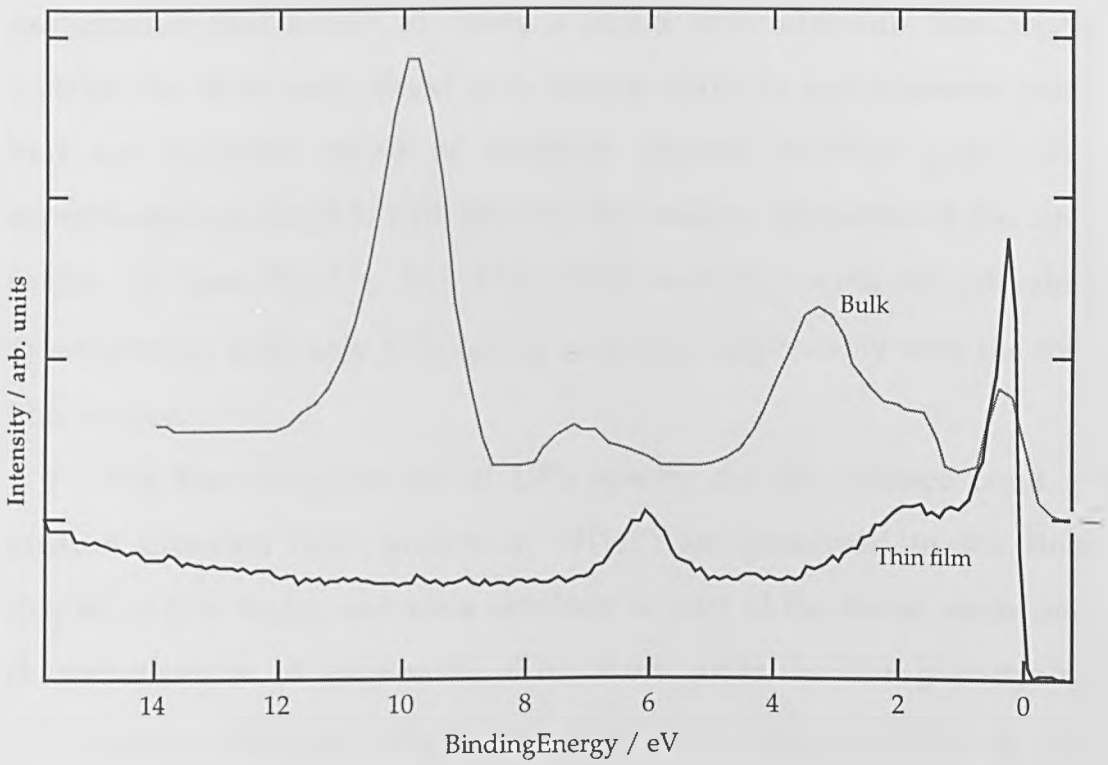

Figure 1.b. Illustrating the differences in the UV photoemission spectra from a bulk Y (0001) sample, and ~ 5 monolayers of Y grown on W(110). The spectra were taken at normal incidence, with photon energies of 40 eV and 33 eV respectively.

The most dramatic difference in the two spectra is the intense feature from the bulk crystal which has a binding energy of ~ 9.6 eV, a feature which is absent from the thin film crystal. This has been named the surface order dependent state (SODS) and has been seen on all bulk rare-earth (0001) surfaces studied to date [1.5]. It is because the SODS is seen only on the (0001) surface of the bulk crystals that it is called surface order dependent. However, its origin remains a mystery since the calculated electronic structure of the rare-earths performed so far show no electron states existing at this binding energy.

It has been suggested [1.8] that the SODS derives from adsorbate contamination, since the binding energy of 9.6 eV is roughly comparable to the binding energy of a simple molecular orbital. To investigate this possibility, the Rare Earth Group at Liverpool began a series of experiments that aimed to create a SODS with ultrathin film single crystals; the films were dosed with various diatomic and triatomic gases that are typically found as residual vacuum chamber gases. The experimental results [1.9, 1.10] showed the catalytic properties of the rare-earths, in that H_2, O_2, CO, CO_2, H_2O and H_2S were all adsorbed dissociatively, with only CH_4 failing to interact appreciably with the thin film surface.

The first complete set of UPS spectra for the valence band of yttrium ultrathin films grown on W(110) are presented in the final chapter of this thesis, and were obtained as part of the initial study and characterisation of rare-earth thin films prior to the gas dosing experiments. Although a definitive explanation for the SODS is still lacking, the differences between the spectra for yttrium ultrathin film crystals and those from a previous studies of a yttrium bulk crystal [1.10] suggested that further investigation was needed.

This thesis also presents the first calculations for yttrium in the presence of a tungsten surface, and the first real-space photocurrent calculation for yttrium, in an attempt to elucidate the differences between the electronic structures of bulk and thin film crystals.

Following on from this introductory chapter, the discussion centres on a review of electronic structure and begins with an account of the single-electron approximation and band structure theory. Next, a thorough review of multiple scattering theory is presented, which aims to present enough of this theoretical framework to justify the real-space

photocurrent equation. There follows a review chapter on photoemission spectroscopy, which concludes with a discussion on the real-space photocurrent equation. The final chapter presents experimental data for the W(110) surface and yttrium ultrathin films grown on W(110), and presents an analysis based on a series of model single-electron calculations.

1.5 References

[1.1] D. D. Koelling, "The Band Model for d- and f- Metals" in The Electronic Structure of Complex Systems, NATO ASI Series B: Physics Vol. 113, 183-242, Plenum (1984).

[1.2] L. V. Moruzzi, J. F. Janak, A. R. Williams, " Calculated Electronic Properties of Metals", Pergammon Press, (1978).

[1.3] J. Braun, "The theory of angle-resolved ultraviolet photoemission", Reports on Progress in Physics, Vol.59, No.10, pp.1267-1338, (1996).

[1.4] F. Gerken, J. Barth, R. Kammerer, L. I. Johansson, A. Flodstrom, "Surface shifts on rare-earth metals", Surface Science, Volume 117, 468-474, (1982).

[1.5] S. D. Barrett, "Angle-resolved photoemission and LEED from rare-earth metals", Surface Science Reports, Volume 14, 7/8, (1992).

[1.6] S. F. Weller, W. Alvarado, K. Schroder and M. Campagna, Phys. Rev. Lett., Volume 54, 1555, (1985).

[1.7] N. P. Tucker, R. I. R. Blyth, R. G. White, M. H. Lee, C. Searle and S. D. Barrett, "Core-level spectroscopy study of rare-earth metal/W(110) interface formation", J.Phys: Condens. Matter, Vol. 10, 6677-6686, (1998).

[1.8] R. Baptist, A. Pellisier and G. Chauvet, Z. Phys. B (Condens. Matter), Vol. 73, 107, (1988).

[1.9] C. Searle, R. I. R. Blyth, R. G. White, N. P. Tucker, M. H. Lee and S. D. Barrett, "Photoemission Study of CO Adsorption on Gd", J. Synchrotron Rad., Vol 2., 312-314, (1995).

[1.10] R. G. White, "Photoemission studies from epitaxial Gd and Y thin films", Ph.D. thesis, University of Liverpool, (1996).

Chapter 2

The Electronic Structure Problem

The purpose of this chapter is twofold: to examine the approximations that must be made when reducing a many electron problem to an equivalent single electron problem, and to discuss the application of the resulting single electron theory to periodic systems. The chapter begins by presenting the Hamiltonian for the electronic structure problem, and discusses quasiparticles before an account of Hartree-Fock theory. This is followed by a review of Hohenberg-Kohn-Sham density functional theory. A brief summary of band theory follows, and the chapter concludes with a short discussion on the motivation for real-space methods in electronic structure calculations.

2.1 Single Particle States and the Many Body Problem

With the discovery of the electron in 1897 by J.J. Thomson [2.1] the classical concept of the atom as an indivisible particle was shattered. The atom now had an inner structure, the exact nature of which was an open question since the electron was known to be charged and Coulombic repulsion would prevent a localisation of the atomic electrons. By placing the atomic electrons within a vague globule of positive charge

(Thomson's short-lived 'plum-pudding' model of the atom) he can be credited with qualitatively solving the first electronic structure problem.

One hundred years later, the study of electronic structure has matured within the domain of quantum mechanics and acquired a logical rigour through density functional theory, but the essential problem of electronic structure remains; to describe the energy states of a given configuration of electrons subject to a suitably defined external potential.

The most general Hamiltonian H for the electronic structure problem is written as $H = T + U + V$, where T is the kinetic energy operator, V is the potential energy operator and U is an operator denoting any other interactions. For crystalline systems we can fix the nuclei onto the lattice sites R_n by invoking the Born-Oppenheimer approximation, and thus write the many-body Schrödinger equation for M nuclei with atomic number Z_n and N electrons of mass m as

$$\left[-\frac{\hbar^2}{2m} \sum_{i}^{N} \nabla_i^2 - \sum_{n}^{M} \sum_{i}^{N} \frac{e^2 Z_n}{\left| \vec{R}_n - \vec{r}_i \right|} + \frac{1}{2} \sum_{i \neq j}^{N} \frac{e^2}{\left| \vec{r}_i - \vec{r}_j \right|} \right] \Psi = E \Psi, \qquad (2.1)$$

where r_i relates the positions of the electrons, e is the fundamental unit of charge, $h = 2\pi\hbar$ is Planck's constant, E is the energy eigenvalue and $\Psi = \Psi(\vec{r}_1, \vec{r}_2, \ldots, \vec{r}_N)$ is a many-body eigenfunction.

This is without doubt a complicated problem, since the mutual interactions of the electrons introduces non-local energy terms which cannot be calculated in a precise way. The difficulty has initiated two broad philosophies for its solution: empirical methods such as the psuedopotential method rely on the specifics of experimental data to parameterise their calculations, whereas *ab initio* methods contain no adjustable parameters, using instead fundamental physical quantities (primarily the atomic number Z) in their calculative schemes.

Much of the technical detail concerning the *ab initio* solution of electronic structure problems can be understood as an attempt to find pragmatic approximations to the troublesome electron-electron interactions, approximations which are ultimately validated by their agreement with experiment and which reduce the many-body equation to a more tractable form.

However, before examining some of these approximations, we need to consider one important model for inter-electron interactions which does allow single particle states to emerge from the many electron gas, this being the formation of quasiparticles.

2.1.2 Quasiparticles

The quasiparticle concept [2.2, 2.3] may be understood intuitively via a model of an electron-gas in its ground-state, which is later perturbed by the addition of an extra electron. The gas responds to this excitation in a way that screens the long-ranged Coulomb force of the additional electron, thereby localising its influence. The electron plus the response of the gas constitute a quasiparticle, which can only interact weakly with other quasiparticles. By forming quasiparticles, the many-electron system effectively reduces to an independent quasiparticle system.

Clearly, the "electron plus response" quasi-particle is only a valid concept over a limited range of energies near the Fermi level, since the extra electron is forbidden from interacting with occupied states at lower levels by the Pauli exclusion principle [2.4], but the concept of quasiparticle formation does supply a useful explanation for the appearance of single-particle features in electron spectroscopy data, if only in a limited sense.

We can now examine two different approaches to the many-electron problem which achieve a single-particle description; the wave

function methods of Hartree-Fock theory and density functional theory.

2.2 The Hartree and Hartree-Fock Equations

Hartree conjectured [2.5, 2.21(a)] that a single-electron experiences the many-electron ensemble as a mean or "effective" potential field U_h acting locally. The conjecture is realised by assuming that the many-electron wave function Ψ can be represented by a product of single-electron states Φ, the Hartree orbitals:

$$\Psi(\vec{r}_1,\vec{r}_2,\ldots,\vec{r}_3) = \prod_i^N \Phi(\vec{r}_i), \tag{2.2}$$

which allows a charge density to be assigned, for instance, to the kth orbital $\Phi(\vec{r}_k)$ as the product of its position probability density with charge $-e$. This gives a total charge density for the remaining electrons in the system as

$$\mathrm{n}(\vec{r}) = -e\sum_{j\neq k}^{N}\left|\Phi(\vec{r}_j)\right|^2, \tag{2.3}$$

and solving Poisson's equation for the potential arising from the density $\mathrm{n}(\vec{r})$ gives a mean field U_h for $\Phi(\vec{r}_k)$,

$$U_h = \sum_{j\neq k}^{N}\int d^3\vec{r}_j \left|\Phi_j(\vec{r}_j)\right|^2 \frac{e^2}{\left|\vec{r}_j-\vec{r}_k\right|}. \tag{2.4}$$

Hartree's equation for the kth orbital has now taken a single-electron form for the many-electron problem;

$$H_k\Phi(\vec{r}_k) = \varepsilon_k\Phi(\vec{r}_k), \tag{2.5}$$

where ε_k is a single-electron energy eigenvalue and the Hamiltonian H_k

is now written as

$$H_k = -\frac{\hbar^2}{2m}\nabla_k^2 - \underbrace{\sum_n^M \frac{e^2 Z_n}{\left|\vec{R}_n - \vec{r}_k\right|}}_{\hat{V}} + \underbrace{\sum_{j\neq k}^N \int d^3 r_j \left|\Phi_j(\vec{r}_j)\right|^2 \frac{e^2}{\left|\vec{r}_j - \vec{r}_k\right|}}_{\hat{U}_h}. \qquad (2.6)$$

Hence, with an $N-$electron system Hartree's method produces N single-electron, simultaneous, nonlinear integrodifferential equations which cannot be solved analytically, but they do permit an approximate solution through self-consistency (see figure 2.a, below).

In the self-consistent solution an effective potential, or its equivalent charge density, is assumed for the potential terms $(V+U_h)$. The Hartree equations (2.5) are solved to produce a new system of eigenfunctions; these are subsequently used to provide a better estimate for the potential. The cycle is halted when the eigenfunctions are 'consistent' with the potential to a suitably high degree of accuracy; whence the two estimated functions are mutually agreeable and Hartree's equation produces essentially a single energy eigenvalue.

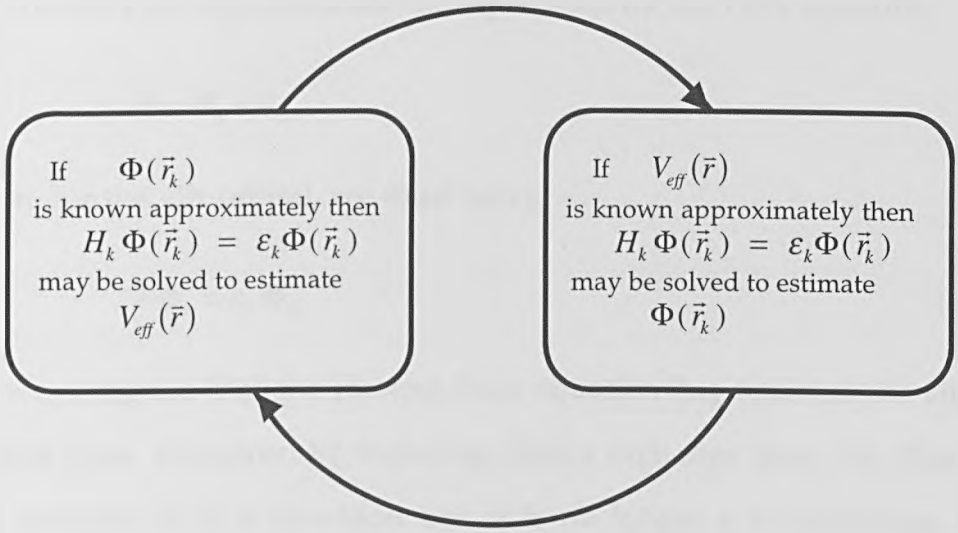

Figure 2.a, the self-consistency cycle.

Unfortunately Hartree's solution of the electronic structure problem suffers from a serious drawback. A simple product of wave functions (2.2) is unphysical because it does not make any allowance for antisymmetry properties. Consequently, Hartree's electrons do not obey the Pauli exclusion principle, and must be regarded as semi-classical.

The oversight was amended by Fock, who considered the many-electron wave function to be a Slater determinant of single-electron wave functions,

$$\Psi(\vec{r}_1,\vec{r}_2,\ \ldots\ ,\vec{r}_N) = \frac{1}{\sqrt{N!}}\begin{vmatrix} \Phi_1(\vec{r}_1) & \Phi_1(\vec{r}_2) & \ldots & \Phi_1(\vec{r}_N) \\ \Phi_2(\vec{r}_1) & \Phi_2(\vec{r}_2) & \ldots & \Phi_2(\vec{r}_N) \\ \vdots & \vdots & \ldots & \vdots \\ \Phi_N(\vec{r}_1) & \Phi_N(\vec{r}_2) & \ldots & \Phi_N(\vec{r}_N) \end{vmatrix}. \qquad (2.7)$$

Fock's analysis of the problem identified an additional exchange term V_{ex} that was subsequently incorporated into Hartree's equations;

$$V_{ex} = -e^2 \sum_j \int d\vec{r}\,' \frac{1}{|\vec{r}-\vec{r}\,'|} \Phi_j^*(\vec{r}\,')\Phi_i(\vec{r}\,')\Phi_j(\vec{r})\delta_{ij}. \qquad (2.8)$$

The Hartree-Fock equations are thus governed by the Fock operator,

$$F = H_h + V_{ex}, \qquad (2.9)$$

so that, for the kth orbital, we must solve

$$F\Phi_k = \varepsilon_k \Phi_k, \qquad (2.10)$$

and we recognise that the Hartree-Fock equation has retained the single-electron form. However, by including Fock's exchange term, the Hartree-Fock operator (2.9) is non-local and it is no longer a Hamiltonian. This makes the solution of the Hartree-Fock equations technically very

challenging, and in practice the exchange terms may be replaced by a suitably constructed potential [2.6].

2.3 Density Functional Theory

Despite the ingenuity of early attempts to solve the electronic structure problem, it was not until the 1960's that a unique solution was first shown to exist in principle through the ground breaking analysis of density functional theory (DFT).

The historical roots of DFT can be traced to the birth of quantum mechanics with the statistical Thomas-Fermi theory of the atom [2.5, 2.7, 2.21(b)], which first recognised that a functional relationship exists between the density of electrons $n(\vec{r})$ and the many-body wave function of the ground-state energy. The renaissance of this idea - that it is the single-electron density which is the fundamental parameter for the description of many-electron systems - arose from the work of Hohenberg and Kohn [2.8] who founded their modern DFT on two vital theorems that initially required the ground-state to be non-degenerate, a requirement which has since been lifted [2.9, 2.10].

Hohenberg-Kohn-Sham DFT

Hohenberg and Kohn's first theorem proves that the ground-state energy is a unique functional of the ground-state electron density $E_o[n(\vec{r})]$, by showing that there is a unique ground-state density for any applied potential field. The logical structure of DFT is completed by their second theorem that proves the existence of a minimum for $E_o[n(\vec{r})]$ at the ground-state density; this is identified as the true ground-state energy of the many-electron system. Although Hohenberg and Kohn provided an exact expression for the energy functional, their equation is just as

intractable as solving the full many-electron problem.

In practice, the total energy functional $E_o[n(\vec{r})]$ is constructed within DFT by approximating the dominant contributive energy terms as functionals of the electron density:

$$E_o[n(\vec{r})] = T_o[n(\vec{r})] + E_{ext}[n(\vec{r})] + E_h[n(\vec{r})] + E_{xc}[n(\vec{r})], \qquad (2.11)$$

where the kinetic energy functional $T_o[n(\vec{r})]$ is calculated from the ground state of a non-interacting gas at density $n(\vec{r})$, $E_{ext}[n(\vec{r})]$ denotes the external potential functional arising from electron-nuclei interactions, $E_h[n(\vec{r})]$ is the Hartree functional for the electron interactions and the last term, $E_{xc}[n(\vec{r})]$, is the exchange-correlation functional that accounts for all other possible interactions. Writing these terms explicitly gives the Hohenberg-Kohn functional,

$$E_o[n(\vec{r})] = T_o[n(\vec{r})] - \sum_{M=1}^{N} Ze \int d\vec{r}\, \frac{n(\vec{r})}{|\vec{r} - \vec{R}_M|} + \frac{1}{2}\int d\vec{r}\, d\vec{r}\,' \frac{n(\vec{r})\, n(\vec{r}\,')}{|\vec{r} - \vec{r}\,'|} + E_{xc}[n(\vec{r})]. \qquad (2.12)$$

The ground-state density that minimises (2.12) was obtained by Hohenberg and Kohn using a variational principle constrained by a conservation rule on the number of electrons, and was shown to reduce to an equivalent problem that demonstrates a deep connection between many-electron and single-electron states: minimising the density in the Hohenberg-Kohn functional is equivalent to finding the motion of a single-electron in an effective potential field.

The Kohn-Sham Equations and the LDA

Kohn and Sham [2.11] next extended DFT by assuming the ground-state density to be composed of determinental orbitals, and showed that the minimisation is equivalent to self-consistently solving a set of single-electron equations having the form of Schrödinger's equation (the Kohn-Sham equations);

$$\left(-\frac{\hbar^2}{2m}\nabla^2 + v_{eff}(\vec{r})\right)\Phi_i(\vec{r}) = \varepsilon_i\,\Phi_i(\vec{r}), \qquad (2.13)$$

where ε_i is a single-electron local density eigenvalue and the effective potential $v_{eff}(\vec{r})$ is

$$v_{eff}(\vec{r}) = -\sum_{M=1}^{N}\frac{Ze^2}{|r-R_M|} + \int d\vec{r}'\frac{n(\vec{r}')}{|\vec{r}-\vec{r}'|} + v_{xc}(\vec{r}). \qquad (2.14)$$

The last term in (2.14), $v_{xc}(\vec{r})$, is the exchange-correlation potential which, once again, is an unknown quantity that signifies the electron-electron interactions.

Kohn and Sham next introduced the simplifying approximation that elevated DFT into a workable computational method. Although the density dependent exchange-correlation energy functional $E_{xc}[n(\vec{r})]$ cannot be calculated precisely, a quantity which can be calculated is the exchange-correlation energy function for the homogeneous electron gas.

Kohn and Sham thus replaced the unknown functional E_{xc} having variable spatial density, with a wholly tractable function having an equivalent density for every corresponding point in space. This is the local density approximation (LDA), which has proved to be surprisingly successful in reproducing by calculation the data from electron spectroscopy, since there is no formal justification for identifying the local

density eigenvalues with the quasiparticle states of spectroscopy, other than noting that self-energy corrections to the LDA are small for most metallic systems [2.10].

The Hohenberg-Kohn-Sham DFT has recently been given a final rigorous mathematical foundation in terms of convex functional analysis with the work of Leib and Levy [2.9] and both Thomas-Fermi theory and Hartree-Fock theory have been subsumed into this more general work.

Having examined the relationship between many-electron and single-electron states, we can now consider the role of a periodic potential on single-electron states with some degree of confidence that this approach is suitable for a study of the electronic structure of crystalline systems.

2.4 Single Electron States and Band Theory

Concurrent with the development of methods to study many-electron systems, the foundation of quantum mechanics also generated the first investigations into the properties of Schrödinger's equation with a spatially periodic potential, and the existence of quasi-continuous bands of stationary states was duly reported by Strutt, and independently by Bloch [2.15].

The periodic Schrödinger equation is an example of a Hill's equation [2.23], a linear differential equation having the coefficient of the dependent variable as a periodic function of the coordinate. Mathieu provided solutions for this type of equation in 1868 that today correspond to band edges, and Floquet found more general solutions in 1883 that would now be recognised as one dimensional Bloch functions.

The key ingredients of band theory are conceptually simple; a single electron moves within a potential field which has the same discrete

symmetry properties as a crystal lattice. The symmetry is expressed through the translation operator T_R as

$$T_R \Psi(r) = \Psi(r + R), \tag{2. 15}$$

where R is a vector in the space spanned by the crystal lattice vectors. Employing the cyclic Born-von Karmen boundary conditions leads to Bloch's theorem:

$$\Psi(r+R) = e^{i\vec{k}\cdot\vec{R}} \Psi(r), \tag{2. 16}$$

where $\vec{k}$, the propagation vector for the electron, labels the energy eigenvalue. This labelling is permitted because the translation operator T_R is compatible with the Hamiltonian of the periodic Schrödinger equation, and so ε and k are simultaneous eigenstates. Consequently, the solution of Schrödinger's equation can take the form

$$H\Psi_k = \varepsilon(k)\Psi_k, \tag{2. 17}$$

whenever the Hamiltonian H contains a periodic potential.

Electron states satisfying Bloch's theorem are then Bloch functions; delocalised and existing everywhere within the lattice. Band states arise because the function $\varepsilon(k)$ is both many-valued and analytic, with each analytic branch defining a band. The band structure, which is the dispersion relation for $\varepsilon(k)$, is traditionally solved by numerical schemes that either employ partial wave summation or expansion by a fixed basis set to describe the electronic states [2.22].

A great advance for these schemes came in the 1980's with the linear methods championed by Andersen [2.16, 2.22], that use energy-independent fixed basis functions derived from the partial waves. Arguably, the most popular of these is the linear muffin-tin orbital

method within the atomic sphere approximation (LMTO - ASA), which uses a fixed basis set of angular momentum eigenfunctions (the muffin-tin orbitals) to describe the electron states, an approach which works well with close-packed metal systems. In recent years, Andersen's LMTO programme has also incorporated the recursion method, in what is now called the 'tight-binding' LMTO [2.14]. Since this was the computational method used to generate the band structures and density of states in chapter five, a brief overview follows.

2.4.1 The Tight-Binding LMTO Method

At the heart of the tight-binding LMTO is the recursion method initially proposed by Haydock [2.13]. Haydock recursion is a rapidly converging real-space technique that calculates orthogonal basis states via a continued fraction algorithm. This has been included in the LMTO formalism through a transformation of the muffin-tin orbitals into an equivalent set of screened orbitals; these having a much shorter spatial range, so that only shells of nearest neighbour atoms need be considered in the calculation. The result is a more compact order N computational problem, and the tight-binding LMTO is a very fast technique in comparison to its predecessor.

Andersen and his co-workers have released the tight-binding LMTO program LMASA-46 for use in educational establishments. This code is a remarkably user-friendly suite of programs that can be used to calculate a variety of properties of interest in the study of crystalline materials (see figure 2.b, overleaf). The program input requires only the atomic species, their lattice coordinates within the unit cell, and the crystal's space group number to be supplied by the user. The filling of atomic shells using Hund's rules and all symmetry checking operations

are incorporated into the program. The self-consistent calculation produces a potential file for each atomic species, which is then available for any further calculations that may be necessary.

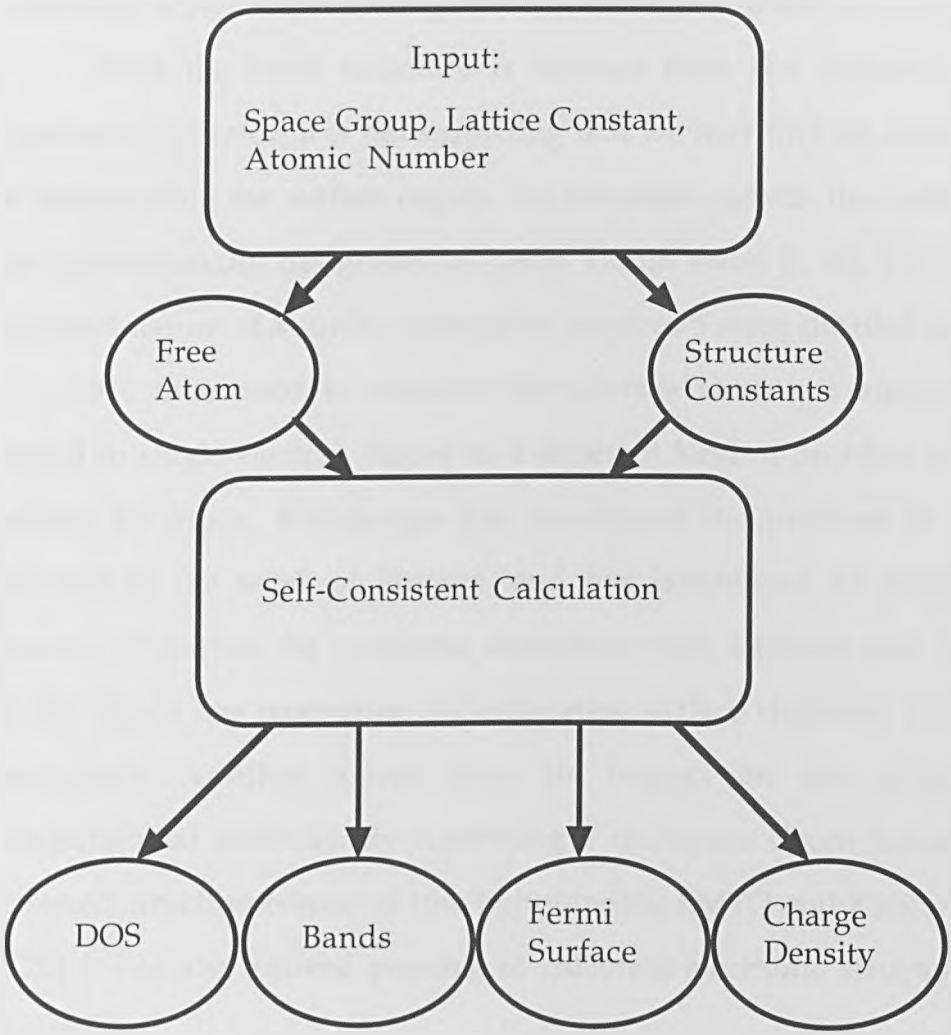

Figure 2.b, showing a schematic of the LMASA-46 program.

2.5 Surface Electronic Structure

At the surface of a crystal we can expect to experience difficulties when using Bloch's theorem; the calculations must assume a symmetry

at the surface which simply may not exist. The metal surface responds to the breaking of the full three dimensional crystal symmetry usually by inter-layer relaxations and contractions, but it can also reconstruct into a completely different symmetry group. A dramatic example of this behaviour is provided by the giant reconstructions of the rare-earths [2.17].

Since the band structure is derived from the properties of the translation operator, it is not surprising that we may find an additional set of states within the surface region. For transition metals, the surface states are conventionally designated as being Tamm states [2.18], but in reality the exact nature of a surface state often requires a more detailed analysis.

We thus need to consider the surface electronic structure with regard to single-electron theory as a different kind of problem to the one tackled by Bloch. Weinberger has considered the problem to be more relevant to the work of Floquet, and has introduced an entirely new lexicon to discuss the problems associated with surfaces and interfaces [2.19]. This is one motivation for calculating surface electronic structure in real-space. Another arises from its impact on the efficiency of computational methods. By combining a real-space Green function with screened structure constants (the tight-binding LMTO and KKR methods), [2.20] it has also proved possible to calculate electronic structures more rapidly.

Having reviewed single electron theory and its approach to the electronic structure problem, we shall examine multiple scattering theory in the next chapter and show how this technique can be applied to calculate the density of states.

2.6 References

[2.1] J. J. Thomson, Philosophical Magazine, Vol. 48, 567, (1899).

[2.2] W. Jones and N. H. March, "Theoretical Solid State Physics. Vol.1: Perfect Lattices in Equilibrium", Dover Publications, Chapter One, (1985).

[2.3] R. D. Mattuck, "A Guide to Feynman Diagrams in the Many-Body Problem", McGraw-Hill, (1967).

[2.4] C. Kittel, "Introduction to Solid State Physics", (Sixth edition), 253-288, John Wiley and Sons, (1986).

[2.5] L. I. Schiff (and references therein) "Quantum Mechanics", (Third edition), McGraw-Hill, 424-466, (1968).

[2.6] L. Hedin and S. Lundquist (and references therein) "Effects of Electron-Electron and Electron-Phonon Interactions on the One-Electron States of Solids", Solid State Physics, Vol.23, 1-181, (1969).

[2.7] N. W. Ashcroft and N. D. Mermin, "Solid State Physics", W.B. Saunders Company, 329-352, (1976).

[2.8] P. Hohenberg and W. Kohn, Phys.Rev., Vol.138, B864, (1964).

[2.9] H. Eschrig, "The Fundamentals of Density Functional Theory", Lecture Notes, (private communication).

[2.10] F. Aryasetaiwan and O. Gunnarsson, "The GW method", Rep Prog. Phys., Vol. 61, 237-312, (1998).
S. G. Louie, "Quasiparticle Excitations and Photoemission" in "Angle Resolved Photoemission: theory and current applications", (ed.) S. D. Kevan, Studies in Surface Science and Catalysis, Vol. 74, Elsevier Science Ltd., (1992).

[2.11] W. Kohn and L. J. Sham, Phys. Rev. A, Vol. 140, 1133, (1965).

[2.13] R. Haydock, V. Heine, M. J. Kelly, J.Phys.C. Vol.8, 2591 (1975).
V.Heine,D.W.Bullett, R.Haydock and M.J.Kelly, Solid State Physics, Vol. 35, Academic Press, New York, (1980).

[2.14] H. J. Nowak, O. K. Andersen, T. Fujiwara, O. Jepsen, P. Vargas, Phy. Rev. B, Vol. 44, 8, 3577-3598, (1991).

[2.15] H. Jones, "The Theory of Brillouin Zones and Electronic States in Crystals", North Holland Publishing Company, (1962).

[2.16] O. K. Andersen, "Linear Methods in Band Theory", The Electronic

Structure of Complex Systems, NATO ASI Series B: Physics Vol. 113, 11-66, Plenum (1984).

[2.17] S. D. Barrett, R. I. R. Blyth, A. M. Begley, S. S. Dhesi and R. G. Jordan, Phys. Rev. B. , Vol. 43, 6, 4573-4578, (1991).

S. S. Dhesi, "Surface structure of rare-earth metals", Ph.D Thesis, University of Liverpool, (1993).

[2.18] J. E. Inglesfield, "Surface Electronic-Structure", Rep. Prog. Phys., No. 3, 223-284, (1982).

[2.19] P. Weinberger, "Multilayer systems and symmetry", Phil. Mag. B , Vol. 75, No.4, 509-533, (1997).

[2.20] P. Weinberger, I. Turek and I. Szunyogh, "The TB-LMTO method and its relation to the screened KKR method", International Journal of Quantum Chemistry, Vol. 63, No. 1, 165-188, (1997).

R. Zeller, P. H. Dederichs, B.Ufalussy, L. Szunyogh and P.Weinberger, Phys. Rev. B, Vol. 52, 12, 8807-8812, (1995).

[2.21(a)] A.Messiah "Quantum Mechanics", Vol. 2, North Holland Publishing Company, 773-781, (1962).
[2.21(b)] A. Messiah *ibid* ., 615-619.

[2.22] H.L. Skriver, "The LMTO-Method", Springer-Verlag, (1983).

[2.23] M.S.P. Eastham, "The Spectral Theory of Periodic Differential Equations", Scottish Academic Press Ltd., (1973).

Chapter 3

Scattering Theory and the Multiple Scattering Green Function

The purpose of this chapter is to establish the boundary conditions for scattering events, and to show how these lead to the multiple scattering Green function, since it is this Green function which underpins the photocurrent equation discussed in the next chapter. Rydberg units are used throughout this chapter, in which $\hbar^2 = 2m = e = 1$.

We begin with an account of the radial wave equation and phase shift analysis before discussing briefly the solution of inhomogeneous differential equations by Green functions. The Green function is then related to the density of states. Next, we present an analysis of potential scattering, which introduces the Lippmann-Schwinger equations, before discussing Gyorffy's scattering path operator and the multiple scattering Green function.

3.1 A Framework for Scattering Theory

The quantum mechanical theory of scattering is founded on the principle that it is the asymptotic scattering state which is an observable [3.1]; it is not necessary to know the exact microphysical interactions that occur during the brief interval of the scattering event and consequently

scattering can be modelled as a 'black box' process, in which an initial 'input' state is converted into an 'output' scattered state.

Although a more general treatment of scattering theory allows for energy exchanges we need only consider elastic scattering, since it is this so-called 'on the energy shell' condition (conservation of kinetic energy) which allows the scattered state to be derived from the phase shifts [3.2]. This will be discussed in more detail below.

The multiple scattering theory reviewed here is a single-electron theory that neatly divides the electronic structure problem into two parts; local (atomic) scattering properties are calculated and then used with the global (structural) properties of a distributed assembly of those scatterers to calculate observables. In applying this technique to problems of electronic structure, we assume that the potentials which act as scattering centres have been generated self-consistently using methods akin to those discussed in the previous chapter. The potential thus contains all the many-electron interactions, and the single-electron only interacts with the potential.

3.2 The Radial Wave Equation and Phase Shifts

In what follows we shall be investigating the effects of scattering from a spatially finite spherical potential; the so-called muffin-tin potential which has the form [3.3, 3.4]

$$V(\vec{r}) = \begin{cases} V(\vec{r}) - C & for\ r \le S \\ C & for\ r \ge S \end{cases} \tag{3.1}$$

where S is the radius of the muffin-tin sphere and C is a constant that denotes the interstitial region between the muffin-tin spheres. It is convenient to assume that $C = 0$ in what follows, without loss of generality (see figure 3.a, overleaf).

If we incorporate a muffin-tin potential $V(\vec{r})$ into the Hamiltonian for the time independent Schrödinger equation, we obtain the familiar energy eigenvalue problem:

$$\left[\nabla^2 + V(\vec{r})\right]|\Psi\rangle = \varepsilon\,|\Psi\rangle, \tag{3.2}$$

where ∇^2 is the kinetic energy operator and ε is the single-electron energy eigenvalue. For non-core states we can set $k = \sqrt{\varepsilon}$, and the solution

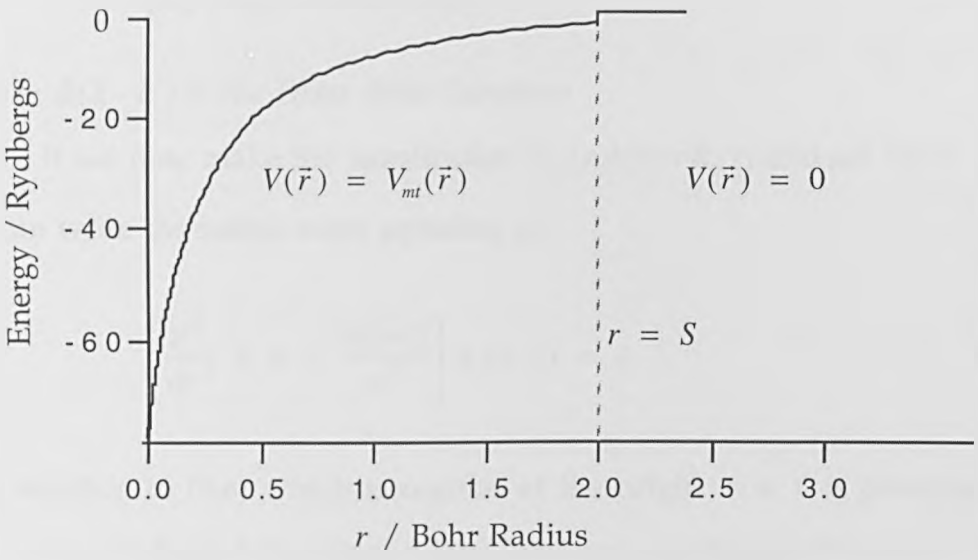

Figure 3.a: showing the different regions in the muffin-tin potential. The potential shown has been adapted from an LMASA-46 potential for tungsten.

to (3. 2) can be written as:

$$\Psi_k(r) = \sum_L a_L(k) R_l(r) Y_L(\hat{r}), \tag{3.3}$$

where $Y_L(\hat{r})$ is a spherical harmonic with $\hat{r}$ a unit vector and $L = l,m$ denotes the angular and spin momentum indices respectively, $a_L(k)$ is the expansion coefficient and $R_l(r)$ is the radial wave function that satisfies the radial wave equation,

$$\left[\frac{1}{r^2}\frac{d}{dr}(r^2\frac{d}{dr}) + \varepsilon - V(\vec{r}) - \frac{l(l+1)}{r^2}\right] R_l(r) = 0. \tag{3.4}$$

For a unique solution to the eigenvalue problem (3.2) we require $\Psi_k(\vec{r})$ to be regular as $r\to\infty$ and normalisable. The difficulties of normalisation in the continuous spectrum of the eigenvalue problem are well known [3.16] and we shall assume that $\Psi_k(\vec{r})$ is normalised such that

$$\langle \Psi_{k'} | \Psi_k \rangle = \delta(k-k'), \tag{3.5}$$

where $\delta(k-k')$ is the Dirac delta function.

If we now make the substitution $u_l(r,k)=rR_l(r)$ and set $V(\vec{r}) = 0$, we can write the radial wave equation as

$$\left[\frac{d^2}{dr^2} + \varepsilon - \frac{l(l+1)}{r^2}\right] u_l(r,k) = 0. \tag{3.6}$$

The solution to (3.6) which is regular at the origin $r = 0$ is provided by the spherical Bessel function $j_l(kr)$, and we emphasise that this is the free-space solution in what follows. The spherical Bessel function has the asymptotic form [3.5]

$$j_l(kr) \underset{r\longrightarrow\infty}{\approx} \frac{1}{kr}\sin\left[kr - \frac{l\pi}{2}\right], \tag{3.7}$$

Another solution to equation (3.6) which is, however, irregular at the origin is the spherical Neumann function, $n_l(kr)$, with asymptotic form [3.5]

$$n_l(kr) \underset{r\longrightarrow\infty}{\approx} -\frac{1}{kr}\cos\left[kr - \frac{l\pi}{2}\right], \tag{3.8}$$

We are now in a position to discuss the conceptual basis of phase shift analysis.

3.2.1 The Meaning of the Phase Shift

We can write the general free-space solution to equation (3.4) as

$$R_l(r,k) = B_l(k) j_l(kr) + C_l(k) n_l(kr), \tag{3.9}$$

where $B_l(k), C_l(k)$ are normalising coefficients. To obviate the irregular behaviour of $n_l(kr)$, we can choose $C_l(k) = 0$ whenever the solution needs to include the origin.

Since the asymptotic forms (3. 7) and (3.8) may be combined into

$$R_l(r,k) \underset{r\longrightarrow\infty}{\approx} \frac{1}{kr}\sin\left[kr - \frac{l\pi}{2} + \delta_l(k)\right], \tag{3.10}$$

the general solution has a phase $\delta_l(k)$, which is additional to the free-space solution. If we identify the free-space solution $j_l(kr)$ with an incident wave and, taking account of the restriction on the spatial domain for $n_l(kr)$, identify the spherical Neumann function with the scattered wave that radiates from the surface of the potential sphere, then we note that the extra phase $\delta_l(k)$ arises from the scattered wave. The coefficients in (3.9) can now be expressed in accordance with equation (3.10) so that a 'null' scattering event, characterised by $\delta_l(k) = 0$, coincides with the free-space solution everywhere. This is the 'phase shift' form of the radial wave function:

$$R_l(r,k) = \cos\delta_l(k) j_l(kr) + \sin\delta_l(k)\ n_l(kr). \tag{3.11}$$

We can also express the linear combination (3.9) in the complex plane

through the spherical Hankel functions [3.6],

$$h_l^{\pm}(kr) = j_l(kr) \pm i n_l(kr), \tag{3.12}$$

where $h_l^{+}(kr)$ is a spherical Hankel function of the first kind and $h_l^{-}(kr)$ is a spherical Hankel function of the second kind. These solutions behave asymptotically like spherical waves,

$$h_l^{\pm}(kr) \underset{r \to \infty}{\sim} \frac{i^{-(l+1)} e^{\pm ikr}}{kr}, \tag{3.13}$$

a property which makes them especially useful in scattering problems.

3.2.2 Calculating the Phase Shift

We can use the phase-shift form of the radial wave function to calculate $\delta_l(k)$ by considering the continuity of $R_l(r,k)$ at the boundary of the muffin-tin sphere. Continuity is established when both the function and its spatial-derivative have equal value across the boundary; that is, we require the logarithmic derivative $\beta_l(k)$ of the radial wave function evaluated at the muffin-tin boundary ($r = S$) to be

$$\beta_l(k) = \frac{1}{R_l(r,k)} \left(\frac{d R_l(r,k)}{dr} \right) \Bigg|_{r=S} \tag{3.14}$$

With this matching condition for the wave function the phase shift can be calculated from the relationship

$$\tan \delta_l(k) = \frac{k n_l'(kS) - \beta_l(k) n_l(kS)}{k j_l'(kS) - \beta_l(k) j_l(kS)}, \tag{3.15}$$

where the primed functions have been differentiated with respect to the argument kr.

3.3 Differential Equations and Green Functions

In the theory of linear differential equations, the inhomogeneous equation has the form

$$L_r|\Psi\rangle = \sigma(r), \tag{3.16}$$

where L_r is a linear differential operator and $\sigma(r)$ is called the source term [3.6]. The corresponding homogeneous equation is a special case of (3.16) when $\sigma(r) = 0$; its solution is known as the complementary function and we will write this as $|\Phi\rangle$. The inhomogeneous differential equation (3.16) is solved by a linear combination of the complementary function and any $|\Psi\rangle$ that satisfies the prescribed boundary conditions for the full problem; this latter solution is the particular integral and we can find it by considering the following operator relationship,

$$L_r^{-1} L_r = 1, \tag{3.17}$$

where L_r^{-1} is the inverse operator to L_r and 1 is the identity operator. Consequently, equation (3.16) may be solved by applying L_r^{-1} on the left and using the result (3.17). We then have the particular integral,

$$|\Psi\rangle = L_r^{-1}\sigma(r). \tag{3.18}$$

The general solution of the inhomogeneous equation (3. 16) is therefore,

$$|\Psi\rangle = |\Phi\rangle + L_r^{-1}\sigma(r). \tag{3.19}$$

Since L_r is a differential operator, the inverse operator is an integral operator and the 'solution' recasts (3.16) into an equivalent integral equation which must satisfy the same boundary conditions. The

integral equation may be solved when L_r^{-1} is known explicitly.

The inverse operator called the Green function $G(r, r')$ uses an extra degree of freedom r' as an additional parameter and we adopt the convention that

$$G(r, r')\ L_r = \delta(r - r'). \tag{3.20}$$

This is the defining equation for the Green function belonging to the differential operator L_r. It may be interpreted as the response of the system to a unit source at r'. The extra degree of freedom also serves another purpose by shifting our attention to any region of interest within the space of the variable r, so it is not surprising that elsewhere in the literature $G(r, r')$ is also called a propagator.

3.3.1 Green Functions and the Density of States

The Green function can be related to an eigenfunction which is complete in Hilbert space via its modal expansion [3.7]. Calling the eigenfunction $|\Psi_n\rangle$, this is written as,

$$G^{\pm}(r, r';\varepsilon) = \lim_{\eta \to 0^+} \sum_n \frac{|\Psi_n\rangle\langle\Psi_n|}{\varepsilon - \varepsilon_n \pm i\eta}, \tag{3.21}$$

where ε_n denotes the eigenvalue, $i\eta$ is a purely imaginary infinitesimal and the summation includes integration for any continuous part of the eigenvalue spectrum. Consequently, the Green function exists only for $\varepsilon \neq \varepsilon_n$, since the eigenvalues ε_n appear as simple poles on the real axis for the discrete part of the spectrum and as a natural boundary in the continuum. The singular behaviour is 'smoothed' by the imaginary infinitesimal $i\eta$, which displaces the poles from the real axis and into the complex plane.

The limiting process which recovers the Green function serves as an additional boundary condition and more than one Green function can be constructed. We shall choose the 'outgoing' Green function G^+ as the most suitable for what follows; we shall see later that G^+ corresponds to a divergent spherical wave, whereas the alternative choice of G^- gives a spherically convergent wave - a difficult state to prepare in nature.

We can now derive an expression for the density of states [3.8]. The trace of a Green function is obtained by analogy with the trace of a matrix. Setting $r = r'$ and integrating over all space, we find

$$\int dr\, G^+(r,r;\varepsilon) = \underset{\eta \to 0^+}{Lim} \int dr \sum_n \frac{|\Psi_n\rangle\langle\Psi_n|}{\varepsilon - \varepsilon_n + i\eta} . \qquad (3.22)$$

We can make use of the formal identity [3.9]

$$\underset{\eta \to 0^+}{Lim} \sum_n \frac{1}{\varepsilon - \varepsilon_n + i\eta} = \mathscr{P}.\mathscr{P}.\left(\frac{1}{\varepsilon - \varepsilon_n}\right) - i\pi\delta(\varepsilon - \varepsilon_n), \qquad (3.23)$$

where $\mathscr{P}.\mathscr{P}.$ denotes the principal part, to establish the relationship

$$\delta(\varepsilon - \varepsilon_n) = -\frac{1}{\pi}\, \mathscr{I}m \left\{ \underset{\eta \to 0^+}{Lim} \frac{1}{\varepsilon - \varepsilon_n + i\eta} \right\}, \qquad (3.24)$$

which gives, on inspecting the trace of the Green function (3. 22),

$$-\frac{1}{\pi}\, \mathscr{I}m \left\{ \int dr\, G^+(r,r;\varepsilon) \right\} = \sum_n \delta(\varepsilon - \varepsilon_n). \qquad (3.25)$$

This last expression is the density of states, because it simply counts the number of eigenvalues within a given interval. Denoting the density of states by $\rho(\varepsilon)$, we can therefore write explicitly

$$\rho(\varepsilon) = -\frac{1}{\pi} \mathcal{I}m\left\{\int dr\, G^{+}(r,r;\varepsilon)\right\}. \tag{3. 26}$$

3.4 Potential Scattering

In considering scattering events, it is useful to separate the Hamiltonian H into two terms

$$H = H_0 + V, \tag{3. 27}$$

where H_0 is a reference system that permits all eigenvalues and eigenvectors to be calculated, and V is an interaction term that acts as a perturbation to the reference system.

We can now recast the time independent Schrödinger equation (3. 2) as a single-electron scattering problem,

$$\left[\varepsilon - \nabla^2\right] |\Psi\rangle = V(\vec{r})|\Psi\rangle, \tag{3. 28}$$

where the reference system H_0 is the free-particle kinetic energy operator ∇^2, the interaction term V is a muffin-tin potential $V(\vec{r})$ and ε is the single-electron energy eigenvalue. This prescription for the scattering problem allows $V(\vec{r})|\Psi\rangle$ to be regarded as a source term by formal analogy to the inhomogeneous differential equation (3.16).

3.5 The Lippmann-Schwinger Equations

The boundary conditions for physically real solutions require $|\Psi\rangle \rightarrow |\Phi\rangle$ as $V(\vec{r}) \rightarrow 0$, where $|\Phi\rangle$ solves the homogeneous equation

$$\left[\varepsilon - \nabla^2\right] |\Phi\rangle = 0, \tag{3. 29}$$

and where ε is the same energy eigenvalue as in the full problem (3. 28). The formal solution satisfying these requirements is provided by the

Lippmann-Schwinger equation [3.10],

$$|\Psi\rangle = |\Phi\rangle + G_0^+ V(\vec{r})|\Psi\rangle, \tag{3.30a}$$

where we have written G_0^+ to emphasise that the Green function belongs to the reference system. The Lippmann-Schwinger equation may also be written as

$$|\Psi\rangle = |\Phi\rangle + G_0^+ \mathrm{t}\, |\Phi\rangle, \tag{3.30b}$$

which introduces the operator t that satisfies

$$\mathrm{t}\, |\Phi\rangle = V(\vec{r})|\Psi\rangle. \tag{3.31}$$

It is important to be clear about the meaning of this last relationship; it asserts that we can construct the effect of the interaction solely from the Hilbert space of the reference system, and that our problem is solved once we have a means to calculate t. Before progressing with this scheme, we shall first examine the Lippmann-Schwinger equation in the position representation, since this will provide some valuable insights into the nature of the scattered state.

The free-space Green function (belonging to the operator ∇^2) in the position representation behaves like a spherical wave:

$$G_0^+(|\vec{r} - \vec{r}'|) = \frac{e^{\imath k|\vec{r}-\vec{r}'|}}{4\pi|\vec{r} - \vec{r}'|}, \tag{3.32}$$

where once again we have set $k = \sqrt{\varepsilon}$. If we allow $\vec{r}' \to \infty$ and introduce suitable simplifying approximations [3.11] we can obtain the asymptotic form of the scattered state

$$\underset{r \to \infty}{\Psi_k(\vec{r})} \sim e^{i\vec{k}\cdot\vec{r}} - \frac{e^{ikr}}{4\pi r}\int_{-\infty}^{\infty} dr' e^{-i\hat{k}\vec{r}'}\, V(\vec{r}')\Psi_k(\vec{r}'), \tag{3.33}$$

where $\hat{k} = k\hat{r}$. The scattered state $\Psi_k(\vec{r})$ is therefore a superposition of both an incident plane wave and a spherical scattered wave. Since $\hat{k}$ depends only on the direction of $\hat{r}$ we can consider the integral in (3.33) to be angular; this integral is the scattering amplitude $\left\langle \Phi_{\hat{k}} \right| V \left| \Psi_k \right\rangle$ that defines the matrix element of the potential for scattering into a free state propagating in the $\hat{k}$ direction. The scattering amplitude may be used to establish a simple formula for the t matrix.

Recalling the defining relation for the t operator (3.31), we can construct the 'on the energy shell' t matrix element, where $\vec{k} = \hat{k}$, in a similar manner. In an angular momentum representation we obtain

$$\mathrm{t}_l = \int_{-\infty}^{\infty} d\vec{r} \int_{-\infty}^{\infty} d\vec{r}' j_l(r)\mathrm{t}_l(r,r') j_l(r') Y_L(\hat{r}) Y_L^*(\hat{r}'). \tag{3.34}$$

The t matrix element (3.34) may be used, together with the angular momentum decomposition of G_0^+;

$$G_0^+(\vec{r},\vec{r}') = -ik\sum_L j_l(r_<) Y_L(\hat{r}_<) h_l^+(r_>) Y_L^*(\hat{r}_>), \tag{3.35}$$

where $r_<(r_>)$ denotes the lesser (greater) of vectors $\vec{r}$ and $\vec{r}'$, to construct the Lippmann-Schwinger equation for the radial wave function $R_l(r,k)$ [3.2]. By performing the necessary algebraic trickery, we can derive the free-space form of the radial wave function that must be satisfied on the surface of a muffin-tin sphere,

$$e^{i\delta_l(k)} R_l(r,k) = j_l(kr) - ik\mathrm{t}_l h_l^+(kr), \quad (r \geq S). \tag{3.36}$$

Substituting the phase shift form of $R_l(r,k)$ (3.11) into this boundary condition produces an expression for the t matrix element in terms of the phase shifts:

$$\mathrm{t}_l(k) = -\frac{e^{i\delta_l(k)}}{k} \sin\delta_l(k). \tag{3.37}$$

3.6 The Scattering Solutions of the Radial Wave Equation

An alternative radial wave function $Z_l(r,k)$ was introduced by Faulkner and Stocks [3.12], which has the free-space form

$$Z_l(r,k) = j_l(kr)\mathrm{t}_l^{-1} - ikh_l^+(kr), \quad (r \geq S). \tag{3.38}$$

Comparing equation (3.38) with (3.36) we can easily see that the two functions are related:

$$e^{i\delta_l(k)} R_l(r,k) = \mathrm{t}_l(k)\, Z_l(r,k). \tag{3.39}$$

It is important to understand the applicability of these solutions, and to illustrate their differences we can consider their behaviour when subject to a null scattering event.

3.6.1 Null Scattering Events

In the absence of a scattering potential we have no means to change the state of a freely propagating wave and $\delta_l(k) = 0$. With this condition the radial wave function (3.11) simply reduces to a spherical Bessel function, and we also find on examining (3.37) that $\mathrm{t}_l(k) = 0$.

It is interesting to see how the case $\mathrm{t}_l(k) = 0$ affects the scattered state $\Psi_k(\vec{r})$ when this is defined in terms of $R_l(r,k)$. Consistency

demands that the asymptotic form of the scattered state (3.33) should be related to its eigenfunction expansion (3.3) in the appropriate limit

$$\Psi_k(r) = \sum_L a_L(k) R_l(r) Y_L(\hat{r}),$$

and this allows the coefficients $a_L(k)$ to be determined. The analysis gives [3.13]:

$$\Psi_k(\vec{r}) = 4\pi \sum_L i^l e^{i\delta_l(k)} R_l(r,k) Y_L^*(\hat{k}) Y_L(r), \tag{3.40}$$

and substituting the condition $\delta_l(k) = 0$, we find that we reproduce Bauer's expansion for a plane wave in an angular momentum basis,

$$e^{i\vec{k}\cdot\vec{r}} = 4\pi \sum_L i^l j_l(kr) Y_L^*(\hat{k}) Y_L(\hat{r}). \tag{3.41}$$

Not surprisingly, we have found that a phase shift $\delta_l(k) = 0$ conditions the scattered state to be a pure incident wave; or equivalently, that $\mathrm{t}_l(k)$ is responsible for generating the scattered *wave* in the scattered *state* .

The null scattering event for $Z_l(r,k)$ makes this function singular because it behaves as t_l^{-1}, and we can assert that the relationship between the two radial wave functions (3.39) no longer holds. Consequently, we recognise that the $Z_l(r,k)$are only usefully defined in the presence of a scattering potential, and that they fully warrant their designation as the 'scattering solutions' of the radial wave equation.

We shall now complete this chapter by reviewing multiple-scattering theory in the spirit of Gyorffy and Stott [3.14], which will lead to Faulkner and Stock's expression for the multiple scattering Green function [3.12].

3.7 The Scattering Path Operator

To effect the transition from single to multiple scattering theory, we consider a total potential $V(\vec{r})$ to be derived from an assembly of muffin-tin potentials $v^i(\vec{r})$ located at points $\vec{R}_i$;

$$V(\vec{r}) = \sum_i v^i(\vec{r} - \vec{R}_i). \tag{3.42}$$

For brevity, we shall assume that the spatial dependence is understood and neglect to write this further here.

Recalling the defining equation for the Green function G^+ (3.20), we can rewrite the scattering problem (3.28) for the potential V as the operator equation;

$$\left[-\left\{\nabla^2 + \varepsilon\right\} + V \right] G^+ = 1, \tag{3.43}$$

where 1 is again the identity operator. The expression in braces is the free-space Hamiltonian, which has the free-space Green function G_0^+. Taking advantage of this, we can write the operator equation

$$\left[-\left(G_0^+\right)^{-1} + V \right] G^+ = 1, \tag{3.44}$$

and thus obtain the full Green function G^+ as a perturbation about the free-space Green function G_0^+,

$$G^+ = G_0^+(1 - VG_0^+)^{-1}. \tag{3.45}$$

Expanding (3.44) (taking care over the non-commutativity of the operators) produces the perturbation series,

$$G^+ = G_0^+ + G_0^+VG_0^+ + G_0^+VG_0^+VG_0^+ + \ldots ,$$

which can also be written more compactly as a Dyson equation:

$$G^+ = G_0^+ + G_0^+ V G^+ \qquad (3.46\text{ a})$$

$$= G_0^+ + G^+ V G_0^+ . \qquad (3.46\text{ b})$$

The Dyson equation (3.46) is formally solved through the total scattering operator T:

$$G^+ = G_0^+ + G_0^+ \mathrm{T}\, G_0^+ , \qquad (3.47)$$

where

$$\mathrm{T} = \mathrm{V} + \mathrm{V} G_0^+ \mathrm{T} \qquad (3.48\text{ a})$$

$$= \mathrm{V} + \mathrm{T}\ G_0^+ \mathrm{V}. \qquad (3.48\text{ b})$$

These relations are noteworthy since it is a simple task to reproduce the Lippmann-Schwinger equations (3.30) from (3.48).

We have now come to the crux of this analysis. Because we have not made any additional assumptions about the potential V in deriving the expressions above, the results (3.48) are completely general. Consequently, we can relate the single scattering operators t^i associated with the potentials v^i in a similar manner to relations (3. 48);

$$\mathrm{t}^i = v^i + v^i G_0^+ \mathrm{t}^i = (1 - G_0^+ v^i)^{-1} v^i \qquad (3.49\text{ a})$$

$$= v^i + \mathrm{t}^i G_0^+ v^i = v^i (1 - G_0^+ v^i)^{-1}. \qquad (3.49\text{ b})$$

We can also relate the total scattering operator T to a particular site potential v^i by a direct comparison of equation (3. 42) with (3. 48):

$$\mathrm{T} = \sum_i v^i + \sum_{i,n} v^i G_0^+\ \mathrm{T}. \qquad (3.50)$$

What we are aiming to do is to express the total scattering T in terms of

individual scattering contributions from the potentials v^i. To achieve this, we introduce the partial scattering operator Q^i, such that:

$$\mathrm{T} = \sum_i Q^i. \tag{3.51}$$

The difference between the operators Q^i and t^i should be clear: Q^i denotes the scattering from site i in the presence of all other (multiple) scattering events within the assembly, whereas t^i denotes the (single) scattering solely from the potential v^i.

Hence, we can replace the T operator in equation (3. 49):

$$\sum_i Q^i = \sum_i v^i + \sum_{i,n} v^i G_0^+ Q^n, \tag{3.52}$$

which allows us to isolate the contribution from site i,

$$\begin{aligned} Q^i &= v^i + \sum_n v^i G_0^+ Q^n, \\ &= v^i + v^i G_0^+ Q^i + \sum_{n \neq i} v^i G_0^+ Q^i. \end{aligned} \tag{3.53}$$

This last expression may be reduced further by using the single scattering t^i relations (3.47);

$$Q^i = \underbrace{\mathrm{t}^i}_{Direct} + \underbrace{\sum_{n \neq i} \mathrm{t}^i G_0^+ Q^i}_{Assembly}, \tag{3.54}$$

and we appear to have achieved our objective; equation (3.53) relates the contribution to the total scattering from the potential v^i as the sum of all scattering events within the assembly that contribute an incident wave to this site, plus the scattering from the direct wave incident to this site.

Gyorffy and Stott [3.14] further decomposed the partial scattering

operator Q^i to represent the elastically scattered elements of the total scattering operator T, by introducing the scattering path operator τ^{ij} where:

$$Q^i = \sum_j \tau^{ij}, \tag{3.55}$$

and thus,

$$\mathrm{T} = \sum_i Q^i = \sum_{i,j} \tau^{ij}. \tag{3.56}$$

By considering equations (3.54) and (3.55), the scattering path operator can be related to the single scattering operators;

$$\begin{aligned} \tau^{ij} &= \mathrm{t}^i \delta_{i,j} + \mathrm{t}^i G_0^+ \sum_{p \neq i} \tau^{pj} \\ &= \mathrm{t}^i \delta_{i,j} + \sum_{p \neq j} \mathrm{t}^j G_0^+ \tau^{ip}, \end{aligned} \tag{3.57}$$

where $\delta_{i,j}$ is the Kronecker delta function.

3.8 Calculating the τ Matrix

If we project the defining equation for the scattering path operator (3.57) into the position representation, and adjust the origin of the coordinate system to locate the scattering sites, we obtain;

$$\begin{aligned} \tau^{ij}(\vec{r}+\vec{R}_i, \vec{r}'+\vec{R}_j) &= \mathrm{t}^i(\vec{r}+\vec{R}_i, \vec{r}'+\vec{R}_j)\delta_{i,j} \\ &+ \sum_{n \neq i} \int_0^{S_1} d\vec{r}_1 \int_0^{S_2} d\vec{r}_2 \Big[\mathrm{t}^i(\vec{r}+\vec{R}_i, \vec{r}_1+\vec{R}_i) \\ &\times G_0^+(\vec{r}_1+\vec{R}_i, \vec{r}_2+\vec{R}_n) \tau^{ij}(\vec{r}_2+\vec{R}_n, \vec{r}'+\vec{R}_j) \Big]. \end{aligned} \tag{3.58}$$

The limits on the integrals arise from the muffin-tin character of the potential; since $v^i(\vec{r}) = 0$ outside the boundary of the muffin-tin sphere we can assert, after examining (3. 49) and (3. 57), that both $\mathbf{t}^i$ and τ^{ij} have zero value unless $\vec{r}_1$ lies within site i and $\vec{r}_2$ lies within site j, and hence that $\vec{r}_1, \vec{r}_2$ are constrained to lie within the boundaries of the muffin-tin spheres S_1, S_2 respectively.

The spatial restrictions introduced by this geometry allow a convenient expansion of the free-space Green function G_0^+, which simplifies equation (3.57) considerably.

By examining G_0^+ in the position representation (3.32), we find it is permissible to write

$$G_0^+(\vec{r}_1 + \vec{R}_i, \vec{r}_2 + \vec{R}_n) = G_0^+(\vec{r}_1, \vec{r}_2 - \vec{R}_{in}), \tag{3. 59}$$

where $\vec{R}_{in} \equiv \vec{R}_i - \vec{R}_n$; and substituting the RHS of (3.59) into the angular momentum decomposition of G_0^+ (3.34) produces:

$$G_0^+(\vec{r}_1 + \vec{R}_i, \vec{r}_2 + \vec{R}_n) = -ik\sum_L j_l(\vec{r}_1) Y_L^*(\hat{r}_1) h_l^+(\vec{\Re}) Y_L(\hat{\Re}). \tag{3. 60}$$

where $\vec{\Re} = \vec{r}_2 - \vec{R}_{in}$.

We can now make use of a beautiful relationship that expands a spherical Hankel function on one site, in terms of a spherical Bessel function centred on a different site;

$$-ik h_l^+(\vec{\Re}) Y_L(\hat{\Re}) = \sum_{L'} g_{LL'}^{ij} j_{l'}(r_2) Y_{L'}(\hat{r}_2). \tag{3. 61}$$

We note that this expansion is only valid if $|\vec{r}_2| < |\vec{R}_{in}|$, which is

certainly true for the integrals above (3.57). The $g^{ij}_{LL'}$ in equation (3.61) are the real-space structure constants:

$$g^{ij}_{LL'} = -4\pi ik(-1)^{m_l(l'-l)}\sum_{L} i^{-l_1} C(\bar{L},L,L_1) h^{+}_{L_1}(r_{nm}) Y_{L_1}(\hat{r}_{nm}), \qquad (3.62)$$

with the Gaunt factors $C(\bar{L},L',L_1)$ defined as

$$C(\bar{L},L',L_1) \equiv \int d\hat{r}\, Y^{*}_{\bar{L}}(\hat{r}) Y_{L'}(\hat{r}) Y_{L_1}(\hat{r}). \qquad (3.63)$$

By using the expansion (3.61) to define the Green function (3.60) we have effectively given it a local basis;

$$G^{+}_{0}(\vec{r}_1+\vec{R}_i,\vec{r}_2+\vec{R}_n) = \sum_{L,L'} j_l(\vec{r}_1) Y^{*}_{L}(\hat{r}_1)\, g^{ij}_{L,L'}\, j_{l'}(r_2) Y_{L'}(\hat{r}_2). \qquad (3.64)$$

If we now substitute this local basis Green function (3.64) into the real-space τ matrix equation (3.58), recognise the angular momentum representation for the 'on the energy shell' τ matrix elements;

$$\tau^{ij}_{L,L'} = \int d\vec{r} \int d\vec{r}'\, j_l(\vec{r}) Y_L(\hat{r}_i) \tau^{ij}_{L,L'}(\vec{r}+\vec{R}_i,\vec{r}'+\vec{R}_j) j_l(\vec{r}') Y^{*}_{L'}(\hat{r}'), \qquad (3.65)$$

and also recall the analogous matrix elements for the t matrix (3.33), we produce;

$$\tau^{ij}_{LL'} = \mathrm{t}^{i}_{LL'}\delta_{ij} + \sum_{n\neq i} \mathrm{t}^{i}_{LL'}\, g^{in}_{L,L_2}\, \tau^{nj}_{L,L'}, \qquad (3.66)$$

which is the fundamental equation of multiple scattering theory.

It is easier to understand the structure of (3.66) as a matrix equation [3.15]; if we define $\tau^{ij}_{LL'} = \underline{\tau}$, $\mathrm{t}^{i}_{LL'}\delta_{ij} = \underline{\mathrm{t}}$ and let $(1-\delta_{ij})g^{in}_{L_1L_2} = \underline{\Gamma}$, where 1 is the unit matrix, then (3. 66) becomes:

$$\underline{\tau} = \underline{t} + \underline{t}\,\underline{\Gamma}\,\underline{\tau} \qquad (3.67\,a)$$

$$= \left[\underline{t}^{-1} - \underline{\Gamma}\right]^{-1}. \qquad (3.67\,b)$$

We can now see explicitly how both local ($\underline{t}$) and global ($\underline{\Gamma}$) quantities contribute separately to the τ matrix.

3.9 The Multiple Scattering Green Function

Faulkner and Stocks [3.12] derived the multiple scattering Green function by substituting $\mathrm{T} = \sum \tau^{ij}$ into the Dyson equation (3.47) and projecting the resulting equation into a real-space representation. By considering the site dependent geometry as two separate cases, they produced:

$$G^{+}(\vec{r},\vec{r}';\varepsilon) = \sum_{i,j,L,L'}\Big[Z_L^i(\vec{r};\varepsilon)\tau(\vec{r},\vec{r}';\varepsilon)Z_{L'}^j(\vec{r}';\varepsilon)Y_L^*(\hat{r})Y_{L'}(\hat{r}') - Z_L^i(\vec{r}_<;\varepsilon)j_l^i(\vec{r}_>;\varepsilon)Y_L^*(\hat{r}_<)Y_{L'}(\hat{r}_>)\delta_{L,L'}\delta_{i,j}\Big], \qquad (3.68)$$

where Z_L^i, j_l^i are the regular and irregular scattering solutions for the ith potential. The Green function (3.68) thus describes the scattering (per angular momentum channel) between two separated sites i,j when $\vec{r},\vec{r}'$ fall within these sites, and describes the scattering at a single site when $\vec{r},\vec{r}'$ both fall within the same site. Since the irregular scattering solution is only included for the single site case, it can sensibly be interpreted as a "self-energy" term.

The Green function (3.68) has two properties which make it useful for the systems studied later in this thesis; it allows differing potentials derived from different atomic systems to be used, and it produces real values with real energies.

We shall show how the Green function (3. 68) can be modified to model spectroscopic phenomena in the next chapter, when we discuss the real-space photocurrent equation.

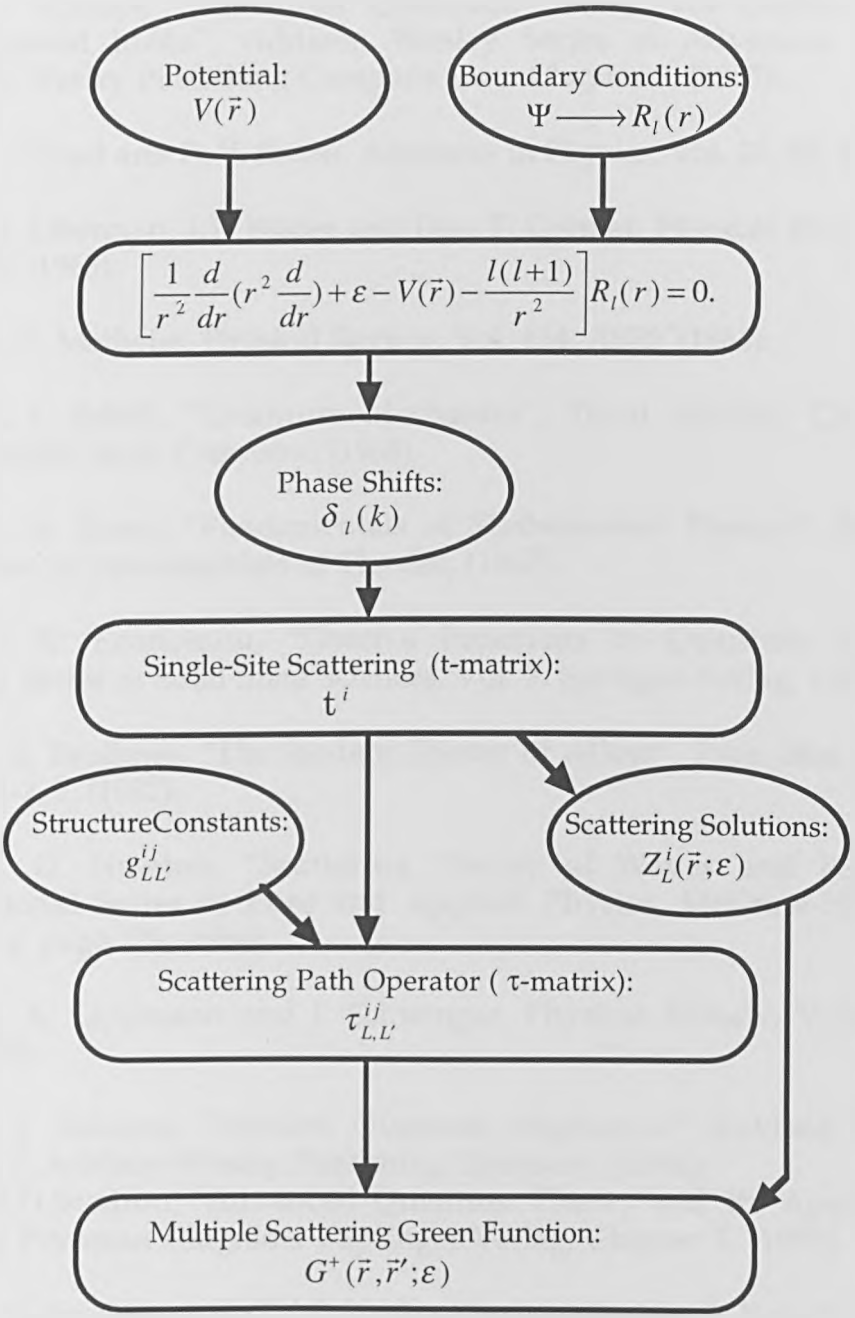

Figure 3.b: a flow diagram illustrating the development of the key concepts of multiple scattering theory and how these may be used to calculate the Green function.

3.10 References

[3.1] P. Roman, ''Advanced Quantum Theory, An Outline of the Fundamental Ideas'', Addison Wesley Series in Advanced Physics, Addison Wesley Publishing Company Inc., Chapter 3, (1965).

[3.2] P. Lloyd and P. V. Smith, Advances in Physics, Vol. 21, 69, (1972).

[3.3] D. Liberman, J.T. Waber and Don T. Cromer, Physical Review, Vol. 137, A27, (1965).

[3.4] L. F. Matheiss, Physical Review, Vol. 134, A970, (1964).

[3.5] L. I. Schiff, "Quantum Mechanics", Third Edition, Chapter 4, McGraw-Hill Book Company, (1968).

[3.6] E. A. Kraut, "Fundamentals of Mathematical Physics", McGraw-Hill Series in Fundamentals of Physics, (1967).

[3.7] E. N. Economou, "Green's Functions in Quantum Physics", Springer Series in Solid State Sciences, Vol. 7, Springer-Verlag, (1979).

[3.8] J. S. Faulkner, "The Modern Theory of Alloys", Prog. Mat. Sci.,Vol 27, No. 1-2, 1, (1982).

[3.9] R. G. Newton, "Scattering Theory of Waves and Particles", International Series in Pure and Applied Physics, McGraw-Hill Book Company, page 179, (1966).

[3.10] B. A. Lippmann and J. Schwinger, Physical Review, Volume 79, 469, (1950).

[3.11] J. J. Sakurai, "Modern Quantum Mechanics", Revised Edition, Chapter 7, Addison-Wesley Publishing Company, (1994);
M.D.Scadron "Advanced Quantum Theory and Its Applications Through Feynman Diagrams", Springer-Verlag, Chapter 7, (1979).

[3.12] J. S. Faulkner and G. M. Stocks, Physical Review B, Vol. 21, 8, 3222-3244, (1980).

[3.13] See, for instance, P. Roman, "Advanced Quantum Theory", *(ibid)*, pages 159-165.

[3.14] B. L. Gyorffy and M. J. Stott in "Band Structure Spectroscopy of Metals and Alloys", D. J. Fabian and L. M. Watson, (ed.s), Academic Press, (1973).

[3.15] P. J. Durham, "Multiple Scattering Theory Basic Working Notes", (private communication).

[3.16] A. Messiah, "Quantum Mechanics", Volume 1, North Holland Publishing Company, Chapter 5, (1961).

Chapter 3

Scattering Theory and the Multiple Scattering Green Function

The purpose of this chapter is to establish the boundary conditions for scattering events, and to show how these lead to the multiple scattering Green function, since it is this Green function which underpins the photocurrent equation discussed in the next chapter. Rydberg units are used throughout this chapter, in which $\hbar^2 = 2m = e = 1$.

We begin with an account of the radial wave equation and phase shift analysis before discussing briefly the solution of inhomogeneous differential equations by Green functions. The Green function is then related to the density of states. Next, we present an analysis of potential scattering, which introduces the Lippmann-Schwinger equations, before discussing Gyorffy's scattering path operator and the multiple scattering Green function.

3.1 A Framework for Scattering Theory

The quantum mechanical theory of scattering is founded on the principle that it is the asymptotic scattering state which is an observable [3.1]; it is not necessary to know the exact microphysical interactions that occur during the brief interval of the scattering event and consequently

scattering can be modelled as a 'black box' process, in which an initial 'input' state is converted into an 'output' scattered state.

Although a more general treatment of scattering theory allows for energy exchanges we need only consider elastic scattering, since it is this so-called 'on the energy shell' condition (conservation of kinetic energy) which allows the scattered state to be derived from the phase shifts [3.2]. This will be discussed in more detail below.

The multiple scattering theory reviewed here is a single-electron theory that neatly divides the electronic structure problem into two parts; local (atomic) scattering properties are calculated and then used with the global (structural) properties of a distributed assembly of those scatterers to calculate observables. In applying this technique to problems of electronic structure, we assume that the potentials which act as scattering centres have been generated self-consistently using methods akin to those discussed in the previous chapter. The potential thus contains all the many-electron interactions, and the single-electron only interacts with the potential.

3.2 The Radial Wave Equation and Phase Shifts

In what follows we shall be investigating the effects of scattering from a spatially finite spherical potential; the so-called muffin-tin potential which has the form [3.3, 3.4]

$$V(\vec{r}) = \begin{cases} V(\vec{r}) - C & for\ r \le S \\ C & for\ r \ge S \end{cases} \tag{3.1}$$

where S is the radius of the muffin-tin sphere and C is a constant that denotes the interstitial region between the muffin-tin spheres. It is convenient to assume that $C = 0$ in what follows, without loss of generality (see figure 3.a, overleaf).

If we incorporate a muffin-tin potential $V(\vec{r})$ into the Hamiltonian for the time independent Schrödinger equation, we obtain the familiar energy eigenvalue problem:

$$\left[\nabla^2 + V(\vec{r})\right] |\Psi\rangle = \varepsilon |\Psi\rangle, \tag{3.2}$$

where ∇^2 is the kinetic energy operator and ε is the single-electron energy eigenvalue. For non-core states we can set $k = \sqrt{\varepsilon}$, and the solution

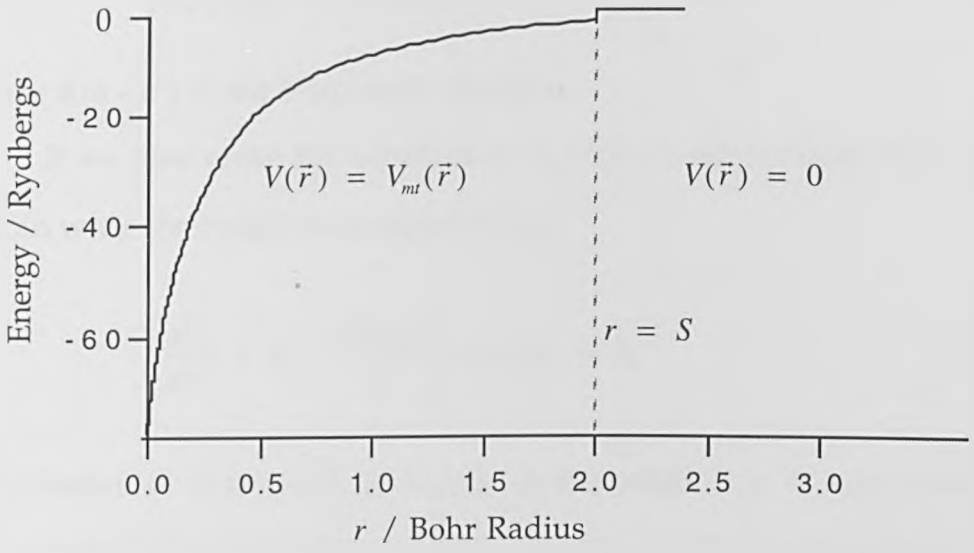

Figure 3.a: showing the different regions in the muffin-tin potential. The potential shown has been adapted from an LMASA-46 potential for tungsten.

to (3. 2) can be written as:

$$\Psi_k(r) = \sum_L a_L(k) R_l(r) Y_L(\hat{r}), \tag{3.3}$$

where $Y_L(\hat{r})$ is a spherical harmonic with $\hat{r}$ a unit vector and $L = l,m$ denotes the angular and spin momentum indices respectively, $a_L(k)$ is the expansion coefficient and $R_l(r)$ is the radial wave function that satisfies the radial wave equation,

$$\left[\frac{1}{r^2}\frac{d}{dr}(r^2\frac{d}{dr}) + \varepsilon - V(\vec{r}) - \frac{l(l+1)}{r^2}\right] R_l(r) = 0. \tag{3.4}$$

For a unique solution to the eigenvalue problem (3.2) we require $\Psi_k(\vec{r})$ to be regular as $r\rightarrow\infty$ and normalisable. The difficulties of normalisation in the continuous spectrum of the eigenvalue problem are well known [3.16] and we shall assume that $\Psi_k(\vec{r})$ is normalised such that

$$\langle \Psi_{k'} | \Psi_k \rangle = \delta(k-k'), \tag{3.5}$$

where $\delta(k-k')$ is the Dirac delta function.

If we now make the substitution $u_l(r,k)=rR_l(r)$ and set $V(\vec{r}) = 0$, we can write the radial wave equation as

$$\left[\frac{d^2}{dr^2} + \varepsilon - \frac{l(l+1)}{r^2}\right] u_l(r,k) = 0. \tag{3.6}$$

The solution to (3.6) which is regular at the origin $r = 0$ is provided by the spherical Bessel function $j_l(kr)$, and we emphasise that this is the free-space solution in what follows. The spherical Bessel function has the asymptotic form [3.5]

$$j_l(kr) \underset{r\longrightarrow\infty}{\approx} \frac{1}{kr}\sin\left[kr - \frac{l\pi}{2}\right], \tag{3.7}$$

Another solution to equation (3.6) which is, however, irregular at the origin is the spherical Neumann function, $n_l(kr)$, with asymptotic form [3.5]

$$n_l(kr) \underset{r\longrightarrow\infty}{\approx} -\frac{1}{kr}\cos\left[kr - \frac{l\pi}{2}\right]. \tag{3.8}$$

We are now in a position to discuss the conceptual basis of phase shift analysis.

3.2.1 The Meaning of the Phase Shift

We can write the general free-space solution to equation (3.4) as

$$R_l(r,k) = B_l(k)j_l(kr) + C_l(k)n_l(kr), \tag{3.9}$$

where $B_l(k), C_l(k)$ are normalising coefficients. To obviate the irregular behaviour of $n_l(kr)$, we can choose $C_l(k) = 0$ whenever the solution needs to include the origin.

Since the asymptotic forms (3. 7) and (3.8) may be combined into

$$\underset{r\longrightarrow\infty}{R_l(r,k)} \approx \frac{1}{kr}\sin\left[kr - \frac{l\pi}{2} + \delta_l(k)\right], \tag{3.10}$$

the general solution has a phase $\delta_l(k)$, which is additional to the free-space solution. If we identify the free-space solution $j_l(kr)$ with an incident wave and, taking account of the restriction on the spatial domain for $n_l(kr)$, identify the spherical Neumann function with the scattered wave that radiates from the surface of the potential sphere, then we note that the extra phase $\delta_l(k)$ arises from the scattered wave. The coefficients in (3.9) can now be expressed in accordance with equation (3.10) so that a 'null' scattering event, characterised by $\delta_l(k) = 0$, coincides with the free-space solution everywhere. This is the 'phase shift' form of the radial wave function:

$$R_l(r,k) = \cos\delta_l(k)\, j_l(kr) + \sin\delta_l(k)\; n_l(kr). \tag{3.11}$$

We can also express the linear combination (3.9) in the complex plane

through the spherical Hankel functions [3.6],

$$h_l^{\pm}(kr) = j_l(kr) \pm i n_l(kr), \tag{3.12}$$

where $h_l^{+}(kr)$ is a spherical Hankel function of the first kind and $h_l^{-}(kr)$ is a spherical Hankel function of the second kind. These solutions behave asymptotically like spherical waves,

$$h_l^{\pm}(kr) \underset{r \to \infty}{\sim} \frac{i^{-(l+1)} e^{\pm ikr}}{kr}, \tag{3.13}$$

a property which makes them especially useful in scattering problems.

3.2.2 Calculating the Phase Shift

We can use the phase-shift form of the radial wave function to calculate $\delta_l(k)$ by considering the continuity of $R_l(r,k)$ at the boundary of the muffin-tin sphere. Continuity is established when both the function and its spatial-derivative have equal value across the boundary; that is, we require the logarithmic derivative $\beta_l(k)$ of the radial wave function evaluated at the muffin-tin boundary ($r = S$) to be

$$\beta_l(k) = \frac{1}{R_l(r,k)} \left(\frac{d R_l(r,k)}{dr} \right) \Bigg|_{r=S}. \tag{3.14}$$

With this matching condition for the wave function the phase shift can be calculated from the relationship

$$\tan \delta_l(k) = \frac{k n_l'(kS) - \beta_l(k) n_l(kS)}{k j_l'(kS) - \beta_l(k) j_l(kS)}, \tag{3.15}$$

where the primed functions have been differentiated with respect to the argument kr.

3.3 Differential Equations and Green Functions

In the theory of linear differential equations, the inhomogeneous equation has the form

$$L_r|\Psi\rangle = \sigma(r), \tag{3.16}$$

where L_r is a linear differential operator and $\sigma(r)$ is called the source term [3.6]. The corresponding homogeneous equation is a special case of (3.16) when $\sigma(r) = 0$; its solution is known as the complementary function and we will write this as $|\Phi\rangle$. The inhomogeneous differential equation (3.16) is solved by a linear combination of the complementary function and any $|\Psi\rangle$ that satisfies the prescribed boundary conditions for the full problem; this latter solution is the particular integral and we can find it by considering the following operator relationship,

$$L_r^{-1} L_r = 1, \tag{3.17}$$

where L_r^{-1} is the inverse operator to L_r and 1 is the identity operator. Consequently, equation (3.16) may be solved by applying L_r^{-1} on the left and using the result (3.17). We then have the particular integral,

$$|\Psi\rangle = L_r^{-1}\sigma(r). \tag{3.18}$$

The general solution of the inhomogeneous equation (3. 16) is therefore,

$$|\Psi\rangle = |\Phi\rangle + L_r^{-1}\sigma(r). \tag{3.19}$$

Since L_r is a differential operator, the inverse operator is an integral operator and the 'solution' recasts (3.16) into an equivalent integral equation which must satisfy the same boundary conditions. The

integral equation may be solved when L_r^{-1} is known explicitly.

The inverse operator called the Green function $G(r, r')$ uses an extra degree of freedom r' as an additional parameter and we adopt the convention that

$$G(r, r')\ L_r = \delta(r - r'). \tag{3.20}$$

This is the defining equation for the Green function belonging to the differential operator L_r. It may be interpreted as the response of the system to a unit source at r'. The extra degree of freedom also serves another purpose by shifting our attention to any region of interest within the space of the variable r, so it is not surprising that elsewhere in the literature $G(r, r')$ is also called a propagator.

3.3.1 Green Functions and the Density of States

The Green function can be related to an eigenfunction which is complete in Hilbert space via its modal expansion [3.7]. Calling the eigenfunction $|\Psi_n\rangle$, this is written as,

$$G^{\pm}(r, r'; \varepsilon) = \lim_{\eta \to 0^+} \sum_n \frac{|\Psi_n\rangle\langle\Psi_n|}{\varepsilon - \varepsilon_n \pm i\eta}\ , \tag{3.21}$$

where ε_n denotes the eigenvalue, $i\eta$ is a purely imaginary infinitesimal and the summation includes integration for any continuous part of the eigenvalue spectrum. Consequently, the Green function exists only for $\varepsilon \neq \varepsilon_n$, since the eigenvalues ε_n appear as simple poles on the real axis for the discrete part of the spectrum and as a natural boundary in the continuum. The singular behaviour is 'smoothed' by the imaginary infinitesimal $i\eta$, which displaces the poles from the real axis and into the complex plane.

The limiting process which recovers the Green function serves as an additional boundary condition and more than one Green function can be constructed. We shall choose the 'outgoing' Green function G^+ as the most suitable for what follows; we shall see later that G^+ corresponds to a divergent spherical wave, whereas the alternative choice of G^- gives a spherically convergent wave - a difficult state to prepare in nature.

We can now derive an expression for the density of states [3.8]. The trace of a Green function is obtained by analogy with the trace of a matrix. Setting $r = r'$ and integrating over all space, we find

$$\int dr\, G^+(r,r;\varepsilon) = \underset{\eta \to 0^+}{Lim} \int dr \sum_n \frac{|\Psi_n\rangle\langle\Psi_n|}{\varepsilon - \varepsilon_n + i\eta} . \qquad (3.22)$$

We can make use of the formal identity [3.9]

$$\underset{\eta \to 0^+}{Lim} \sum_n \frac{1}{\varepsilon - \varepsilon_n + i\eta} = \mathscr{P}.\mathscr{P}.\left(\frac{1}{\varepsilon - \varepsilon_n}\right) - i\pi\delta(\varepsilon - \varepsilon_n), \quad (3.23)$$

where $\mathscr{P}.\mathscr{P}.$ denotes the principal part, to establish the relationship

$$\delta(\varepsilon - \varepsilon_n) = -\frac{1}{\pi}\, \mathscr{I}m \left\{ \underset{\eta \to 0^+}{Lim} \frac{1}{\varepsilon - \varepsilon_n + i\eta} \right\}, \qquad (3.24)$$

which gives, on inspecting the trace of the Green function (3. 22),

$$-\frac{1}{\pi}\, \mathscr{I}m \left\{ \int dr\, G^+(r,r;\varepsilon) \right\} = \sum_n \delta(\varepsilon - \varepsilon_n). \qquad (3.25)$$

This last expression is the density of states, because it simply counts the number of eigenvalues within a given interval. Denoting the density of states by $\rho(\varepsilon)$, we can therefore write explicitly

$$\rho(\varepsilon) = -\frac{1}{\pi} \mathcal{I}m\left\{\int dr\, G^{+}(r,r;\varepsilon)\right\}. \tag{3. 26}$$

3.4 Potential Scattering

In considering scattering events, it is useful to separate the Hamiltonian H into two terms

$$H = H_0 + V, \tag{3. 27}$$

where H_0 is a reference system that permits all eigenvalues and eigenvectors to be calculated, and V is an interaction term that acts as a perturbation to the reference system.

We can now recast the time independent Schrödinger equation (3. 2) as a single-electron scattering problem,

$$\left[\varepsilon - \nabla^2\right] |\Psi\rangle = V(\vec{r})|\Psi\rangle, \tag{3. 28}$$

where the reference system H_0 is the free-particle kinetic energy operator ∇^2, the interaction term V is a muffin-tin potential $V(\vec{r})$ and ε is the single-electron energy eigenvalue. This prescription for the scattering problem allows $V(\vec{r})|\Psi\rangle$ to be regarded as a source term by formal analogy to the inhomogeneous differential equation (3.16).

3.5 The Lippmann-Schwinger Equations

The boundary conditions for physically real solutions require $|\Psi\rangle \rightarrow |\Phi\rangle$ as $V(\vec{r}) \rightarrow 0$, where $|\Phi\rangle$ solves the homogeneous equation

$$\left[\varepsilon - \nabla^2\right] |\Phi\rangle = 0, \tag{3. 29}$$

and where ε is the same energy eigenvalue as in the full problem (3. 28). The formal solution satisfying these requirements is provided by the

Lippmann-Schwinger equation [3.10],

$$|\Psi\rangle = |\Phi\rangle + G_0^+ V(\vec{r})|\Psi\rangle, \tag{3.30a}$$

where we have written G_0^+ to emphasise that the Green function belongs to the reference system. The Lippmann-Schwinger equation may also be written as

$$|\Psi\rangle = |\Phi\rangle + G_0^+ \mathrm{t}\, |\Phi\rangle, \tag{3.30b}$$

which introduces the operator t that satisfies

$$\mathrm{t}\, |\Phi\rangle = V(\vec{r})|\Psi\rangle. \tag{3.31}$$

It is important to be clear about the meaning of this last relationship; it asserts that we can construct the effect of the interaction solely from the Hilbert space of the reference system, and that our problem is solved once we have a means to calculate t. Before progressing with this scheme, we shall first examine the Lippmann-Schwinger equation in the position representation, since this will provide some valuable insights into the nature of the scattered state.

The free-space Green function (belonging to the operator ∇^2) in the position representation behaves like a spherical wave:

$$G_0^+(|\vec{r} - \vec{r}'|) = \frac{e^{ik|\vec{r}-\vec{r}'|}}{4\pi|\vec{r} - \vec{r}'|}, \tag{3.32}$$

where once again we have set $k = \sqrt{\varepsilon}$. If we allow $\vec{r}' \to \infty$ and introduce suitable simplifying approximations [3.11] we can obtain the asymptotic form of the scattered state

$$\underset{r \to \infty}{\Psi_k(\vec{r})} \sim e^{i\vec{k}\vec{r}} - \frac{e^{ikr}}{4\pi r}\int_{-\infty}^{\infty} dr' e^{-i\hat{k}\vec{r}'} V(\vec{r}')\Psi_k(\vec{r}'), \tag{3.33}$$

where $\hat{k} = k\hat{r}$. The scattered state $\Psi_k(\vec{r})$ is therefore a superposition of both an incident plane wave and a spherical scattered wave. Since $\hat{k}$ depends only on the direction of $\hat{r}$ we can consider the integral in (3.33) to be angular; this integral is the scattering amplitude $\left\langle \Phi_{\hat{k}} \right| V \left| \Psi_k \right\rangle$ that defines the matrix element of the potential for scattering into a free state propagating in the $\hat{k}$ direction. The scattering amplitude may be used to establish a simple formula for the t matrix.

Recalling the defining relation for the t operator (3.31), we can construct the 'on the energy shell' t matrix element, where $\vec{k} = \hat{k}$, in a similar manner. In an angular momentum representation we obtain

$$\mathrm{t}_l = \int_{-\infty}^{\infty} d\vec{r} \int_{-\infty}^{\infty} d\vec{r}' j_l(r)\mathrm{t}_l(r,r') j_l(r') Y_L(\hat{r}) Y_L^*(\hat{r}'). \tag{3.34}$$

The t matrix element (3.34) may be used, together with the angular momentum decomposition of G_0^+;

$$G_0^+(\vec{r},\vec{r}') = -ik\sum_L j_l(r_<) Y_L(\hat{r}_<) h_l^+(r_>) Y_L^*(\hat{r}_>), \tag{3.35}$$

where $r_<(r_>)$ denotes the lesser (greater) of vectors $\vec{r}$ and $\vec{r}'$, to construct the Lippmann-Schwinger equation for the radial wave function $R_l(r,k)$ [3.2]. By performing the necessary algebraic trickery, we can derive the free-space form of the radial wave function that must be satisfied on the surface of a muffin-tin sphere,

$$e^{i\delta_l(k)} R_l(r,k) = j_l(kr) - ik\mathrm{t}_l h_l^+(kr), \quad (r \geq S). \tag{3.36}$$

Substituting the phase shift form of $R_l(r,k)$ (3.11) into this boundary condition produces an expression for the t matrix element in terms of the phase shifts:

$$\mathrm{t}_l(k) = -\frac{e^{i\delta_l(k)}}{k} \sin\delta_l(k). \tag{3.37}$$

3.6 The Scattering Solutions of the Radial Wave Equation

An alternative radial wave function $Z_l(r,k)$ was introduced by Faulkner and Stocks [3.12], which has the free-space form

$$Z_l(r,k) = j_l(kr)\mathrm{t}_l^{-1} - ikh_l^+(kr), \quad (r \geq S). \tag{3.38}$$

Comparing equation (3.38) with (3.36) we can easily see that the two functions are related:

$$e^{i\delta_l(k)} R_l(r,k) = \mathrm{t}_l(k)\, Z_l(r,k). \tag{3.39}$$

It is important to understand the applicability of these solutions, and to illustrate their differences we can consider their behaviour when subject to a null scattering event.

3.6.1 Null Scattering Events

In the absence of a scattering potential we have no means to change the state of a freely propagating wave and $\delta_l(k) = 0$. With this condition the radial wave function (3.11) simply reduces to a spherical Bessel function, and we also find on examining (3.37) that $\mathrm{t}_l(k) = 0$.

It is interesting to see how the case $\mathrm{t}_l(k) = 0$ affects the scattered state $\Psi_k(\bar{r})$ when this is defined in terms of $R_l(r,k)$. Consistency

demands that the asymptotic form of the scattered state (3.33) should be related to its eigenfunction expansion (3.3) in the appropriate limit

$$\Psi_k(r) = \sum_L a_L(k) R_l(r) Y_L(\hat{r}),$$

and this allows the coefficients $a_L(k)$ to be determined. The analysis gives [3.13]:

$$\Psi_k(\vec{r}) = 4\pi \sum_L i^l e^{i\delta_l(k)} R_l(r,k) Y_L^*(\hat{k}) Y_L(r), \tag{3.40}$$

and substituting the condition $\delta_l(k) = 0$, we find that we reproduce Bauer's expansion for a plane wave in an angular momentum basis,

$$e^{i\vec{k}\cdot\vec{r}} = 4\pi \sum_L i^l j_l(kr) Y_L^*(\hat{k}) Y_L(\hat{r}). \tag{3.41}$$

Not surprisingly, we have found that a phase shift $\delta_l(k) = 0$ conditions the scattered state to be a pure incident wave; or equivalently, that $t_l(k)$ is responsible for generating the scattered *wave* in the scattered *state* .

The null scattering event for $Z_l(r,k)$ makes this function singular because it behaves as t_l^{-1}, and we can assert that the relationship between the two radial wave functions (3.39) no longer holds. Consequently, we recognise that the $Z_l(r,k)$are only usefully defined in the presence of a scattering potential, and that they fully warrant their designation as the 'scattering solutions' of the radial wave equation.

We shall now complete this chapter by reviewing multiple-scattering theory in the spirit of Gyorffy and Stott [3.14], which will lead to Faulkner and Stock's expression for the multiple scattering Green function [3.12].

3.7 The Scattering Path Operator

To effect the transition from single to multiple scattering theory, we consider a total potential $V(\vec{r})$ to be derived from an assembly of muffin-tin potentials $v^{i}(\vec{r})$ located at points $\vec{R}_i$;

$$V(\vec{r}) = \sum_i v^{i}(\vec{r} - \vec{R}_i). \tag{3.42}$$

For brevity, we shall assume that the spatial dependence is understood and neglect to write this further here.

Recalling the defining equation for the Green function G^+ (3.20), we can rewrite the scattering problem (3.28) for the potential V as the operator equation;

$$\left[-\left\{\nabla^2 + \varepsilon\right\} + V \right] G^+ = 1, \tag{3.43}$$

where 1 is again the identity operator. The expression in braces is the free-space Hamiltonian, which has the free-space Green function G_0^+. Taking advantage of this, we can write the operator equation

$$\left[-\left(G_0^+\right)^{-1} + V \right] G^+ = 1, \tag{3.44}$$

and thus obtain the full Green function G^+ as a perturbation about the free-space Green function G_0^+,

$$G^+ = G_0^+(1 - VG_0^+)^{-1}. \tag{3.45}$$

Expanding (3.44) (taking care over the non-commutativity of the operators) produces the perturbation series,

$$G^+ = G_0^+ + G_0^+VG_0^+ + G_0^+VG_0^+VG_0^+ + \ldots,$$

which can also be written more compactly as a Dyson equation:

$$G^+ = G_0^+ + G_0^+ V G^+ \qquad (3.46\text{ a})$$

$$= G_0^+ + G^+ V G_0^+ . \qquad (3.46\text{ b})$$

The Dyson equation (3.46) is formally solved through the total scattering operator T:

$$G^+ = G_0^+ + G_0^+ \mathrm{T}\, G_0^+ , \qquad (3.47)$$

where

$$\mathrm{T} = \mathrm{V} + \mathrm{V} G_0^+ \mathrm{T} \qquad (3.48\text{ a})$$

$$= \mathrm{V} + \mathrm{T}\, G_0^+ \mathrm{V}. \qquad (3.48\text{ b})$$

These relations are noteworthy since it is a simple task to reproduce the Lippmann-Schwinger equations (3.30) from (3.48).

We have now come to the crux of this analysis. Because we have not made any additional assumptions about the potential V in deriving the expressions above, the results (3.48) are completely general. Consequently, we can relate the single scattering operators t^i associated with the potentials v^i in a similar manner to relations (3. 48);

$$\mathrm{t}^i = v^i + v^i G_0^+ \mathrm{t}^i = (1 - G_0^+ v^i)^{-1} v^i \qquad (3.49\text{ a})$$

$$= v^i + \mathrm{t}^i G_0^+ v^i = v^i (1 - G_0^+ v^i)^{-1}. \qquad (3.49\text{ b})$$

We can also relate the total scattering operator T to a particular site potential v^i by a direct comparison of equation (3. 42) with (3. 48):

$$\mathrm{T} = \sum_i v^i + \sum_{i,n} v^i G_0^+ \mathrm{T}. \qquad (3.50)$$

What we are aiming to do is to express the total scattering T in terms of

individual scattering contributions from the potentials v^i. To achieve this, we introduce the partial scattering operator Q^i, such that:

$$\mathrm{T} = \sum_i Q^i. \tag{3.51}$$

The difference between the operators Q^i and t^i should be clear: Q^i denotes the scattering from site i in the presence of all other (multiple) scattering events within the assembly, whereas t^i denotes the (single) scattering solely from the potential v^i.

Hence, we can replace the T operator in equation (3. 49):

$$\sum_i Q^i = \sum_i v^i + \sum_{i,n} v^i G_0^+ \; Q^n, \tag{3.52}$$

which allows us to isolate the contribution from site i,

$$\begin{aligned} Q^i &= v^i + \sum_n v^i G_0^+ \; Q^n, \\ &= v^i + v^i G_0^+ Q^i + \sum_{n \neq i} v^i G_0^+ Q^i. \end{aligned} \tag{3.53}$$

This last expression may be reduced further by using the single scattering t^i relations (3.47);

$$Q^i = \underbrace{\mathrm{t}^i}_{Direct} + \underbrace{\sum_{n \neq i} \mathrm{t}^i G_0^+ Q^i}_{Assembly}, \tag{3.54}$$

and we appear to have achieved our objective; equation (3.53) relates the contribution to the total scattering from the potential v^i as the sum of all scattering events within the assembly that contribute an incident wave to this site, plus the scattering from the direct wave incident to this site.

Gyorffy and Stott [3.14] further decomposed the partial scattering

operator Q^i to represent the elastically scattered elements of the total scattering operator T, by introducing the scattering path operator τ^{ij} where:

$$Q^i = \sum_j \tau^{ij}, \tag{3.55}$$

and thus,

$$\mathrm{T} = \sum_i Q^i = \sum_{i,j} \tau^{ij}. \tag{3.56}$$

By considering equations (3.54) and (3.55), the scattering path operator can be related to the single scattering operators;

$$\begin{aligned} \tau^{ij} &= \mathrm{t}^i \delta_{i,j} + \mathrm{t}^i G_0^+ \sum_{p \neq i} \tau^{pj} \\ &= \mathrm{t}^i \delta_{i,j} + \sum_{p \neq j} \mathrm{t}^j G_0^+ \tau^{ip}, \end{aligned} \tag{3.57}$$

where $\delta_{i,j}$ is the Kronecker delta function.

3.8 Calculating the τ Matrix

If we project the defining equation for the scattering path operator (3.57) into the position representation, and adjust the origin of the coordinate system to locate the scattering sites, we obtain;

$$\begin{aligned} \tau^{ij}(\vec{r}+\vec{R}_i, \vec{r}'+\vec{R}_j) &= \mathrm{t}^i(\vec{r}+\vec{R}_i, \vec{r}'+\vec{R}_j)\delta_{i,j} \\ &+ \sum_{n \neq i} \int_0^{S_1} d\vec{r}_1 \int_0^{S_2} d\vec{r}_2 \Big[\mathrm{t}^i(\vec{r}+\vec{R}_i, \vec{r}_1+\vec{R}_i) \\ &\times G_0^+(\vec{r}_1+\vec{R}_i, \vec{r}_2+\vec{R}_n) \tau^{ij}(\vec{r}_2+\vec{R}_n, \vec{r}'+\vec{R}_j) \Big]. \end{aligned} \tag{3.58}$$

The limits on the integrals arise from the muffin-tin character of the potential; since $v^i(\vec{r}) = 0$ outside the boundary of the muffin-tin sphere we can assert, after examining (3. 49) and (3. 57), that both t^i and τ^{ij} have zero value unless $\vec{r}_1$ lies within site i and $\vec{r}_2$ lies within site j, and hence that $\vec{r}_1, \vec{r}_2$ are constrained to lie within the boundaries of the muffin-tin spheres S_1, S_2 respectively.

The spatial restrictions introduced by this geometry allow a convenient expansion of the free-space Green function G_0^+, which simplifies equation (3.57) considerably.

By examining G_0^+ in the position representation (3.32), we find it is permissible to write

$$G_0^+(\vec{r}_1+\vec{R}_i,\vec{r}_2+\vec{R}_n) = G_0^+(\vec{r}_1,\vec{r}_2-\vec{R}_{in}), \tag{3. 59}$$

where $\vec{R}_{in} \equiv \vec{R}_i - \vec{R}_n$; and substituting the RHS of (3.59) into the angular momentum decomposition of G_0^+ (3.34) produces:

$$G_0^+(\vec{r}_1+\vec{R}_i,\vec{r}_2+\vec{R}_n) = -ik\sum_L j_l(\vec{r}_1)Y_L^*(\hat{r}_1)h_l^+(\vec{\Re})Y_L(\hat{\Re}). \tag{3. 60}$$

where $\vec{\Re} = \vec{r}_2 - \vec{R}_{in}$.

We can now make use of a beautiful relationship that expands a spherical Hankel function on one site, in terms of a spherical Bessel function centred on a different site;

$$-ik\,h_l^+(\vec{\Re})Y_L(\hat{\Re}) = \sum_{L'} g_{LL'}^{ij} j_{l'}(r_2)Y_{L'}(\hat{r}_2). \tag{3. 61}$$

We note that this expansion is only valid if $|\vec{r}_2| < |\vec{R}_{in}|$, which is

certainly true for the integrals above (3.57). The $g^{ij}_{LL'}$ in equation (3.61) are the real-space structure constants:

$$g^{ij}_{LL'} = -4\pi ik(-1)^{m_i(l'-l)} \sum_{L} i^{-l_1} C(\bar{L}, L, L_1) h^{+}_{L_1}(r_{nm}) Y_{L_1}(\hat{r}_{nm}), \qquad (3.62)$$

with the Gaunt factors $C(\bar{L}, L', L_1)$ defined as

$$C(\bar{L}, L', L_1) \equiv \int d\hat{r}\, Y^{*}_{L}(\hat{r}) Y_{L'}(\hat{r}) Y_{L_1}(\hat{r}). \qquad (3.63)$$

By using the expansion (3.61) to define the Green function (3.60) we have effectively given it a local basis;

$$G^{+}_{0}(\vec{r}_1 + \vec{R}_i, \vec{r}_2 + \vec{R}_n) = \sum_{L,L'} j_l(\vec{r}_1) Y^{*}_{L}(\hat{r}_1)\, g^{ij}_{L,L'}\, j_{l'}(r_2) Y_{L'}(\hat{r}_2). \qquad (3.64)$$

If we now substitute this local basis Green function (3.64) into the real-space τ matrix equation (3.58), recognise the angular momentum representation for the 'on the energy shell' τ matrix elements;

$$\tau^{ij}_{L,L'} = \int d\vec{r} \int d\vec{r}'\, j_l(\vec{r}) Y_L(\hat{r}_i) \tau^{ij}_{L,L'}(\vec{r} + \vec{R}_i, \vec{r}' + \vec{R}_j) j_l(\vec{r}') Y^{*}_{L'}(\hat{r}'), \qquad (3.65)$$

and also recall the analogous matrix elements for the t matrix (3.33), we produce;

$$\tau^{ij}_{LL'} = t^{i}_{LL'} \delta_{ij} + \sum_{n \neq i} t^{i}_{LL'}\, g^{in}_{L_1 L_2}\, \tau^{nj}_{L_2 L'}, \qquad (3.66)$$

which is the fundamental equation of multiple scattering theory.

It is easier to understand the structure of (3.66) as a matrix equation [3.15]; if we define $\tau^{ij}_{LL'} = \underline{\tau}$, $t^{i}_{LL'}\delta_{ij} = \underline{t}$ and let $(1 - \delta_{ij}) g^{in}_{L_1 L_2} = \underline{\Gamma}$, where 1 is the unit matrix, then (3. 66) becomes:

$$\underline{\tau} = \underline{t} + \underline{t}\,\underline{\Gamma}\,\underline{\tau} \tag{3.67 a}$$

$$= \left[\underline{t}^{-1} - \underline{\Gamma}\right]^{-1}. \tag{3.67 b}$$

We can now see explicitly how both local ($\underline{t}$) and global ($\underline{\Gamma}$) quantities contribute separately to the τ matrix.

3.9 The Multiple Scattering Green Function

Faulkner and Stocks [3.12] derived the multiple scattering Green function by substituting $T = \sum \tau^{ij}$ into the Dyson equation (3.47) and projecting the resulting equation into a real-space representation. By considering the site dependent geometry as two separate cases, they produced:

$$\begin{aligned} G^{+}(\vec{r},\vec{r}';\varepsilon) = \sum_{i,j,L,L'} \Big[& Z_L^i(\vec{r};\varepsilon)\tau(\vec{r},\vec{r}';\varepsilon)Z_{L'}^j(\vec{r}';\varepsilon)Y_L^*(\hat{r})Y_{L'}(\hat{r}') \\ & - Z_L^i(\vec{r}_<;\varepsilon)j_l^i(\vec{r}_>;\varepsilon)Y_L^*(\hat{r}_<)Y_{L'}(\hat{r}_>)\delta_{L,L'}\delta_{i,j}\Big], \end{aligned} \tag{3.68}$$

where Z_L^i, j_l^i are the regular and irregular scattering solutions for the ith potential. The Green function (3.68) thus describes the scattering (per angular momentum channel) between two separated sites i,j when $\vec{r},\vec{r}'$ fall within these sites, and describes the scattering at a single site when $\vec{r},\vec{r}'$ both fall within the same site. Since the irregular scattering solution is only included for the single site case, it can sensibly be interpreted as a "self-energy" term.

The Green function (3.68) has two properties which make it useful for the systems studied later in this thesis; it allows differing potentials derived from different atomic systems to be used, and it produces real values with real energies.

We shall show how the Green function (3. 68) can be modified to model spectroscopic phenomena in the next chapter, when we discuss the real-space photocurrent equation.

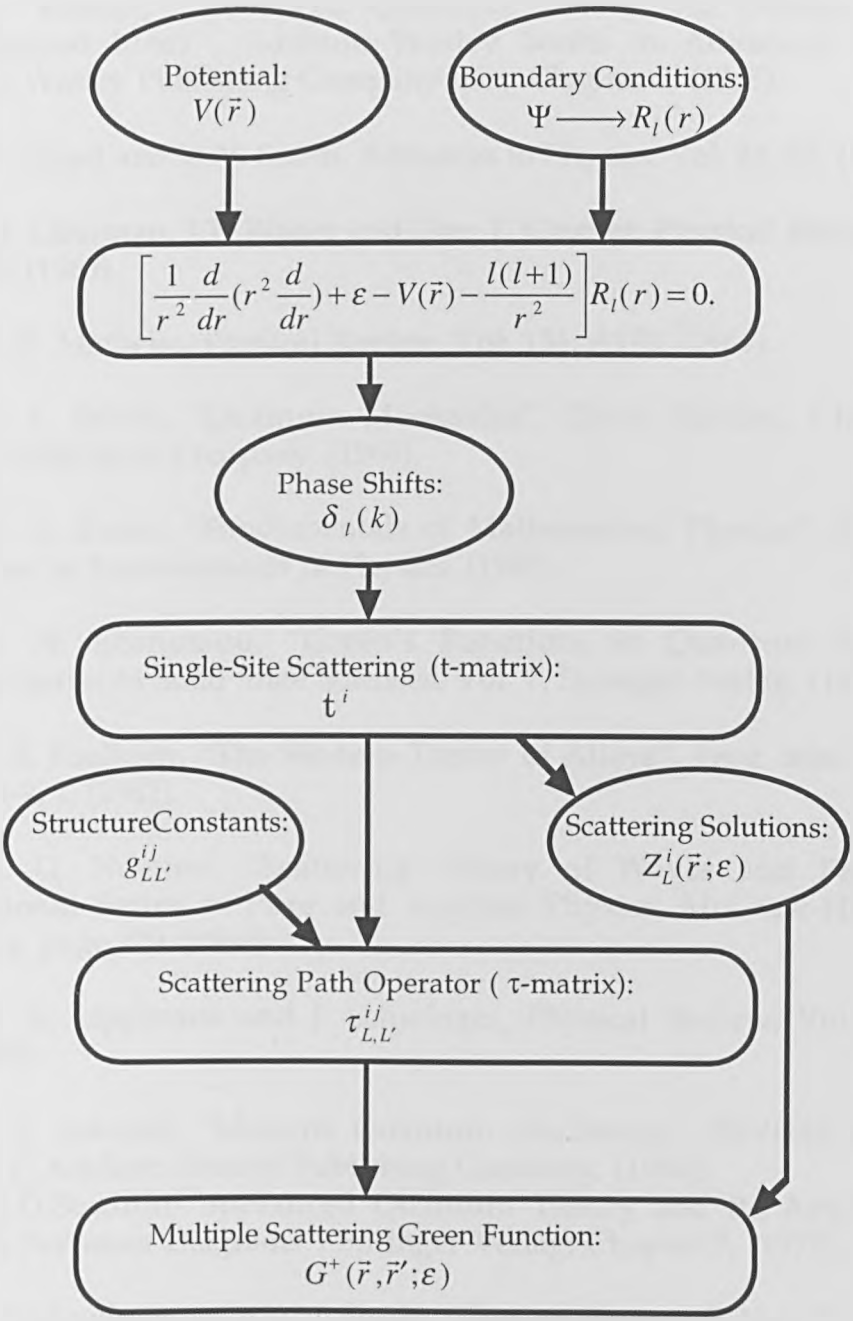

Figure 3.b: a flow diagram illustrating the development of the key concepts of multiple scattering theory and how these may be used to calculate the Green function.

3.10 References

[3.1] P. Roman, "Advanced Quantum Theory, An Outline of the Fundamental Ideas", Addison Wesley Series in Advanced Physics, Addison Wesley Publishing Company Inc., Chapter 3, (1965).

[3.2] P. Lloyd and P. V. Smith, Advances in Physics, Vol. 21, 69, (1972).

[3.3] D. Liberman, J.T. Waber and Don T. Cromer, Physical Review, Vol. 137, A27, (1965).

[3.4] L. F. Matheiss, Physical Review, Vol. 134, A970, (1964).

[3.5] L. I. Schiff, "Quantum Mechanics", Third Edition, Chapter 4, McGraw-Hill Book Company, (1968).

[3.6] E. A. Kraut, "Fundamentals of Mathematical Physics", McGraw-Hill Series in Fundamentals of Physics, (1967).

[3.7] E. N. Economou, "Green's Functions in Quantum Physics", Springer Series in Solid State Sciences, Vol. 7, Springer-Verlag, (1979).

[3.8] J. S. Faulkner, "The Modern Theory of Alloys", Prog. Mat. Sci.,Vol 27, No. 1-2, 1, (1982).

[3.9] R. G. Newton, "Scattering Theory of Waves and Particles", International Series in Pure and Applied Physics, McGraw-Hill Book Company, page 179, (1966).

[3.10] B. A. Lippmann and J. Schwinger, Physical Review, Volume 79, 469, (1950).

[3.11] J. J. Sakurai, "Modern Quantum Mechanics", Revised Edition, Chapter 7, Addison-Wesley Publishing Company, (1994);
M.D.Scadron "Advanced Quantum Theory and Its Applications Through Feynman Diagrams", Springer-Verlag, Chapter 7, (1979).

[3.12] J. S. Faulkner and G. M. Stocks, Physical Review B, Vol. 21, 8, 3222-3244, (1980).

[3.13] See, for instance, P. Roman, "Advanced Quantum Theory", *(ibid)*, pages 159-165.

[3.14] B. L. Gyorffy and M. J. Stott in "Band Structure Spectroscopy of Metals and Alloys", D. J. Fabian and L. M. Watson, (ed.s), Academic Press, (1973).

[3.15] P. J. Durham, "Multiple Scattering Theory Basic Working Notes", (private communication).

[3.16] A. Messiah, "Quantum Mechanics", Volume 1, North Holland Publishing Company, Chapter 5, (1961).

Chapter Four

Photoemission Spectroscopy

This chapter discusses the experimental technique of angle-resolved ultra-violet photoemission spectroscopy (ARUPS), and begins with an account of the methods used to obtain photoemission spectra. The phenomenology of photoemission is presented and the use of Cooper minima to monitor the growth of rare-earth thin films is discussed. The chapter concludes with a model description of the photocurrent derived from multiple scattering theory. Rydberg units are used throughout, where $\hbar^2 = 2m = e = 1$.

4.1 Introduction

In 1887, Hertz [4.1] was investigating the behaviour of sparks and made a seemingly innocuous discovery that was to have a profound impact on physics; the distance that a spark in an arc lamp could jump was increased in the presence of a second, nearby, spark.

Subsequent investigations by Hertz, Lenard and Thomson determined that UV light was responsible for liberating electrons from metals, thereby generating electrical currents that emanated from a metal whenever the light exceeded a particular frequency.

This phenomenon, the photoelectric effect, confounded all

attempted explanations until 1905, when Einstein suggested a radically new interpretation that fully utilised Planck's quantum of action; he proposed that the maximum kinetic energy of an electron ε_{max} be related to the difference in energy between a quantum of light $\hbar\omega$ and a characteristic work function Φ that signifies a threshold for the onset of photoemission. Einstein's equation for the photoelectric effect,

$$\varepsilon_{max} = \hbar\omega - \Phi, \qquad (4.1)$$

provides the fundamental basis for photoemission spectroscopy, arguably the most powerful experimental technique for determining the electronic structure of a wide class of materials.

For reasons of clarity, some notes on terminology are warranted. It is convenient to make a distinction between the photoemission spectra that are determined by experiment, and the photocurrents that arise from idealised theoretical models. The photocurrents are assumed to derive from the motion of photoelectrons, where a photoelectron is an electron that has been raised from its groundstate by a single photon. The energy which the photoelectron must exceed in order to contribute to the photocurrent is called the vacuum level - since final states beneath the vacuum level are bound states, whereas final states above the vacuum level have kinetic energy. However, a more convenient reference energy for photoemission spectra is the Fermi level, and the energy difference between the Fermi level and the vacuum level is defined to be the workfunction.

Einstein's equation (4.1) supplies an obvious and naïve interpretation for photoemission spectra (see figure 4.a, overleaf). By illuminating a material with light of a sufficiently high frequency and discriminating the energy of the photoelectrons, the photoemission

analyse electron energies [4.3], the predominant method for PES employs an electrostatic field to deflect the photoelectrons into a charge detector such as a channeltron (see figure 4.b).

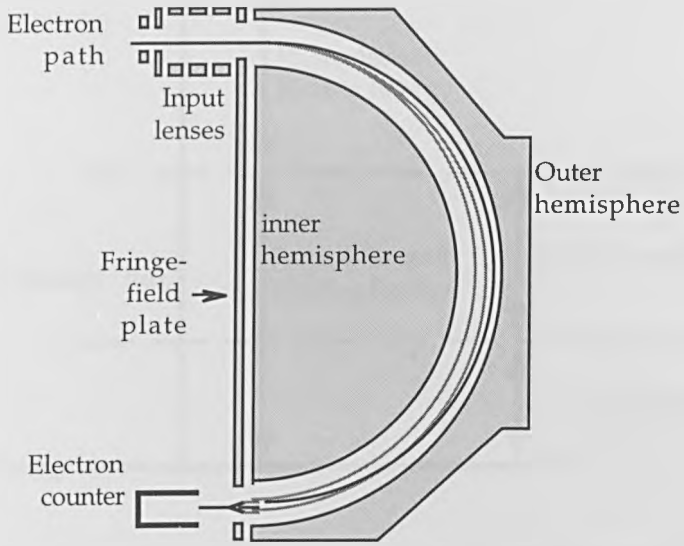

Figure 4.b: the cross-section of a typical hemispherical analyser.

The analyser energy resolution is geometry dependent; for a given energy it is effectively determined by the ratio of the total path length in the analyser to the width of the entrance aperture.

The traditional laboratory UPS light sources are the spectral lines of the noble gases, obtained from gas discharge lamps. The discharge lamps can produce a somewhat restricted range of photon energies by ionising different high purity noble gases: HeII radiation gives an upper limit of 40.8 eV, while ArI gives a lower limit of 11.8 eV. Although gas discharge lamps are certainly effective light sources for photoemission experiments, the full experimental potential of PES is only realised through the use of synchrotron radiation since this provides a more "tunable" light source.

Synchrotron radiation is the light emitted by accelerating relativistic electrons, producing a continuum of photon energies with a

spectra are assumed to furnish a proportional sampling of the occupied electronic states. It is the purpose of the remainder of this chapter to detail the limitations of this naïve interpretation.

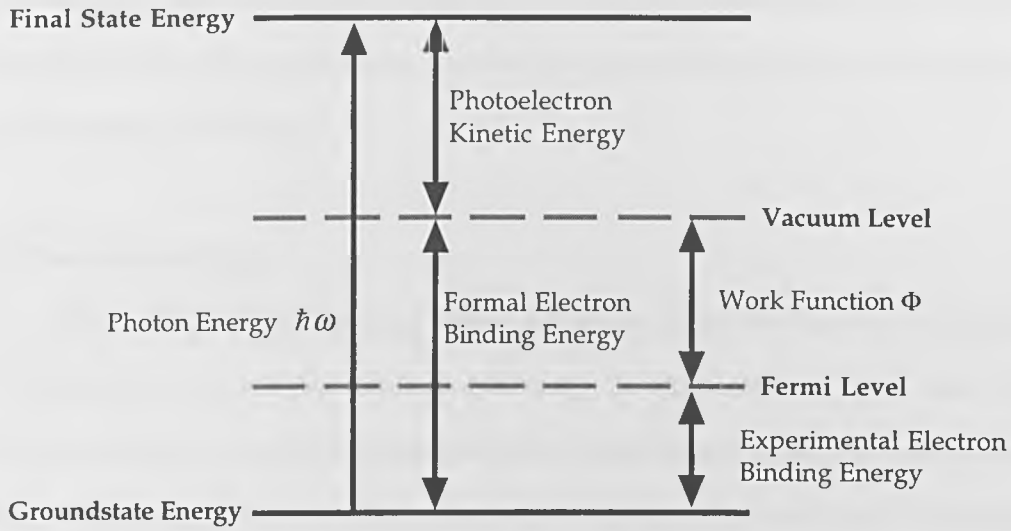

Figure 4.a: showing the energy balance relations in photoemission.

4.2 Experimental Aspects of Photoemission Spectroscopy

The evolution of the photoelectric effect into the experimental technique of ARUPS had to wait until the 1960's for advances in UHV technology, and the development of electron analysers with a sufficiently high sensitivity and resolution.

In the UHV regime (~ 10^{-10} mbar) the residual gas molecules in a vacuum chamber have a mean free path length of the order of kilometres. The rate of surface contamination by the residual UHV atmosphere is reduced to a level that allows an "atomically clean" surface to remain clean throughout the lifetime of a photoemission experiment. For rare-earth metals, this lifetime is typically less than 45 minutes. UHV is achieved by a variety of pumping methods that are best described elsewhere [4.2].

Although a number of different physical techniques can be used to

high beam intensity and strong polarisation [4.4]. The experimental data for ultrathin films of yttrium presented in the final chapter of this thesis was taken at the Daresbury Synchrotron Radiation Source. This operates a 15 m storage ring at a beam energy of 2 GeV; the typical ring current is 200 mA and in normal operation (multi-bunch mode) this has a lifetime of approximately 24 hours.

4.3 Phenomenology

We have, so far, defined photoemission as an excitation process for an electron in which the energy exchange is mediated by a photon. We can note some important consequences immediately from this definition; firstly, photoemission is dependent on both the cross-section for photon capture and on the availability of a suitable final state at higher energy, and secondly, by removing an electron from a correlated N electron system, a hole state will be created which will induce a response amongst the remaining (N-1) electrons. Leaving aside the issue of cross section until later, we shall discuss the other points raised in turn.

4.3.1 The Photoelectron

A freely propagating non-relativistic electron satisfies the dispersion relation

$$\varepsilon = k^2 + C, \tag{4.2}$$

where ε is the electron's kinetic energy, k is the propagation vector for the electron (see section 2.4), and C is a constant potential which we can choose to be zero without loss of generality.

The dispersion relation (4.2) constrains the possibilities for an electron-photon interaction; it specifies that an electron which changes its

energy to a value ε' must also change its k-quantum number to a new value k' through a quadratic relationship. Since the photon has a propagation vector that depends linearly on energy [4.5], it cannot satisfy relation (4.2) for arbitrary energy and we can deduce that a free electron cannot gain or lose a UV photon, simply because there are no final states available for these processes.

In the spatially periodic potential of a crystal, however, the electron's momentum is expressed through its Bloch wave vector $\vec{k}$, which is not unique but is defined modulo a reciprocal lattice vector $\vec{G}$. We can therefore write

$$\vec{k}' = \vec{k} \pm \vec{G}, \tag{4.3}$$

and classify photoemission from a crystal as an Umklapp process, since the electron diffracts against the crystal lattice in order to acquire the change in $\vec{k}$.

This argument demonstrates why UPS is such a useful probe of single crystal electronic structure. A photoelectron is created when a photon excites a groundstate electron into a final state which does not permit further interactions with the photon field; the photoelectron achieves this state by satisfying the underlying dispersion relation for the crystal band structure, and this information is preserved in its transport to the detector. Thus, from these considerations, UPS elicits the electronic structure of crystals because it promotes k–conserving (direct) transitions.

In principle, the direct transition suggests that we can image the Brillouin zone through angle-resolving experiments, by relating the kinetic energy of the photoelectron to its trajectory (see figure 4.c). In practice, however, the reduced symmetry of the surface can only conserve

momentum within the surface reciprocal net, and the normal component of momentum $\vec{k}_{\perp}$ becomes uncertain. This loss of information prevents specific points in the Brillouin zone from being resolved, and the initial electron state lies somewhere along a "rod" in k space. Pendry has estimated [4.6] that the uncertainty in the normal component is 'smeared' over approximately one quarter of the Brillouin zone, but for rare-earth metals this is likely to be greater.

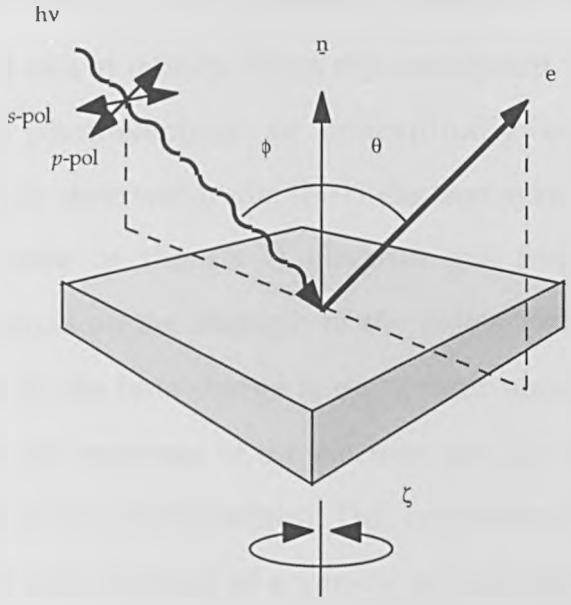

Figure 4.c: the experimental parameters for ARUPS, used in bandmapping. A photon arrives at angle ϕ and an electron is emitted at angle θ to the surface normal n. The sample azimuth is denoted by angle ζ and *p*-pol is the polarisation vector oriented to *plough* the surface. If we resolve the photoelectron momentum $\vec{k}$ into components, $\vec{k} = \vec{k}_{\perp} + \vec{k}_{||}$, where $\vec{k}_{\perp}$ and $\vec{k}_{||}$ are the normal and parallel components of momentum relative to the crystal surface, we can establish a relationship between the momentum, the kinetic energy ε_{kin} and the angle of emission:

$$\vec{k}_{\perp} = \sqrt{\varepsilon_{kin}}\cos\theta, \quad \vec{k}_{||} = \sqrt{\varepsilon_{kin}}\sin\theta.$$

These equations are used to establish the experimental band structure.

If the only physical processes at work in UPS were direct transitions modified by some degree of uncertainty, we would expect the spectra to comprise a set of Lorentzian functions corresponding to the single

electron states of the band structure. The fact that experimental UPS spectra show more structure than just broadening can be attributed to phenomena which lie beyond the single electron model.

4.3.2 The Hole State

The binding energy of a photoelectron is defined rigorously to be the minimum energy needed to remove a single electron from an N electron system to the vacuum level; it is, therefore, the difference in energy between the N and the (N-1) electron systems when the photoelectron is at rest at infinity. From this standpoint, we can regard the removal of the photoelectron as conceptually equivalent to the appearance of a hole state within the (N-1) electron system.

The hole state in the (N-1) electron gas induces a screening response that depends on the strength of the hole's 'positive charge', and since the strength of the hole charge is dependent upon the proximity of the photoelectron, the response of the electron gas can be correlated with the kinetic energy of the photoelectron. This correlation establishes a time scale for the onset and duration of a variety of response phenomena that are manifested in the line shapes and fine structure of spectral features. Figure 4.c presents a brief summary of these phenomena.

The influence of the hole state on the electron gas can also be categorised, in the language of Hartree-Fock theory, by its impact on the effective potential $v_{eff}(\vec{r})$. If the sudden appearance of a hole state disturbs the configuration of the (N-1) electrons sufficiently, then $v_{eff}(\vec{r})$ is notably altered and the (N-1) electrons are forced to adopt the eigenstates of a different Hamiltonian to the N electron system. This reduces the photoelectron's binding energy by an amount equal to the difference in total energies of the N and (N-1) electron gases, the aptly named

relaxation energy.

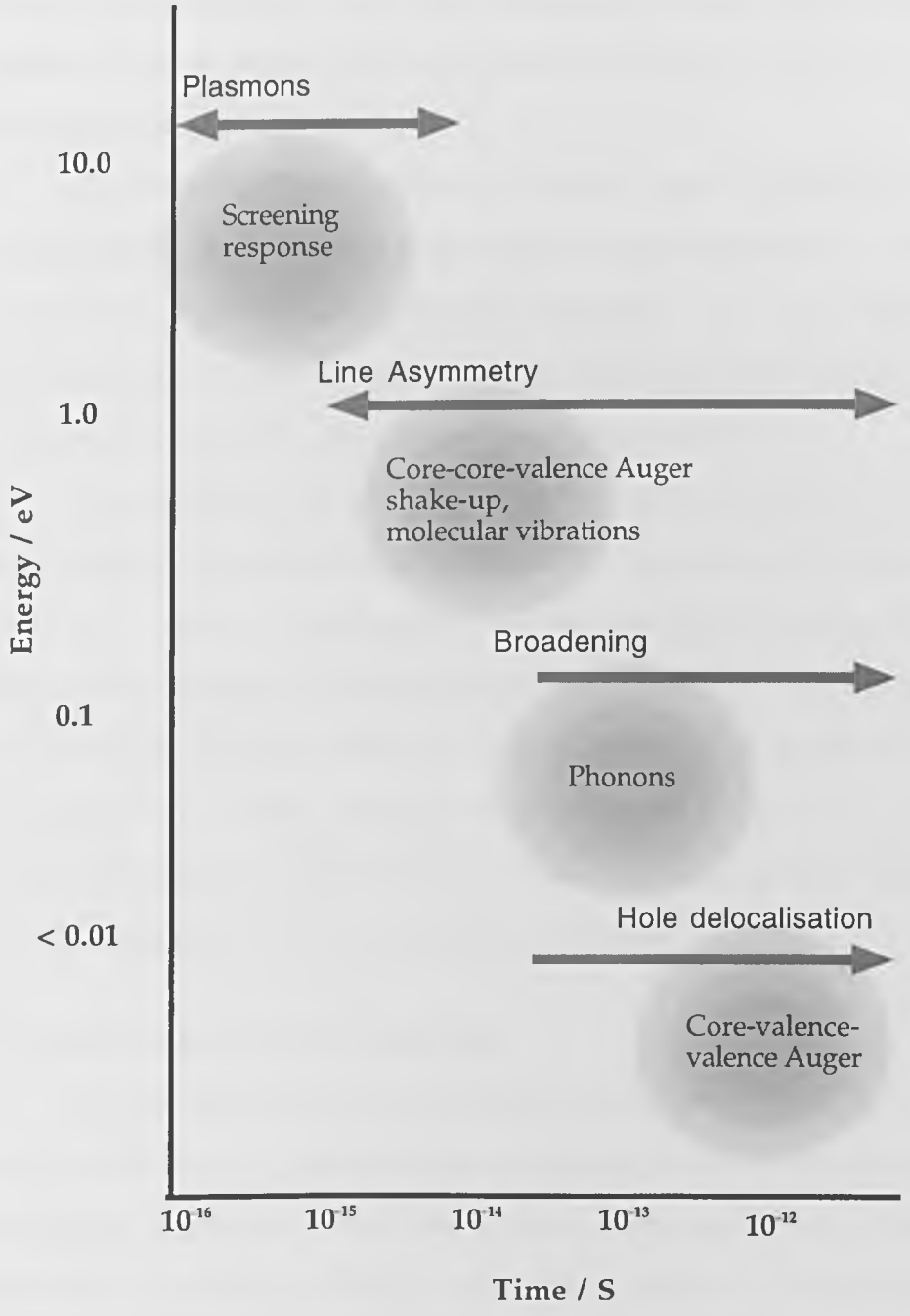

Figure 4.d: showing characteristic time scales and energies for the formation of spectral features, and their underlying phenomena. Adapted from Gadzuk [4.7].

By contrast, when $v_{eff}(\vec{r})$ is not disturbed too greatly, we anticipate that the binding energy is adequately approximated by the single electron orbital energy and we can invoke Koopmans' theorem [4.8]. It is in this instance that we expect the single electron theory to provide a suitable description of spectral features.

In general [4.9], Koopmans' theorem may be applied when the bandwidth of the state that originates the photoelectron is of the same order as the intra-atomic electrostatic repulsion: $\Delta\varepsilon \sim U$. Consequently, we would not expect the narrow bands associated with f electrons to be completely described within the single electron model.

The discussion above illustrates the main difficulty in the naïve interpretation of photoemission spectra. The presence of a hole state can lead to a notable modification of the electronic structure, with a concomitant change in the measured energy of the photoelectron. For UPS, the hole state lies within the valence band and is therefore extended throughout the crystal, whilst at higher photon energies the hole state remains localised to the ion core. Thus, photoemission measures the excited states of a crystal and not the groundstate properties.

4.3.3 The Electron-Photon Interaction

We can consider the introduction of a radiation field into a crystal as a perturbation, Λ, which acts on the existing electronic states. It is, with hindsight, somewhat ironic that a fully quantised photon field is not necessary to model Λ [4.10]; a classical description parametrised by a vector potential $\vec{A}$ serves just as well, and this is the approach that we shall adopt in what follows.

The exact physical processes initiated within the crystal in response to an applied radiation field are not trivial; on a microphysical scale, we

expect $\vec{A}$ to be modified through its interactions with the local atomic fields. Furthermore, because the atomic fields at surfaces and interfaces will be different from those in the bulk of the crystal, we also expect a different optical response from these regions.

Fortunately, for UPS, we do not need to consider processes at quite this level of detail; in the UV range of energies a single wavelength can encompass around 100 atoms, and we can regard $\vec{A}$ as a slowly varying plane wave in the crystal. Hence, the incident radiation experiences the crystal surface (and possibly other interfaces) as a sharp boundary and transmission, reflection and refraction of the wave occurs. The optical response of the crystal in this approximation is therefore governed by its dielectric properties.

The dielectric function $\xi(\omega)$ for a crystal is a complex function, exhibiting a high degree of structure, which represents the elementary modes of excitation of an electron gas as a macroscopic average. The magnitude of the imaginary part of this function, $\mathcal{I}m\{\xi(\omega)\}$, is an important quantity because it gives a measure of the strength of energy loss processes. However, it is usually the case with transition metals that $\mathcal{I}m\{\xi(\omega)\}$ plateaus beyond 10 eV with little change in structure at higher energies. Whilst this suggests that UV radiation will be attenuated in the crystal, the attenuation as a function of path length is much less for $\vec{A}$ than it is for the electron scattering and direct transitions will still occur. This has a useful consequence; we do not expect to find a strong contribution from secondary electrons with UV radiation above this 10 eV threshold.

4.3.4 The Dipole Operator

The standard development for analysing the motion of an electron in a constant electromagnetic field [4.11] employs a replacement of the momentum and potential terms in the Hamiltonian, which we can write using Rydberg units as

$$\vec{P} \rightarrow \left(\vec{P} - \frac{\vec{A}}{c} \right), \; V \rightarrow \phi . \tag{4.4}$$

Here, ϕ is the scalar potential of the radiation field, c is the velocity of light, $\vec{P}$ is the electron's momentum and $\vec{A} = A_0 \hat{e}$ is the vector potential, with $\hat{e}$ a unit polarisation vector. We can thus write the Hamiltonian for electron states in the presence of radiation as

$$H = H_0 - \frac{1}{c}\left(\vec{P}.\vec{A} + \vec{A}.\vec{P} \right) + \frac{A^2}{c^2} + \phi, \tag{4.5}$$

where H_0 is the kinetic energy operator. This may be further simplified. We can neglect the quadratic term in (4.5) because $\vec{A}$ is small in comparison to $\vec{P}$, and since $\vec{A}$ is also defined as being transverse, we can choose to express (4.5) in the Coulomb gauge and set $\phi = 0$. Hence, we are left with the dipole operator,

$$\Lambda = \frac{1}{c}\left(\vec{P}.\vec{A} + \vec{A}.\vec{P} \right), \tag{4.6}$$

which can be written in a number of different forms that are more useful for the purposes of calculation [4.12], but (4.6) shows explicitly that the dipole operator is dependent on the polarisation of the vector potential, $\hat{e}$. The importance of this polarisation on the structure of photoemission spectra can be examined through a symmetry argument.

4.3.5 Polarisation Effects and Parity

The reflection symmetry properties of the dipole operator are expressed in terms of a mirror plane containing both the photoelectron and the detector. If the polarisation vector $\hat{e}$ lies within this mirror plane, the dipole operator has even reflection symmetry. If, however, $\hat{e}$ is normal to this mirror plane, the image of $\hat{e}$ will have opposite sign and the dipole operator is assigned an odd reflection symmetry.

In order to detect a photoelectron, the matrix element for the excitation process $\langle f|\Lambda|i\rangle$ at the detector must be non-zero. This will be achieved when the integrand of the matrix element is an even function of its spatial coordinates, because an odd integrand will integrate to zero over all space. Since the final state wave function is a plane wave which has even parity, we can establish a symmetry selection rule for photoemission: $\Lambda|i\rangle$ must also have an even symmetry to contribute to the photocurrent. Thus, with a suitably oriented polarised light source, it is possible to identify the parity of specific states in photoemission spectra.

The last issue which must be considered is the cross-section for the photoexcitation process, since this plays an essential part in the method used to grow reproducible ultrathin films.

4.3.6 Photoionisation and Cooper Minima

The probability that a photon will excite an electron can be expressed in the language of scattering theory; it is the cross-section for photoionisation, and as such, it has a value which is derived from the wavefunction for the initial electron state. This has an important consequence for the structure of photoemission spectra, because an atomic sub-shell wave function which possesses a node at a given energy will have no available cross-section for photoionisation at that energy.

The mechanism was first noticed by Cooper [4.13], and a suppressed emission of this type through an interval of the energy spectrum is named a Cooper minimum.

4.4 Cooper Minima and the Growth of Ultrathin Films

It is fortuitous that W has a Cooper minimum in the 5d band over an energy range 150-250 eV [4.14], since this corresponds to both an enhanced cross-section for emission from the Y 3d band and to the giant 4f resonance in the lanthanides [4.15] (see figure 4.e, overleaf). Consequently, by tuning a SR light source to exploit these cross-sections effects, the growth of a rare-earth single crystal on W(110) may be monitored through the attenuation of a suitable W photoemission signal with time, leading to reproducible and well-characterised thin film single crystals [4.16]. Figure 4.f, overleaf, shows the degree to which the W(110) photoemission signal is effectively 'switched-off', whilst the signal from a Gd overlayer is boosted with a photon energy of ~150 eV.

The most convenient substrate features to monitor during growth are the W 4f core-levels, which are split into bulk and surface components on a clean surface. Since the magnitude of this surface core level shift (SCLS) is typically 300-320 meV the two components are easily resolved. The adsorbate coverage may be estimated by assuming that the decay in the bulk 4f peak intensity is exponential and correlated with a constant rate of epitaxial deposition [4.17]. These coverage estimates are, at best, provisional. One way for the assumptions to breakdown occurs through photoelectron diffraction, which may enhance the intensity of spectral features with increasing adsorbate coverages by forward-focussed scattering. However, the enhancement is only expected to be appreciable with photoelectron energies in excess of 200 eV [4.18], and it is not

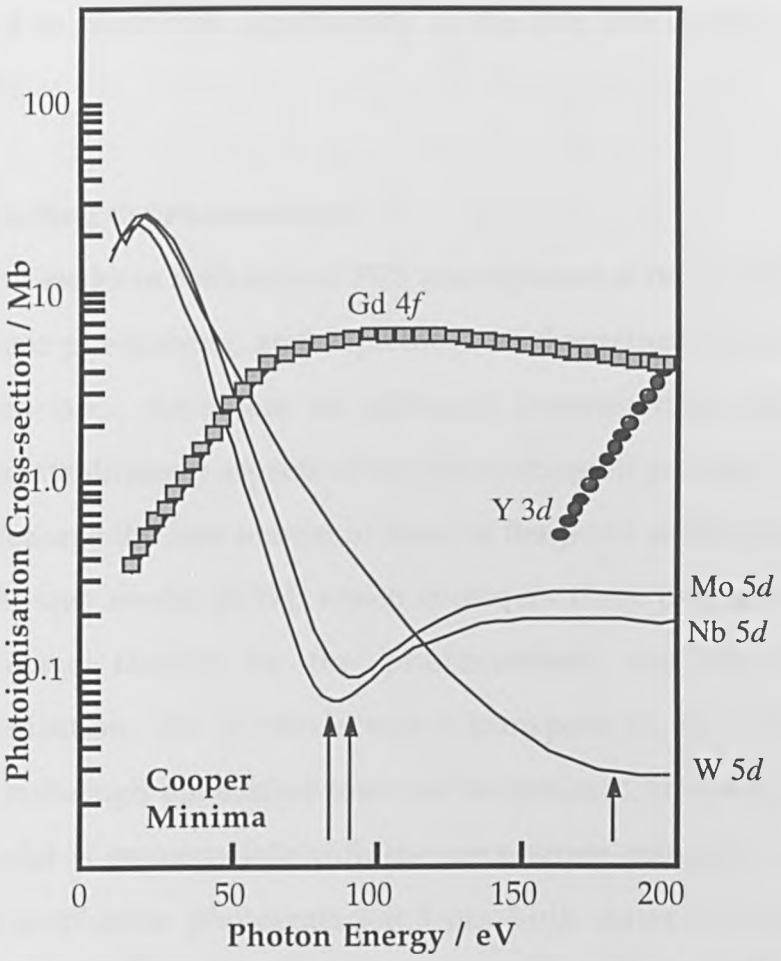

Figure 4.e, showing the enhanced photoionisation cross-sections for Gd and Y that coincide with the 5d Cooper minima of the refractory metals W, Nb,Mo. Adapted from Yeh & Lindau [4.14]

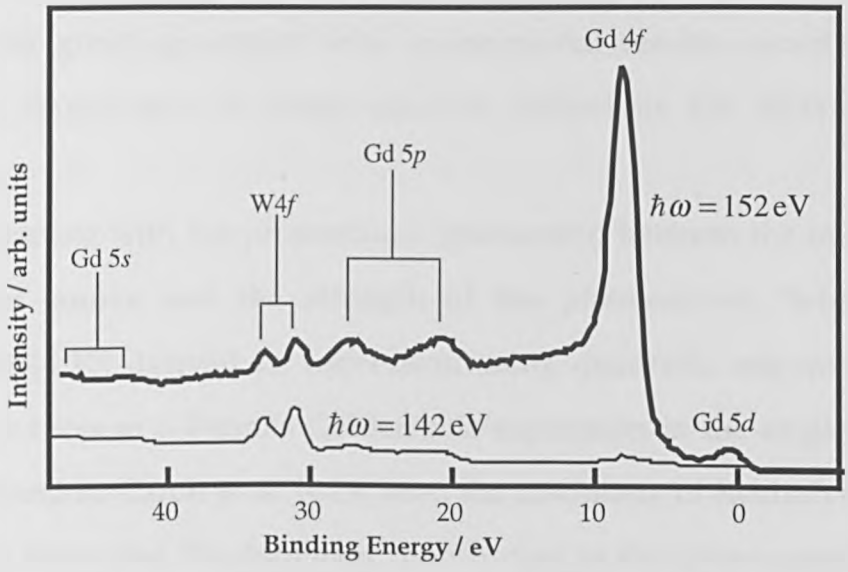

Figure 4.f, PES spectra of 3 ML of Gd on W(110) showing the effects of the giant 4d resonance at $\hbar\omega = 152$ eV.

expected to contribute significantly to the thin film spectra presented in chapter 5.

4.5 Modelling the Photocurrent

As we have seen above, PES encompasses a rich variety of energy-dependent phenomena, and a plethora of theoretical models have been proposed over the years as different investigators have chosen to approximate different aspects of the photoemission process.

Perhaps the best known of these is Berglund and Spicer's variant of the three-step model [4.19], which considers three processes as separate contributive factors to the photocurrent: the cross-section for photoionisation, the photoelectron's transport to the surface and its transport through the surface towards the detector. The fact that the three-step model is incompatible with the uncertainty principle and is known to over-emphasise photoemission from bulk states has not, however, detracted from its popularity with experimentalists [4.1]. Fortunately, a more exacting analysis based on scattering theory has produced a consensus on the salient aspects of photoemission theory and, by providing good agreement with experimental results, established the relative importance of single electron behaviour for measured PES spectra.

Starting with the proportional relationship between the intensity of the light source and the strength of the photocurrent, Schaich and Ashcroft [4.20] derived an expression using quadratic response theory, which reduces to a Fermi's Golden-rule expression in the single-electron approximation. Caroli et al [4.21] used the machinery of Keldysh diagrams [4.22] to show that the dominant contribution to the photocurrent can be expressed within the single-electron theory. However, by embracing

single-electron theory from the outset, it was Adawi [4.23] who first produced what is arguably the most useful calculative scheme in the family of photoemission theories, by recognising the formal symmetry between PES and Low Energy Electron Diffraction (LEED).

We can understand the LEED/PES symmetry intuitively. The LEED electron is initially prepared as a plane wave and scatters from a crystal surface into directed beams. The k-dependent surface structure is, therefore, encoded in the LEED electron's final state. The photoelectron, however, has a k-dependent initial state and arrives at the detector as a final-state plane wave. The two processes thus mirror each other in their initial and final states, and are mathematically equivalent descriptions when the photoelectron's initial and final states are reversed.

Although this popular way of relating the LEED/PES symmetry has some appeal, designating the photoelectron as the time-reversed LEED state appears to be an arbitrary choice - we could just as easily ask for a time-reversed PES state to bring them into an equivalence. The correct way to understand the LEED/PES symmetry is through the more elaborate analysis built from scattering theory, which will be discussed shortly.

The single-electron photoemission theory has been revised and extended to suit particular experimental circumstances, most notably into the relativistic domain [4.27, 4.28] for spin-polarised experiments, but it obviously fails when many-electron processes contribute strongly to the spectrum - such as the famous 6 eV many-body satellite in the spectrum of nickel [4.29]. Calculations that explicitly incorporate the effects of excited states are substantially more difficult than those for the single-electron groundstate, and so far there is no consensus on a preferred calculative scheme [4.30].

4.6 Calculating the Photocurrent

The standard single-electron approach to the photocurrent [4.24, 4.25, 4.26] uses time-independent scattering theory, and no evolution of initial to final states is considered. The real-space model partitions the model into two distinct regions: the region representing the sample contains an assembly of finite-ranged (muffin-tin) scattering potentials, whilst the remaining region is empty space, except for an angle-resolving detector placed a large distance from the sample (see figure 4.g).

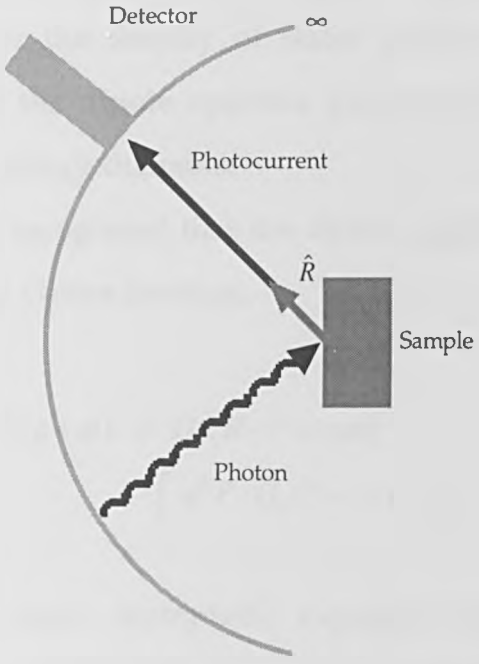

Figure 4.g, showing the experimental arrangement used to model the photocurrent. Adapted from Feibelman and Eastman [4.31]

The photocurrent is described by Caroli's equation, which may be written as

$$I(\vec{k}_{\parallel},\varepsilon+\omega) = -\frac{1}{\pi}\mathcal{I}m\left\{\left\langle \Phi_{\bar{k}_{\parallel}} \middle| G_2^{-}(\varepsilon+\omega)\,\Lambda^{*}\,G_1^{+}(\varepsilon)\,\Lambda\,G_2^{+}(\varepsilon+\omega) \middle| \Phi_{\bar{k}_{\parallel}} \right\rangle\right\}, \qquad (4.7)$$

where G_2^{+}, G_2^{-} are outgoing and incoming single-electron Green

functions at energy $(\varepsilon+\omega)$, with ω the photon energy, $\vec{k}_{\parallel} = \sqrt{(\varepsilon + \omega)}$ and G_1^+ is a single-electron Green function at energy ε. Commutation relations give the acceleration formula for the dipole operator [4.32]

$$\Lambda = \frac{2i\sqrt{2}}{\omega c}\left(\vec{A}.\nabla V\right) \tag{4.8}$$

and the potential thus acts as a source for the photocurrent in addition to being a scattering centre. The Caroli equation (4.7) is essentially an expression for the density of states covering the two energies ε and $(\varepsilon+\omega)$, with the dipole operator providing the means for a transition between the energy domains.

Adawi recognised that the dyson equation (see section 3.7) for the higher energy Green function,

$$\begin{aligned} G_2^+(\vec{R},\vec{r};\varepsilon+\omega) &= G_0(\vec{R}-\vec{r};\varepsilon+\omega) \\ &+ \int d^3\vec{r}'\ G_0(\vec{r}-\vec{r}';\varepsilon+\omega)\ V(\vec{r})\ G_2^+(\vec{r}',\vec{R};\varepsilon+\omega), \end{aligned} \tag{4.9}$$

permits the same asymptotic expansion for both free-space Green functions in a closed form. This occurs because $V(\vec{r})$ exists only within the region of the sample, thereby constraining $\vec{r}$ to lie within the sample volume. Hence, by writing

$$\begin{aligned} G_0(\vec{R} - \vec{r};\varepsilon+\omega) &\underset{R\to\infty}{\approx} \frac{e^{ik\left(R-\hat{R}\cdot\vec{r}'\right)}}{R} \\ &= \frac{e^{ikR}}{R}e^{i\vec{\kappa}.\vec{r}}, \end{aligned} \tag{4.10}$$

where $\vec{\kappa} = -k\hat{R}$, we have a momentum that flows from the detector and into the sample, which may also be interpreted as a hole-state current

flowing towards the detector. By substituting (4.10) into both G_0 terms in equation (4.9), we can form

$$G_2^+(\vec{R},\vec{r};\varepsilon+\omega) = \frac{e^{ikR}}{R}\Phi_{\vec{\kappa}}^{LEED}(\vec{r};\varepsilon+\omega), \qquad (4.11)$$

where $\Phi_{\vec{\kappa}}^{LEED}$ is the Lippmann-Schwinger equation for the time-reversed LEED state

$$\Phi_{\vec{\kappa}}^{LEED}(\vec{r};\varepsilon+\omega) = e^{i\vec{\kappa}\cdot\vec{r}'} + \int_{-\infty}^{\infty} d\vec{r}''\, e^{i\vec{\kappa}\cdot\vec{r}''} V(\vec{r}'') G_2^+(\vec{r}'',\vec{r}';\varepsilon+\omega). \qquad (4.12)$$

This may be used to derive the multiple-scattering form of the time-reversed LEED state, and the real-space photocurrent equation [4.33] follows immediately by direct substition into the Caroli equation (4.7), which may now be written as

$$I(\vec{k}_{\parallel},\varepsilon+\omega) \underset{R\to\infty}{\approx} -\frac{1}{\pi R^2}\mathcal{I}m\left\{\Phi_{\vec{\kappa}}^{*LEED}(\varepsilon+\omega)\,\Lambda^*\,G_1^+(\varepsilon)\,\Lambda\Phi_{\vec{\kappa}}^{LEED}(\varepsilon+\omega)\right\}. \qquad (4.13)$$

A derivation of the multiple-scattering time-reversed LEED state will now be outlined.

We consider scattering within the sample according to the following geometry (see figure 4.h, overleaf):

$\vec{r}$ lies within a scattering site centred at $\vec{R}_n$; $\vec{r} = \vec{R}_n + \vec{r}_n$,

$\vec{r}'$ lies within a scattering site centred at $\vec{R}_m$; $\vec{r}' = \vec{R}_m + \vec{r}_m'$.

Expressing equation (4.12) with these coordinates, and substituting the muffin-tin potential form for the potential $V(\vec{r}'')$, we can write

$$\Phi_{\vec{\kappa}}^{LEED}(\vec{r};\varepsilon+\omega) = e^{i\vec{\kappa}\cdot(\vec{R}_n+\vec{r}_n)} + \sum_m \int d\vec{r}_m' e^{i\vec{\kappa}\cdot(\vec{R}_m+\vec{r}_m')} v(\vec{r}_m') G_2^+(\vec{r}_n,\vec{r}_m';\varepsilon+\omega). \qquad (4.14)$$

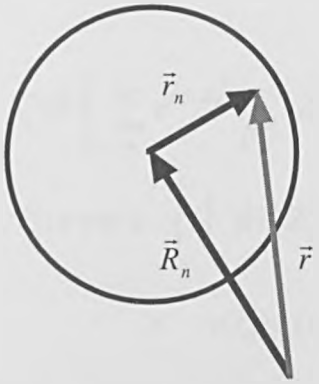

Figure 4.h; showing the labelling scheme used for the vectors in the multiple-scattering time-reversed LEED state.

The plane waves $e^{i\vec{\kappa}\cdot\vec{r}_n}$, $e^{i\vec{\kappa}\cdot\vec{r}'_m}$ may be expanded in an angular momentum basis using Bauer's formula,

$$e^{i(\vec{\kappa}\cdot\vec{r})} = 4\pi \sum_L i^l j_l(\kappa r) Y_L^*(\hat{\kappa}) Y_L(\hat{r}), \tag{4.15}$$

where $L = l, m$ denotes the orbital and spin angular momentum indices respectively, producing

$$\begin{aligned}\Phi_{\vec{\kappa}}^{LEED}(\vec{r};\varepsilon+\omega) &= e^{i\vec{\kappa}\cdot\vec{R}_n}\left[4\pi\sum_L i^l j_l(\kappa r_n) Y_L^*(\hat{\kappa}) Y_L(\hat{r}_n)\right] \\ &+ 4\pi\sum_m e^{i\vec{\kappa}\cdot\vec{R}_m}\sum_L i^l Y_L^*(\hat{\kappa}) \int d\vec{r}'_m\; G_2^+(\vec{r}_n,\vec{r}'_m;\varepsilon+\omega) \\ &\qquad \times v(\vec{r}'_m) j_l(\kappa r'_m) Y_L(\hat{r}'_m).\end{aligned} \tag{4.16}$$

Substituting the multiple-scattering form of the Green function,

$$\begin{aligned}G_2^+(\vec{r}_n,\vec{r}'_m;\varepsilon+\omega) = \sum_{n\,m\,LL'}\big[\; & Z_L^n(\vec{r}_n;\varepsilon+\omega) Y_L^*(\hat{r}_n)\tau_{LL'}^{nm}(\vec{r}_n,\vec{r}'_m;\varepsilon+\omega) \\ & \times Z_{L'}^m(\vec{r}'_m;\varepsilon+\omega) Y_{L'}(\hat{r}'_m) \\ & - Z_L^n(\vec{r}_<;\varepsilon+\omega) Y_L^*(\hat{r}_<) j_l^n(\vec{r}_>;\varepsilon+\omega) Y_{L'}(\hat{r}_>)\delta_{LL'}\delta_{n\,m}\;\big],\end{aligned} \tag{4.17}$$

and rearranging, we can form an expression containing two integral terms

(labelled A and B) that can be simplified:

$$\Phi_{\vec{\kappa}}^{LEED}(\vec{r};\varepsilon+\omega) = 4\pi \sum_{nL} i^l Y_L^*(\hat{\kappa})\Bigg[\sum_m e^{i\vec{\kappa}\cdot\vec{R}_m} \sum_{L'L''} Z_{L'}^n(\vec{r}_n;\varepsilon+\omega) Y_{L'}^*(\hat{r}_n)$$
$$\times \tau_{L'L''}^{nm}(\vec{r}_n,\vec{r}'_m;\varepsilon+\omega) \overset{A}{\Bigg\{} \int d\vec{r}'_m Z_{L''}^m(\vec{r}'_m;\varepsilon+\omega) Y_{L''}(\hat{r}'_m)$$
$$\times \quad v(\vec{r}'_m) j_l(\kappa r'_m) \Bigg\} \qquad (4.18)$$
$$+ e^{i\vec{\kappa}\cdot\vec{R}_n} \overset{B}{\Bigg\{} \quad j_l(\kappa r_n) - \sum_{L'} \int d\vec{r}_n \; Z_{L'}^n(\vec{r}_<;\varepsilon+\omega) Y_{L'}^*(\hat{r}_<)$$
$$j_{l'}{}^n(\vec{r}_>;\varepsilon+\omega) Y_{L'}(\hat{r}_>) \; j_l(\kappa r_n) \Bigg\} \Bigg].$$

By writing the scattering solution in a radial wave function basis,

$$Z_L(\vec{r}) = \sum_{L'} R_{L'}(\vec{r};\varepsilon+\omega) \mathrm{t}^{-1}_{L'L}, \qquad (4.19)$$

and recognising the defining equation for the t matrix, the first integral expression (A) can be simply reduced to the Kronecker delta $\delta_{LL''}$. The remaining integral expression can be re-written in terms of the single-site scattering Green function and, after a little algebra, can be reduced to the Lippmann-Schwinger equation for single-site scattering

$$j_l(\kappa r_n) - R_L(\vec{r}_n;\varepsilon+\omega)$$
$$+ \int dr \; G^+(\vec{r}_n,\vec{r};\varepsilon+\omega) v(\vec{r}) j_l(\kappa r) = 0, \qquad (4.20)$$

The multiple-scattering equation for the time-reversed LEED state becomes, therefore

$$\Phi_{\vec{\kappa}}^{LEED}(\vec{r};\varepsilon+\omega) = 4\pi \sum_m e^{i\vec{\kappa}\cdot\vec{R}_m} \sum_{nLL'} i^l Y_L^*(\hat{\kappa}) Z_L^n(\vec{r}_n;\varepsilon+\omega) Y_L^*(\hat{r}_n)$$
$$\times \tau_{LL'}^{nm}(\vec{r}_n,\vec{r}'_m;\varepsilon+\omega). \qquad (4.21)$$

For metallic systems, we can assume symmetry within the surface reciprocal net and derive a layer-resolved real-space photocurrent equation which is both computationally efficient and suitable for modelling a relaxed surface. In the final chapter of this thesis the results of a study of the Y/W(110) system will be presented, which includes calculated photocurrents for an idealised Y surface.

4.7 References

[4.1] S. Hüffner, "Photoelectron Spectroscopy", Springer Series in Solid State Sciences, Vol.82, 1-20, Springer-Verlag, (1995).

[4.2] N. Harris, "Modern Vacuum Practice", McGraw-Hill Book Company Europe, (1989).

[4.3] See, for instance, M.V. Kurepa, Vacuum, Vol. 37, 3, (1987).

[4.4] R. Z. Bacharach, "Synchrotron Radiation Research"Volume 1, 1-54, Plenum Press, (1992).

[4.5] W. Heitler, "The Quantum Theory of Radiation", Third Edition, Chapter II, Oxford University Press, (1954).

[4.6] J. B. Pendry in "Photoemission and the Electronic Properties of Surfaces", (ed.s) B. Feuerbacher, B. Fitton, R. F. Willis, John Wiley and Sons, (1978).

[4.7] J. W. Gadzuk in "Photoemission and the Electronic Properties of Surfaces", *(ibid).*

[4.8] T. Koopmans, Physica, Vol.1, 104, (1934).

[4.9] T. Gustafsson and E. W. Plummer in "Photoemission and the Electronic Properties of Surfaces", *(ibid).*

[4.10] W. L. Schaich in "Photoemission in Solids I", (ed.s) M. Cardona and L. Ley, Topics in Applied Physics Vol. 26, Springer-Verlag, (1978).

[4.11] L. I. Schiff, "Quantum Mechanics", Third Edition, Chapter 6, McGraw-Hill Book Company, 1968.

[4.12] see, for instance, the discussion by Pendry in [4.6].

[4.13] J. W. Cooper, Phys. Rev. 128, 681, (1962).

[4.14] J. J. Yeh and I. Lindau, "Atomic Subshell Photoionisation Cross-Sections and Asymmetry Parameters" Atomic Data and Nuclear Data Tables, Vol. 32, 1, (1985).

[4.15] W. Lenth, F. Lutz, J. Barth, G. Kalkoffen and C. Kunz, Phys. Rev. Lett., Vol. 41, 1185, (1978);
R. G. White, R. I. R. Blyth, N. P. Tucker, M. H. Lee and S. D. Barrett, J. Synchrotron Rad. , Vol. 2, 261, (1995).

[4.16] N. P. Tucker, R. I. R. Blyth, R. G. White, M. H. Lee, A. W. Robinson and S. D. Barrett, J. Synchrotron Rad., Vol. 2, 252.

[4.17] N. P. Tucker, R. I. R. Blyth, R. G. White, M. H. Lee, C. Searle and S. D. Barrett, J.Phys: Condens. Matter, Vol. 10, 6677-6686, (1998).

[4.18] W.F. Egelhoff Jr., Phys.Rev.B, Vol. 30, 1052, (1984).

[4.19] C. N. Berglund and W. E. Spicer, Phys. Rev. ,Vol. 136, A1030 (1964).

[4.20] W. Schaich and N. W. Ashcroft, Phys. Rev., B3, 2452, (1971).

[4.21] C. Caroli, D. Lederer-Rozenblatt, B. Roulet, D. Saint-James, Phys.Rev., Vol. B 8, 4552, (1973).

[4.22] L. V. Keldysh, Soviet Physics JETP, Vol.20, 1018, (1965).

[4.23] I. Adawi, Phys.Rev.,Vol. 134, A788, (1964).

[4.24] G.D.Mahan,Phys.Rev.,B 2, 4334 (1970).

[4.25] A.Leibsch, Phys.Rev., Vol. B 13, 544, (1976).

[4.26] J. B. Pendry, Surface Science, Vol. 57, 679, (1976).

[4.27] B. Ginatempo, P. J. Durham and B. I. Gyorffy, J. Phys.: Condens. Matter, Vol. 1, 6483-6501, (1989).

[4.28] P. D. Johnson, Rep. Prog. Phys., Vol. 60, 1217, (1997).

[4.29] D. R. Penn, Phys. Rev. Lett., Vol. 42, 921, (1979).

[4.30] M. Springer, F. Aryasetiawan, K. Karlsson, Phys. Rev. Lett., Vol 80, No. 11, 2389-2392, (1998).

[4.31] P. J. Feibelman and D. E. Eastman, Phys. Rev. B, Vol. 10, 12, 4932, (1974).

[4.32] P. J. Durham, J. Phys. F: Metal Phys., Vol. 11, 2475, (1981).

[4.33] P. J. Durham, "Electron Spectroscopy of Metallic Systems", in "The Electronic Structure of Complex Systems", NATO ASI Series B: Physics Vol. 113, 709-757, Plenum (1984).

Chapter 5

Experiments and Analysis

The principal aim of this chapter is to examine the surface electronic structure of Y(0001) by comparing and analysing photoemission spectra from both bulk and ultra-thin film single crystals. In particular, we aim to identify those changes to the electronic structure of Y(0001) that result from yttrium being in the presence of W(110). All of the original calculations presented in this thesis were performed using node tci25 of the IBM-cluster facility at Daresbury Laboratory.

The chapter begins with a review of previously published ARUPS data from a bulk Y(0001) crystal, which is compared with a bulk band structure calculated using the LMASA-46 code. Next, original ARUPS data from W(110) is presented, which is again compared with its bulk band structure. ARUPS data from the Y/W(110) ultra-thin film single crystal is then shown and analysed via a series of model calculations, which includes the first real-space photocurrent calculations for Y(0001). The chapter concludes with a summary of the results and suggestions for future work.

5.1 Bulk Single Crystal Studies

One of the earliest reported studies on the electronic structure of yttrium was by Loucks in 1966 [5.1], who used the augmented plane wave (APW) method to calculate the Fermi surface and provide a crude

estimate for the density of states (DOS). However, it was not until 1978 that Loucks' calculation was shown to be in reasonable agreement with the de Haas-van Alphen experiments of Mattocks and Young [5.2]. This paucity of literature, both theoretical and experimental, graphically illustrates the main problem with early studies on the electronic structure of elemental yttrium; obtaining a sufficiently pure sample to gain useful data. By the middle of the 1980's, however, refining using solid state electrotransport was producing the first high-purity rare earth metal samples, and surface science experiments first became feasible.

Barrett and Jordan [5.3] initiated the modern era of yttrium studies with single-crystal photoemission experiments on Y(0001). This was followed by a series of ARUPS experiments on various crystal faces, which showed the yttrium valence band to be in good agreement with self-consistent LMTO band structure calculations [5.4]. During this time, the anomolous SODS feature at the higher binding energy of ~9.6 eV was investigated and its main properties identified. To date, the origin of this state has eluded explanation, and we shall defer discussing the SODS in detail until later in the chapter.

In order to investigate one suggested explanation for the SODS as deriving from a many-body resonance with an unoccupied surface state, Blyth *et al* [5.5] performed the first momentum (k)-resolved inverse photoemission experiments (KRIPES) on Y(0001). The investigation found no evidence for many-body features in the unoccupied states and the authors noted that their data is well matched by the linear augmented plane wave (LAPW) band structure calculated by Blaha *et al* [5.6].

It will be instructive for the ultra-thin film analysis that follows to compare one data set from bulk single crystal yttrium, the 40 eV photon energy Y(0001) ARUPS data presented in Barrett [5.4], with an original

bulk band structure and DOS calculated using the LMASA-46 code.

5.2 ARUPS for Y(0001) from a Bulk Single Crystal

Although the data shown overleaf (fig. 5.a) was first published by Barrett [5.4], a more complete account of this experiment was drafted by Blyth*et al* [5.7] and the experimental details derive from this latter source.

5.2.1 Experimental

The experiment was performed on beamline 6.2 of the Daresbury SRS in the early 1990's, when this beamline had a total energy resolution of 0.15 eV. The yttrium sample, obtained from Dr. D. Fort (School of Metallurgy and Materials, The University of Birmingham, U. K.), was cleaned *in situ* by approximately 30 cycles of argon bombardment (3-4 kV), followed by annealing to ~ 875 K to restore the surface order. After cooling to room temperature, the sample cleanliness was monitored using UPS. Blyth *et al* reported that the surface showed good order prior to data collection, as evidenced by sharp LEED spots, and that the base pressure during the ARUPS measurements was 2×10^{-10} mbar.

5.2.2 The Bulk Y(0001) ARUPS Spectra

The ARUPS data, shown in figure 5.a, has three prominent valence band features displaying a remarkable degree of symmetry in their dispersion about normal emission ($\theta = 0°$). By convention, these three features with binding energies 0.4, 1.7 and 3.2 eV in normal emission are labelled a, b and c and are typical of the valence band for HCP rare earth metal samples of this kind.

The dispersion shown by the spectral features b and c along ΓM is

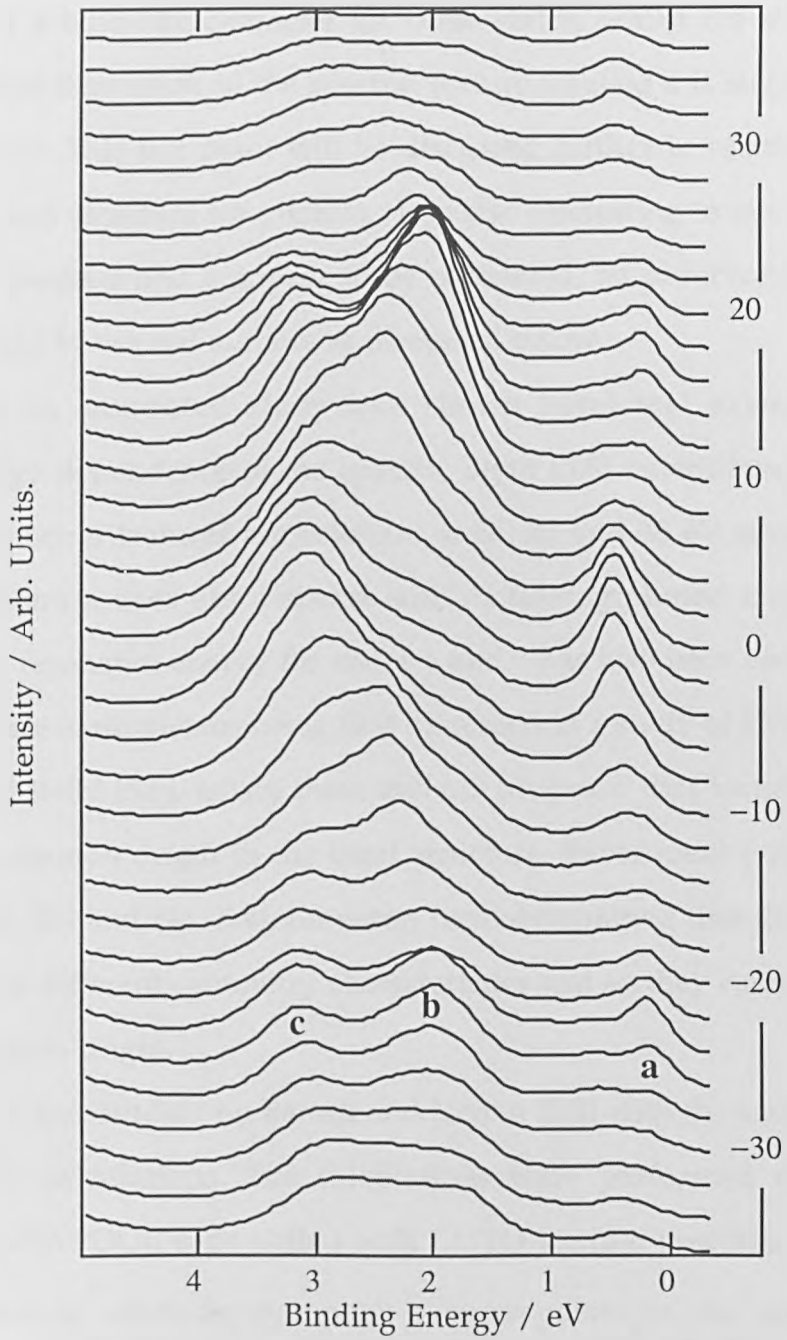

Fig. 5.a: ARUPS data collected along ΓM from a Y(0001) bulk crystal, adapted from Barrett [5.4].The photon energy used was 40 eV, with angle of incidence 55°.

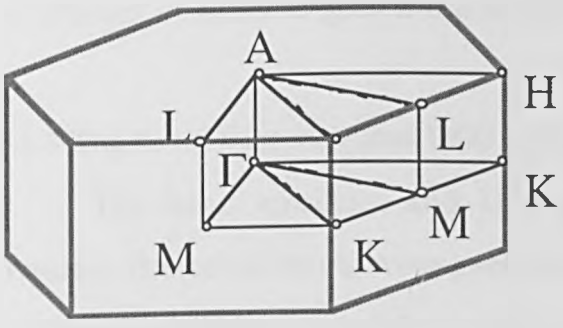

Fig. 5.b: symmetry points in the Brillouin zone for an HCP lattice.

indicative of a bulk-like character for these states, whilst the absence of any significant dispersion to the spectral feature labelled a is suggestive of a surface state. This last point will be discussed further in relation to the calculated band structure for yttrium. It is also interesting to note that the intensity of peaks a and c appear to be correlated, an observation which has been made by several authors as discussed below.

From an associated study (not shown here) that examined the photon-energy dependence of the spectra, Blyth [5.8] determined that the a, b and c spectral features are resonant at 38, 32 and 38 eV respectively, and that feature a does not disperse with increasing photon energy. The concomitant resonance energy for states a and c has also been observed in other HCP rare earth metals, being first discussed in a study of Gd(0001) by Himpsel and Reihl [5.9], where these authors proposed that features a and c shared a common origin in the band structure. Subsequent polarisation studies on Y, Gd and Ho [5.4], however, have determined that the a and c states possess different symmetry characteristics and so they cannot derive from a common origin.

Peak b was studied by Barrett and Jordan [5.3] with the assistance of photocurrent calculations. The calculations were performed using the Daresbury NEWPOOL code with a bulk LMTO yttrium potential, and led these authors to conclude that peak b corresponds to the upper (Γ_{4-}) critical point along ΓA . We shall next present the DOS and band structure of yttrium in order to gain more insight into the ARUPS data.

5.2.3 The Band Structure and DOS for Yttrium

The band structure and DOS are shown in figures 5.c and 5.d overleaf.The calculations were performed scalar-relativistically and are in excellent agreement with other similar calculations for yttrium [5.6, 5.8,

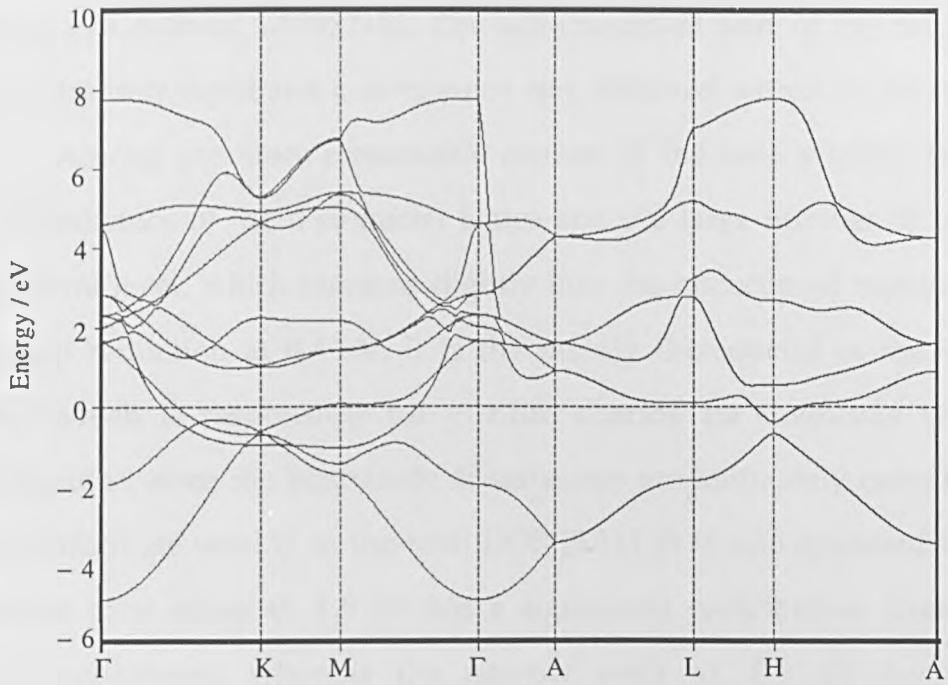

Figure 5.c: the bulk band structure for yttrium.

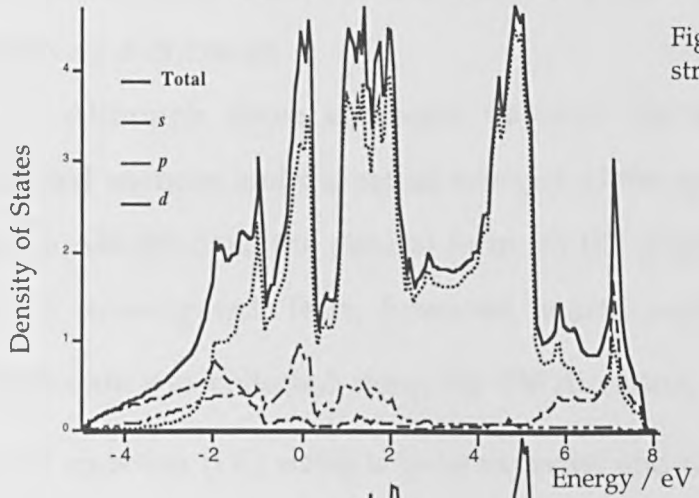

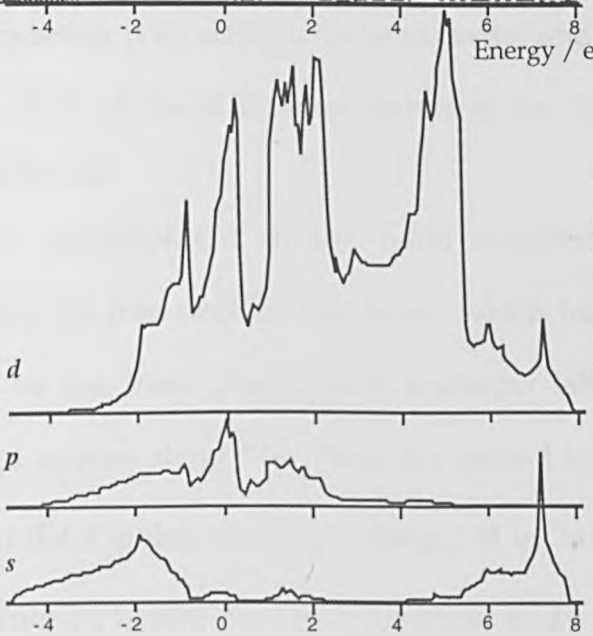

Figure 5.d: The DOS for yttrium. Contributions to the total DOS from states with s, p and d character are also shown. All energies are relative to the Fermi level.

5.10]. A lattice constant of 6.89259 atomic units (a.u.) was assumed together with a c/a ratio of 1.57937155. The self-consistent part of the calculation was extremely rapid and convergence was achieved within 10 iterations.

Among the more remarkable aspects of the bulk yttrium DOS are the dominance of the d-character states and the large number of states at the Fermi level, which increase slightly into the unoccupied region before a sharp reduction at 0.4 eV. It is the mainly d-character of the valence band which is responsible for yttrium sharing its chemistry with the lanthanides, since the lanthanide 4f states are predominately core-like and only contribute weakly to the total DOS [5.11]. It is also apparent that the peak in total states at -1.9 eV has a significant contribution from states with s-character, whereas the narrow peak at -0.9 eV has almost exclusively d-character.

Although there are some obvious discrepancies between the calculated energies and the actual energies of the spectral features a, b and c in the ARUPS data, the general form for the dispersion of the states can still be investigated. It is, however, worth noting that although the ARUPS data was collected along the ΓM direction, some folding with the normal emission (ΓA) states is to be expected and that this may account, in part, for some of the differences between the experimental data and the calculated bands.

The development of the band structure can be discussed by nominating the free-electron like band, which has energy -4.9 eV at the Γ point, to be the "first" band, with a similar labelling for the other two bands that appear along ΓM. Thus, the second band, which has an energy of -2eV at the Γ point, develops along ΓM by initially moving to a lower binding energy, before changing direction midway between Γ and M and

moving back to a higher binding energy, ending at the M point close to the third band. The third band enters the occupied region approximately midway between Γ and M and moves to a higher energy. This dispersive behaviour is certainly reminiscent of features b and c in the ARUPS data. However, it is the spectral feature closest to the Fermi edge (a) which can be identified more precisely, because there are no states at the Γ point in both ΓM and ΓA directions. Recalling that feature a is most intense at the Γ point, and that it shows no dispersion with increasing photon energy, it can unequivocally be assigned to emission from a surface state.

It is also notable that the first band defines the extent of the band structure, since no states exist beyond -4.9 eV. Consequently, this band structure does not account for the SODS, which would necessarily be placed at a higher energy. It will be interesting to examine some of the more defining properties of the SODS feature which may provide clues as to its origin before examining the Y(0001) ultra-thin film data.

5.3 Some Thoughts on the SODS

The SODS was first published in a study of Gd(0001) by Jordan [5.12], and has subsequently been seen on every bulk single crystal rare earth metal studied to date. The fundamental nature of this emission feature can be summarised in the following statements:

1) the SODS derives from a state deep in the valence band (~ 9.6 eV) which is only seen on clean (0001) bulk crystal surfaces (see figure 5.e overleaf);

2) the intensity (width) of this emission feature is directly (inversely) correlated with the degree of surface order;

3) it exhibits resonance with photon energies ~40 eV;

4) experiments with Sc(0001) [5.13] have resolved two components in the SODS;

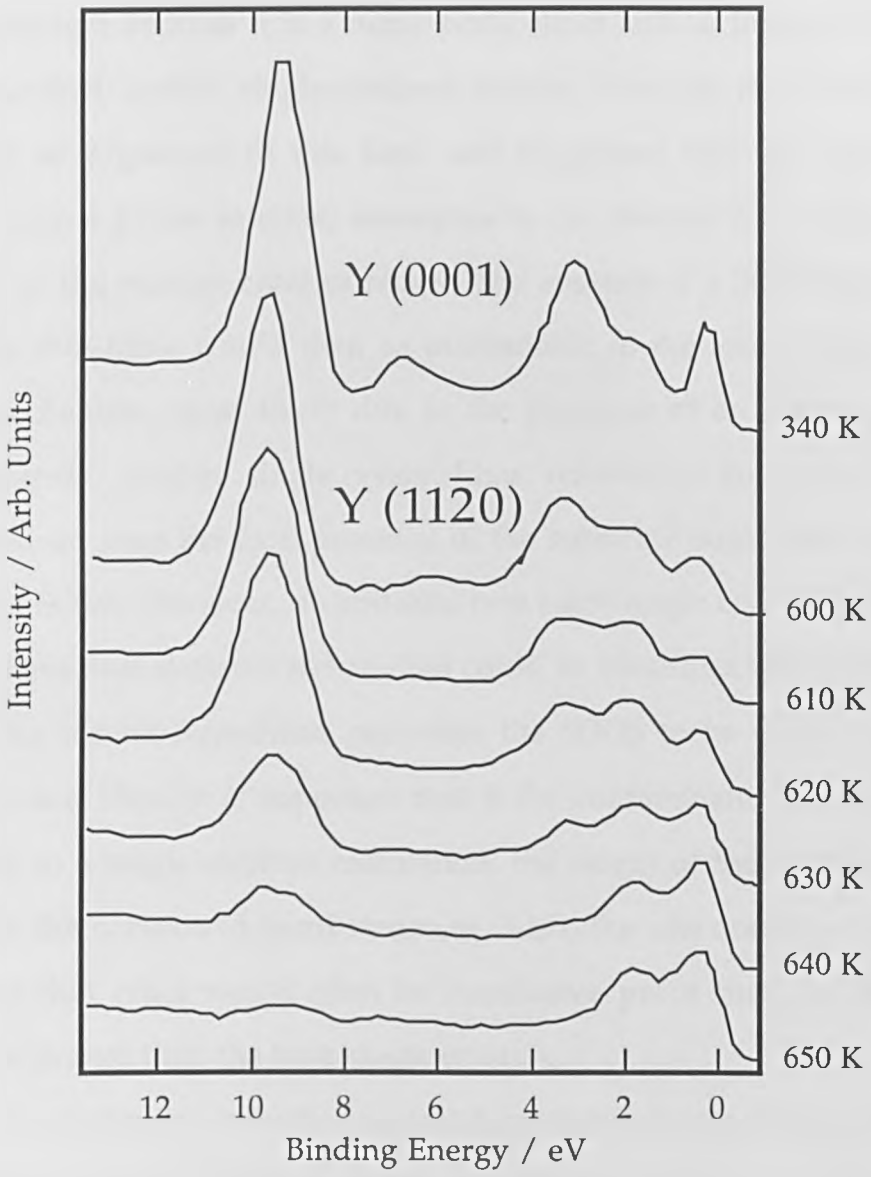

Figure 5.e.The SODS exists only on the (0001) surface of rare earth metals.The spectra above show the emergence of the SODS feature as the yttrium reconstructs from the four-fold symmetric (11$\bar{2}$0) surface, maintained at an elevated temperature, to the (0001) surface at a lower temperature. An ideal (0001) surface is also shown for comparison. Adapted from Barrett *et al.*[5.14].

5) single-electron theory cannot identify any state in any of the rare earth metals which could give rise to a SODS.

There are two very obvious hypotheses that may be proposed to explain the list of properties above and these are not mutually exclusive. Firstly, we can postulate that the SODS does not appear in any calculated band structure because it is a many-body effect and is, therefore, simply not described within single-electron theory. Patchett *et al.* [5.13] have pursued an argument of this kind and suggested that the SODS may derive from a 2-hole satellite, analogous to the famous 6 eV many-body satellite in the valence band of nickel. The absence of a SODS feature on the ultra-thin films would then be attributable to the loss of this many-body mechanism, most likely due to the presence of an interface state. Consequently, 'thicker' single crystal films, relieved of their lattice strain and removed from the local potential of the substrate ought once again to display a SODS. However, no epitaxial rare earth single crystals published to date have ever shown a feature that could be identified with a SODS.

The second hypothesis considers the SODS to be derived from a contaminant. Thus, it is supposed that if the contaminant were correctly included in a single-electron calculation, the origin of the SODS may be found in the compound band structure. Also, the absence of a SODS on the ultra-thin films would then be conclusive proof that the epitaxial films are cleaner than the bulk single crystals.

The difficulty with this second hypothesis comes from naming a suitable candidate as the contaminant, since all reports on the SODS feature have claimed that the sample was clean at the time of data collection, and adsorbtion experiments which aimed to reproduce a SODS on ultra-thin films have merely demonstrated the catalytic properties of these films [5.15]. There is, however, one instance in which hydrogen can be proposed as the contaminant, and a short discussion on this argument will follow.

It is well known that rare earth metals have an affinity for hydrogen [5.16]. Since hydrogen is not detectable through Auger transitions and since it also scatters LEED electrons weakly, it can be difficult to characterise on a surface. However, hydrogen adsorbed purely at the surface can be discounted as a source of contamination in ARUPS experiments because this has been well-characterised and is known to produce an emission feature at a binding energy of ~ 3.8 eV [5.17].

The formation of the bulk-like yttrium di-hydride (β-phase) and tri-hydride (γ-phase) can also be discounted, since these stable hydride phases have strikingly different physical properties to pure yttrium that are easily detectable: YH_2 forms a BCC lattice whilst YH_3 is an insulator which usually crumbles to a powder [5.18]. This leaves only the disordered α-phase hydride to be considered, the hydrogen solid-solution which exists for concentrations < 0.2 H/Y.

It is interesting to ponder on the possibility of a hydrogen-solid solution (the disordered α-phase hydride) being responsible for the SODS, possibly through the formation of sp-hybridised orbitals in sub-surface layers. It has been noted [5.4] that the SODS may ultimately derive from states with p-character, because the photon-energy resonance behaviour of the SODS is of the same order in energy as the highest energy p-levels of the rare earths. Unfortunately, calculations for the electronic structure of the various yttrium hydride phases are very difficult, and the electronic structure of the yttrium hydrides is still disputed [5.19].

It is the mobility of hydrogen within the HCP lattice which makes the α-phase hydride so difficult to model, and yet we can speculate that this mobility may also drive the mechanism that causes the giant reconstructions of the rare earths, if this is considered to be instead a re-

crystallisation of the surface.

The model that we have in mind is of an open surface which is cooling in the presence of an escaping gas. A gas molecule at the surface may experience scattering with a phonon from the surface reciprocal net and propagate back into the crystal, thereby transporting momentum from the surface and into the bulk, or scatter away from the surface into free space, thereby removing momentum from the surface layer altogether. In this last instance, we have a mechanism for cooling which could seed the growth of a close-packed crystal from the surface and into the bulk. Evidently this rough model does little more than speculate on a possible mechanism for an unproven phenomenon, but Barrett has reported that it is only with slow cooling that the reconstructions form [5.10].

5.4 The W(110) ARUPS Experiments

Tungsten has a long and important history within the study of surface electronic structure, since it was the analysis of UPS data from W(001) that first conclusively demonstrated the existence of electronic states local to the surface [5.20, 5.21]. Although ultra-thin film studies of yttrium on iron [5.22], and a variety of rare earth metals on divers transition metal substrates have been reported [5.23], there is good evidence from core-level studies that substitutional alloying occurs. Consequently, no single crystals have been reported grown on non-refractory metal substrates. The reasons for choosing W(110) as a substrate for the growth of ultra-thin film yttrium have been discussed in the introductory chapter of this thesis. We quote them again here; no substitutional alloying takes place at the interface and the packing density of the W(110) face promotes Y(0001) growth.

In order to understand the part played by W(110) in these ultra-thin film studies, we need first to examine and understand the electronic structure of W(110). In what follows, original data taken with a VG noble-gas discharge lamp is presented and consequently, the light source has no specific polarisation.

5.4.1 The ADES Chamber

Figure 5.f, below, depicts a schematic diagram of the Angle Dispersive Electron Spectrometer (ADES) UHV system used by the Rare Earth Group at Liverpool for ARUPS experiments.

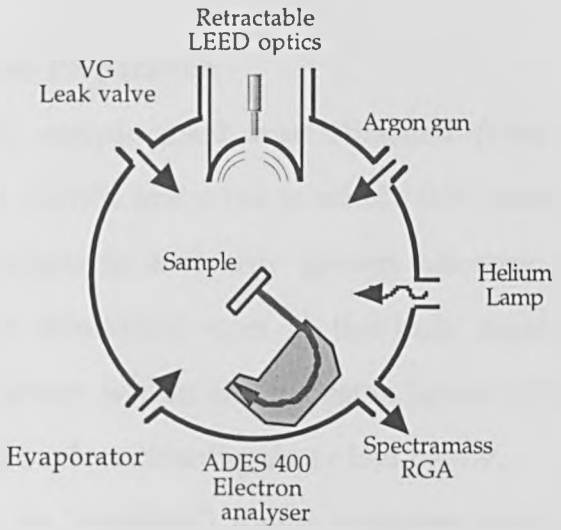

Figure 5.f. A schematic of the ADES chamber.

At the heart of this system is the hemispherical ADES 400 angle resolving analyser, which is mounted on a goniometer permitting rotations up to 330° in the plane normal to the sample. The source of UV radiation is provided by a VG noble-gas discharge lamp. With helium gas supplied to the lamp, two photon energies are available for experiments; HeII provides a moderately bright source of 40.81 eV photons, while HeI supplies a somewhat higher intensity flux of 21.18 eV photons.

The chamber is also equipped with other standard surface science

tools, such as a set of VG rear view retractable LEED optics which can be adjusted to obtain Auger spectra, and a Spectramass quadrupole mass spectrometer for residual gas analysis. UHV is maintained by a diffusion pump with the assistance of titanium sublimation pumps. The total pressure is measured with VG ion and pirani gauges and a base pressure better than $2x10^{-11}$ can be routinely achieved.

Samples are held in the chamber by a VG omniax manipulator. The sample temperature is controlled by electron beam heating, which uses a high voltage Glassman power supply to provide a typical current of 400 mA at 1500 V.

5.4.2 W(110) Sample Preparation

The W(110) sample used was obtained from Goodfellow, who quoted a purity of 99.99% and a cut to within 0.5° from a boule. The most abundent contaminant in a freshly grown tungsten crystal is carbon, which migrates to interstitial sites in the bulk crystal lattice. It is the mobility of this carbon within the tungsten lattice which has led to the standard recipe for surface cleaning described below.

By heating (or 'roasting') a new tungsten sample to ~ 1500K, the carbon impurities undergo transport through the sample, giving rise to an enhanced concentration of carbon in the surface region. By roasting in an atmosphere of $\sim 10^{-6}$ mbar of oxygen, the surface carbon may form CO and CO_2 gases. These may be monitored via their partial pressures during the initial stages of cleaning to gauge the purity of the crystal. The treatment, however, results in the formation of a thick oxide layer, which is removed by rapidly heating (or 'flashing') the sample to a high temperature (~ 2300K) for a few seconds.

The crystal used in this experiment was cleaned in this manner

several times before it was deemed suitable for photoemission experiments. During the course of the experiment, the sample was periodically 'flashed' to ~1800 K to remove residual contamination from vacuum chamber gases. The sample cleanliness was monitored initially with Auger spectroscopy and the surface order was checked with LEED and showed good order prior to data collection.

5.4.3 The W(110) ARUPS Spectra

The ARUPS data for W(110) is presented on the following page and shows good agreement with a previous investigation by Peden and Shinn [5.24]. The HeII ARUPS study of W(110) by Holmes and King [5.25] was expected to show good agreement with the data presented here, since these authors reported using an ADES 400 analyser and employed a similar method of sample preparation to the one described above. However, their data does not compare particularly well with this study and by comparison with tungsten oxide ARUPS measurements [5.24, 5.26] (not shown here), it appears likely that their HeII ΓΣN data was at least partially oxidised.

The W(110) normal emission spectrum collects data along the ΓN direction (see figures 5.g and 5.h, overleaf) and shows 3 prominent spectral features, here labelled as α, β and χ, with binding energies of 0.25, 1.35 and 1.7 eV respectively. A broad and low intensity feature is also present in the spectra that displays a peak at 6.35 eV in normal emission, although this only becomes prominent as the spectral feature labelled δ for emission angles $\theta > 28$ °.

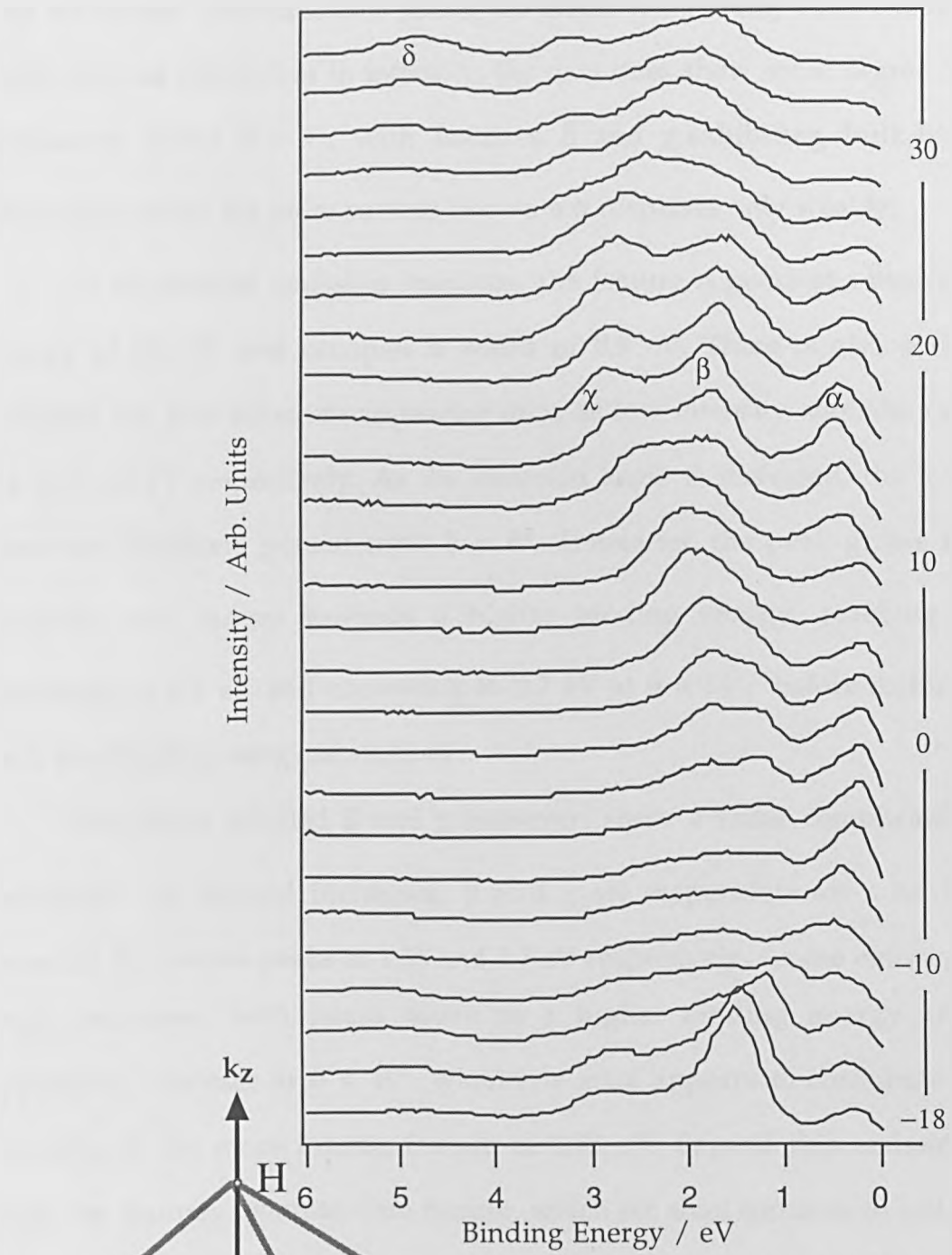

Fig. 5.g: ARUPS data collected along ΓΣN, using HeII radiation (photon energy 40.8 eV).

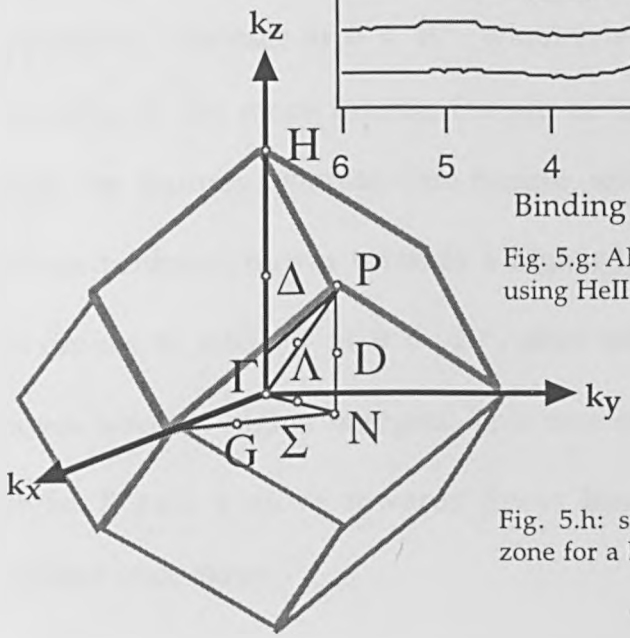

Fig. 5.h: symmetry points in the Brillouin zone for a BCC lattice

The off-normal measurements probe the states lying along ΓΣN. Despite some obvious differences in intensity, the data does show some degree of symmetry about $\theta = 0°$, with features β and χ exhibiting bulk-like dispersion whilst the more surface-like state α disperses only weakly.

In the normal emission spectrum, the feature α peaks at a binding energy of 0.2 eV and occupies a width of 0.9 eV. There is also some evidence for fine structure appearing on α as low intensity shoulders at 0.6 and 0.9 eV respectively. As the emission angle is increased, the low intensity shoulders persist until $\theta = 8°$. Thereafter, the peak grows in intensity and moves towards a higher binding energy, reaching a maximum at 0.5 eV and narrowing to 0.7 eV at $\theta = 14°$, before drifting back to a binding energy of ~0.25 eV.

The peaks labelled β and χ, however, show a more complicated behaviour. At normal incidence, β and χ are responsible for a broad emission that shows peaks at 1.35 and 1.7 eV respectively. As the emission angle increases, both peaks move to a higher binding energy and apparently coalesce at $\theta = 10°$, when one state appears to contribute a shoulder to the more intense feature at 1.75 eV. Beyond this emission angle the features separate. One feature, which we shall continue to call χ for convenience, moves towards a higher binding energy and achieves a maximum of 2.85 eV at $\theta = 20°$, after which a new state appears that moves towards higher energies. This new state reaches 3.3 eV at $\theta = 34°$, whilst β and χ move towards lower binding energies and appear to coalesce once again.

In order to gain a better understanding of this system, we need to examine the calculated band structure and DOS for tungsten.

5.4.4 Band Structure and DOS for W(110)

A scalar-relativistic band structure and DOS for tungsten, which has been calculated using the LMASA-46 code, is shown overleaf (figure 5.i). The calculation used a lattice constant of 5.98136 a.u. for the tungsten and converged to self-consistency within 15 iterations.

The most remarkable aspects of the tungsten DOS are the wealth of structure in the unoccupied region and the predominance of the d-states. The high density of unoccupied d-states just above the Fermi level is also noteworthy, since it is these states which are available for hybridisation with adsorbates.

The calculated bulk band structure shows good overall agreement with previously published bulk band structures for tungsten [5.27, 5.28], but it does also show a few discrepencies with fully relativistic calculations. Most notably, the band structure does not clearly show the famous band gap in the unoccupied states. This loss of detail is not surprising, since tungsten's high atomic number places it firmly within the domain of relativistic materials, and a scalar-relativistic calculation that ignores spin-orbit interactions is necessarily approximate. Over the region of the occupied ΓΣN states, however, the LMASA-46 calculation compares favourably with the fully relativistic band structure that was used by Collins *et al* [5.29] in their investigation of the unoccupied states of W(110).

The calculated band structure shows an agreement in form with the dispersion of the emission features in the W(110) ARUPS data (figure 5.g). Using the same labelling scheme for the bands as was done

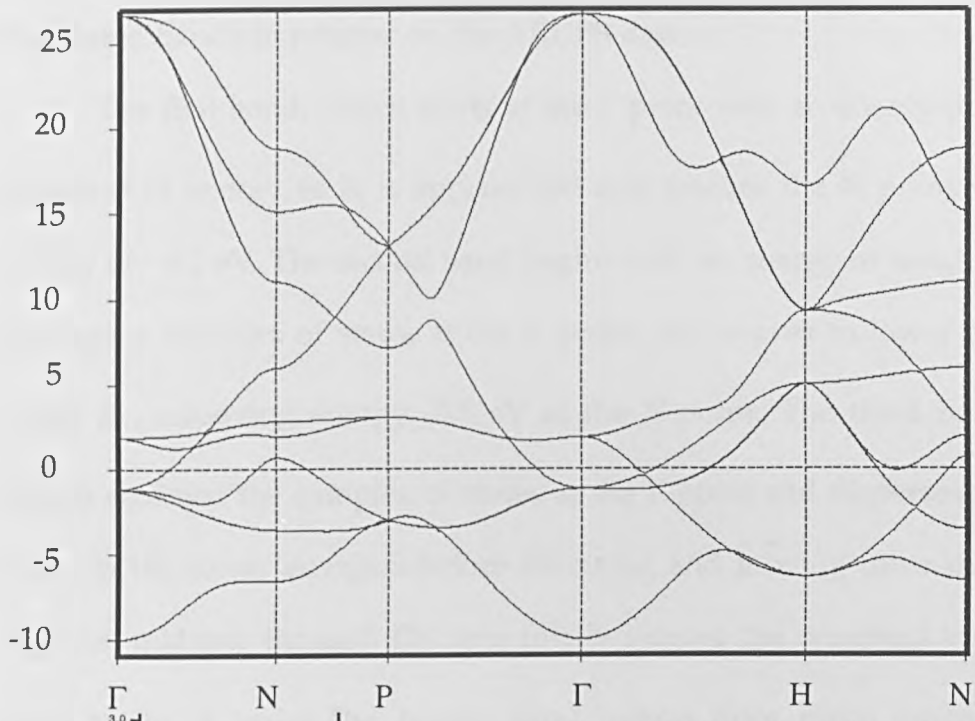

Figure 5.i. The bulk band structure for tungsten

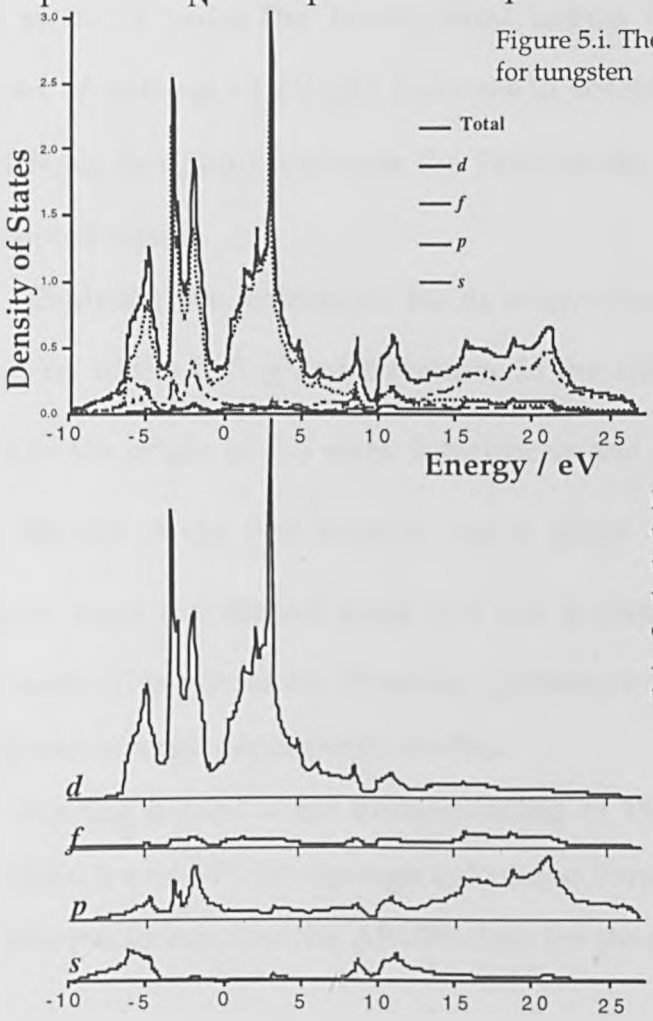

Figure 5.j. The DOS for tungsten. Contributions to the total DOS from states with s, p, d and f character are also shown. All energies are relative to the Fermi level.

previously with yttrium, we can discuss the development of the calculated bands in relation to the ARUPS data.

The first band, which starts at the Γ point with an energy of -10 eV, increases in energy as N is approached and reaches the N point with an energy of - 6.2 eV. The second band begins with an energy of roughly -1 eV amongst a complex of states at the Γ point, and moves to lower energies along Σ , achieving energy -3.5 eV at the N point. The third band also begins amongst the complex of states at the Γ point and disperses initially towards the lower energies before reversing and moving towards higher energies midway through ΓN, and finally leaving the occupied states just prior to the N point.The fourth band begins once more amongst the complex of states at - 1 eV and increases in energy until midway between Γ and N, at this point it crosses the Fermi level and enters the region of unoccupied states.

Evidently, the calculated bands show notable similarities with the dispersion of the α, β, χ and δ features in the ARUPS data. It is tempting to assign the origin of the weak δ feature in the ARUPS data to emission from the top of the first band at the N point, to assign the χ states to emission from the second band and the β states to emission from the third band. This would be, however, premature without full polarisation and photon-energy dependency studies.

Having gained some understanding of the electronic structure of both Y(0001) and W(110) through calculated band structures, we are now in a position to examine the ARUPS data for the ultra-thin films.

5.5 ARUPS from Y/W(110)

At low adsorbate coverages, the structures formed by small transition-metal clusters on W(110) have been the subject of interest, mostly through efforts to understand the adatom-adatom interactions that govern the growth of the higher coverage ordered films. Tight-binding calculations performed by Dhanak and Bassett [5.31] investigated the stability of different geometries for Re and W clusters on W(110), and found that linear chains of Re had a smaller overall energy than a more close-packed triangular configuration. This result is notable because it suggests that the formation of linear chains may be a precursor to the Frank-van der Merwe (FM) monolayer-by-monolayer growth mode, which is believed to be the preferred initial growth mode for Y/W(110). The basic growth mechanisms for epitaxial films (see fig. 5.k., overleaf) arise in essence from a competition between adatom interactions, the sticking probability and the mobility of the adsorbate on the surface.

Amongst the rare earth metals, however, it is the growth of ultra-thin films of Gadolinium on W(110) which has been studied most thoroughly and a significant literature now exists for this system [5.30]. This is fortunate for the analysis of the Y/W(110) system, because Gd and Y share a similar valence electron configuration, they have the same metallic radius of 1.801 Å and they also both adopt the HCP crystal structure at room temperature. Consequently, we shall draw on this resource whenever it is convenient in the analysis that follows.

5.5.1 Beamline 4.1 and Chamber

The experiments were performed on beamline 4.1 of the SRS at Daresbury Laboratory, which has been optimised for ARUPS experiments requiring high angular and energy resolution.

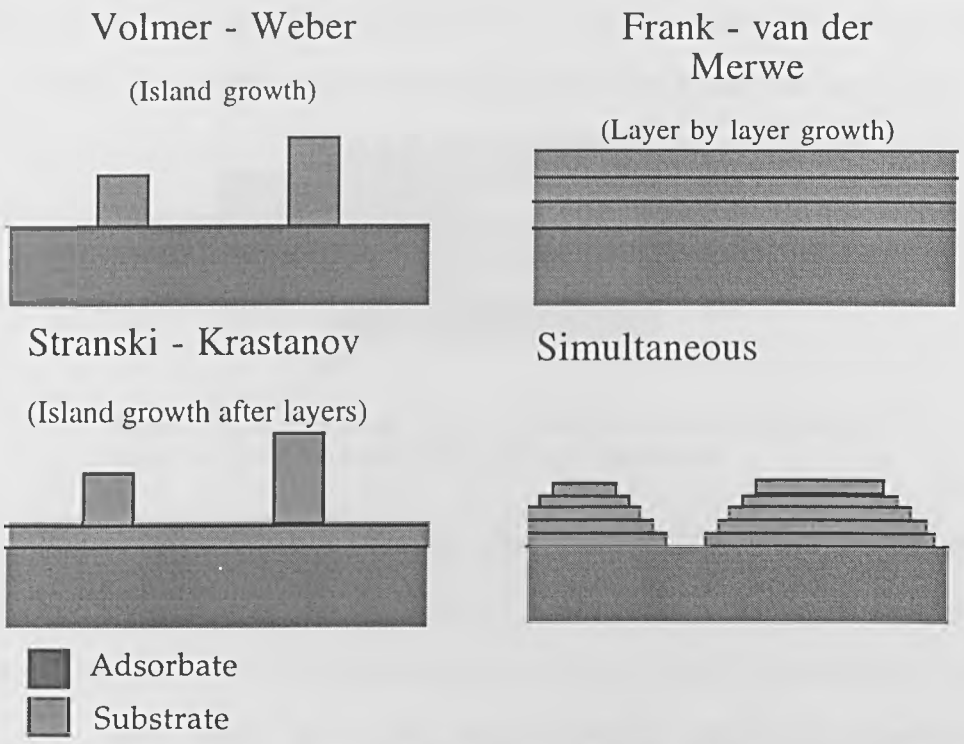

Fig. 5.k, showing the four common types of ultrathin-film growth. After Rhead, Barthés and Argile [5.33].

The beamline monochromator comprises three spherical diffraction gratings that have been chosen to provide first order diffraction over the photon ranges 15-45 eV, 45-130 eV and 100-250 eV.

The beamline 4.1 end station used in these experiments was a Vacuum Science Workshop (VSW) UHV chamber, fitted with a VSW HA 54 angle-resolving electron analyser, Omicron LEED optics, a Vacuum Generators residual gas analyser, a high precision leak valve and a bespoke evaporator, originally used by Dowben *et al* [5.32], and graciously loaned by Dowben's research team to the Liverpool REG (see fig.1, overleaf). When operated at ~1400 K, it has been estimated that a slow but constant evaporation rate of about 1 ML in 20 minutes is possible.

The yttrium source, which was an off-cut from a high purity bulk single crystal, was held loosely wound in the tungsten basket of the evaporator. Heat was applied directly using a low voltage high current (TSP) supply,

whilst cooling was supplied from a flow of chilled water through a copper tube coiled around the evaporator body (a stainless steel vacuum pipe).

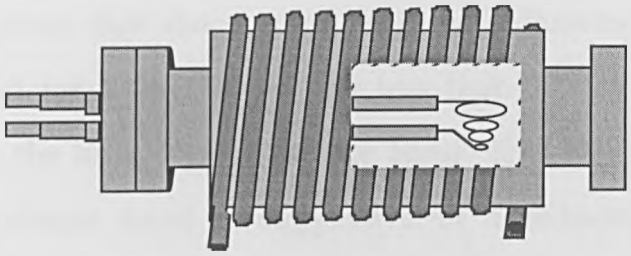

Figure 5.1. A schematic of the water-cooled, tungsten wire basket evaporator, used for the yttrium deposition.

Before use the evaporator was degassed for several days by periodically depositing sample films at about 1500 K. It was considered to be degassed when films could be grown without the pressure rising above 10^{-9} mbar, after which the water-cooling was applied. This allowed the evaporator to be operated at pressures below 10^{-10} mbar during data collection.

The yttrium source was degassed extensively in conjunction with the evaporator. Also, because this highly reactive metal behaves like an additional sublimation pump under these conditions, the experiment had excellent vacuum conditions (~ $5x10^{-11}$ mbar). The ultra-thin film growth was monitored using the Cooper-Minimum technique, as described in the previous chapter.

5.5.2 ARUPS spectra for Y/W(110)

The photon energy dependency of the Y/W(110) system is shown in figure 5.m, overleaf. The data was collected at normal emission (ΓP for tungsten) and used a range of photon energies, from 25 to 45 eV.

The most striking difference between the ARUPS data for the bulk single crystal (see fig. 5.a) and the spectra in fig. 5.m is the lack of any significant emission features over the range 1.5-3.5 eV in the ultra-thin

film crystal. This is surprising, because the bulk yttrium single crystal (see fig. 5.a) has its most intense emission over this range of energies. In fact, we can estimate that the spectral features delimiting the region of the valence band for Y/W(110) occupy less than 50% of the energy region available to the bulk crystal valence band. This narrowing of the ultra-thin film valence band is suggestive of a reduction in the yttrium coordination number compared to that of the close-packed bulk crystal.

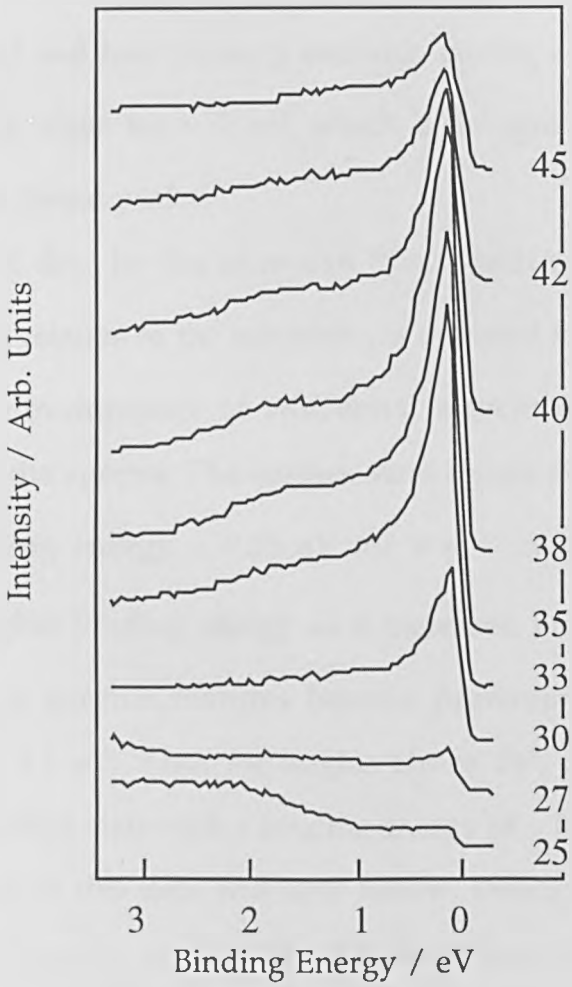

Figure 5. m. The photon energy dependence data for Y/W(110). The film thickness is estimated to be 3 ML. The data was collected in normal emission with an incidence angle of 5°.

The most prominent feature in the ultra-thin film spectra (fig. 5.m) is the intense emission at 0.1 eV, which has a width of ~ 0.1 eV and

shows no significant dispersion as the photon energy increases. This emission has been attributed to a surface state, and is typically seen in the valence band of epitaxially deposited rare earth films [5.34]. The data shows that the surface state resonates at $\hbar\omega$ = 38 eV, which we note is the same resonance energy as the surface state (peak a) on the yttrium bulk single crystal. There is also a weak emission feature which emerges at 0.2-0.25 eV for $\hbar\omega$ = 38 eV and drifts to higher energies as the photon energy increases. A broad and low intensity emission having a binding energy of ~ 1.8 eV resonates when $\hbar\omega$ = 38 eV, which is the same resonance energy as the bulk single crystal peak c.

The ARUPS data for the ultra-thin film, which was collected along the ΓΣN direction relative to the tungsten , is depicted in fig. 5.n (overleaf) and shows the development of additional structures with dispersive characteristics in the spectra. The surface state shows another feature as a shoulder at binding energy ~ 0.35 eV for θ = 4°, which broadens and disperses to a higher binding energy as θ increases. For angles exceeding 18°, a further two spectral features become prominent, having binding energies 1.3 and 1.5 eV. Also, for angles above 24°, a further shoulder appears on the surface state with a binding energy of ~ 0.45 eV.

An analysis of this data will now follow, through a progression of models for the yttrium surface, for the tungsten surface and for the surface of an immiscible alloy of tungsten and yttrium. The calculations, however, will only attempt to establish the general form of the electronic structure and comparisons with absolute values, such as the binding energies of spectral features, will not be attempted.

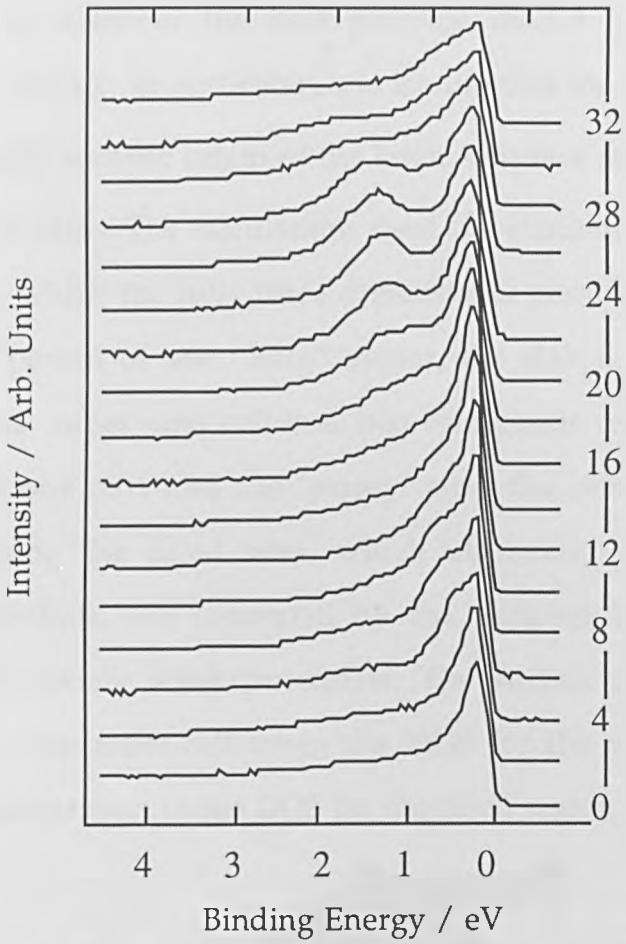

Figure 5.n. ARUPS data for Y/W(110). The film thickness is estimated to be 3 ML. The data was collected with photon energy = 33 eV and an incidence angle of 5°.

5.6 Model Calculations

We have until now tacitly assumed that it is the yttrium valence band that is being measured in the ultra-thin film ARUPS data. Important questions, however, must be answered before we can have any confidence that this is indeed the case. To what extent does the ultra-thin film behave like an ideal 2-dimensional Y(0001) surface? What is the effect of lattice strain on the yttrium electronic structure? How is the yttrium electronic structure altered by local bonding at the interface? It is the purpose of the calculations that follow to attempt to answer these questions.

The super-cell calculations forming this part of the study

endeavoured to discover the best possible model for the electronic structure of Y/W(110). In particular, one feature that the calculations were aiming to identify was the origin of the intense surface state at the Γ point of the ultra-thin films. The calculations used the standard 'slab' technique for surfaces, in which the fully three dimensional periodic lattice is given an additional period of one "long" vector, the slab is then formed by partitioning this 'super'-unit cell into two contiguous regions: the 'filled' sites occuping one part and the 'empty' sites the remaining part. The layers comprising the filled sites, which ultimately contain the self-consistent potentials, are separated by the vacuum layers containing diffuse and extremely weak potentials. The surface is deemed to be isolated within the super-cell when the DOS for the vacuum region is negligable in comparison to the DOS for the filled region.

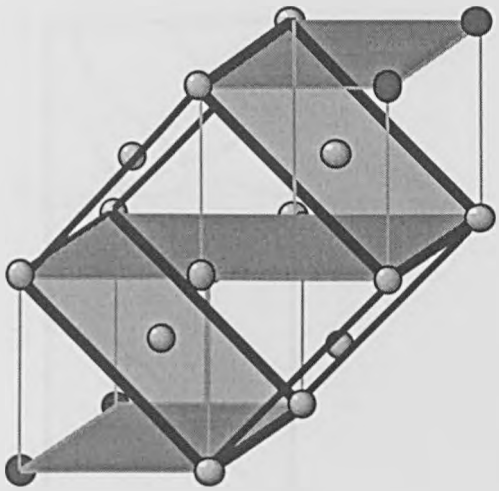

Figure 5.o, showing how W(110) forms the FCT unit cell in the slab geometry used for surface calculations.

The calculations used two different slab geometries in modelling the yttrium and the tungsten systems. The pure, unstrained yttrium used an HCP structure with the long vector on the c axis. The W(110) surface (see fig. 5.o, above) was modelled using a face-centred tetragonal (FCT)

unit cell, having the long vector oriented normal to the 110 direction.

The structures were initially calculated with the smallest number of vacuum layers needed to ensure self-consistency. The thickest slabs were, in fact, the first to be calculated. The thinner slabs resulted from replacing filled layers with vacuum layers, so that the size of the supercell was constant throughout.

5.6.1 Calculations for Y(0001)

The band structure for a single layer of yttrium, calculated using the bulk lattice value and ignoring possible relaxations, has been plotted along the ΓM direction (as shown in fig. 5.p, below). Because this system provides each atom with only 6 nearest neighbours, it is not surprising

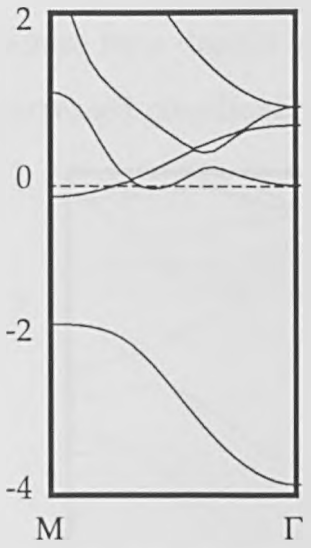

Figure 5.p. The single layer yttrium band structure

to discover that the band structure has narrowed in comparison with that of the bulk band structure. Also noteworthy is the absence of any occupied states at the Γ point and close to the Fermi level that can be identified with the ultra-thin film's surface state.

with the ultra-thin film's surface state.

The bulk band structure has been reproduced in fig. 5.q, below, for reference. The bulk yttrium structure has already been discussed in some detail (see section 5.2.3), and nothing further will be added here.

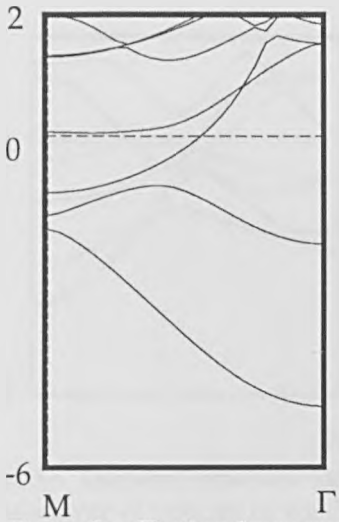

Figure 5.q. The band structure for bulk yttrium.

The band structure for a double layer of HCP yttrium is depicted in fig. 5.r, below. The increased coordination number for this system leads to

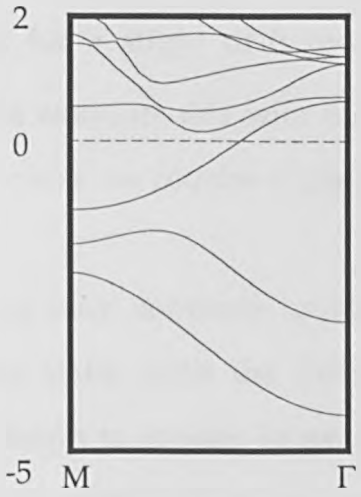

Figure 5.r. The double-layer yttrium band structure.

a broader valence band than that of the single-layered yttrium. A comparison with the bulk band structure (fig. 5.q) shows that the bands are also significantly more 'bulk-like' and have substantially more

It is interesting at this point to make a comparison between the 'unstrained' (HCP) yttrium and a 'strained' (FCT) single layer of yttrium (see fig. 5.s, below). The FCT yttrium shows once again a familiar narrowing of the valence band.

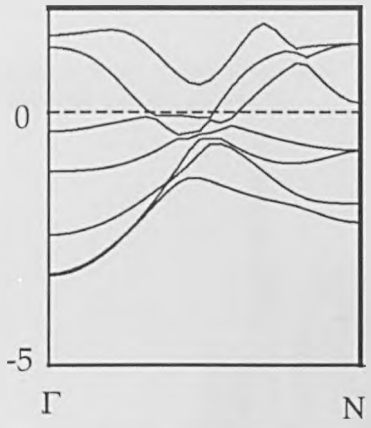

Figure 5.s. The band structure for 'strained' yttrium; a single layer of yttrium in the FCT lattice.

However, the band structure for FCT yttrium does show a far richer development of states than that of the yttrium HCP system. In particular, one state near the Fermi level shows very little dispersion along the first half of ΓM, except for a slight drift towards lower binding energies. However, we cannot associate this with the features at the Fermi level in the ARUPS data because we require a dispersion towards higher binding energies.

Evidently, we may continue looking at the band structures of increasingly thicker slabs, with the proviso that eventually bulk-like characteristics will begin to appear. In general, the development of states plotted within a band structure become more difficult to follow as the slab thickness increases. However, the onset of bulk-like states can be much more easily seen through the DOS rather than the band structure. For example, fig. 5.t (below) shows the favourable comparison between the local density of states (LDOS) from the centre of a six-layered HCP yttrium

slab and the density of states from bulk HCP yttrium, and we can conclude that a six-layered slab of yttrium suffices to calculate both surface and bulk properties.

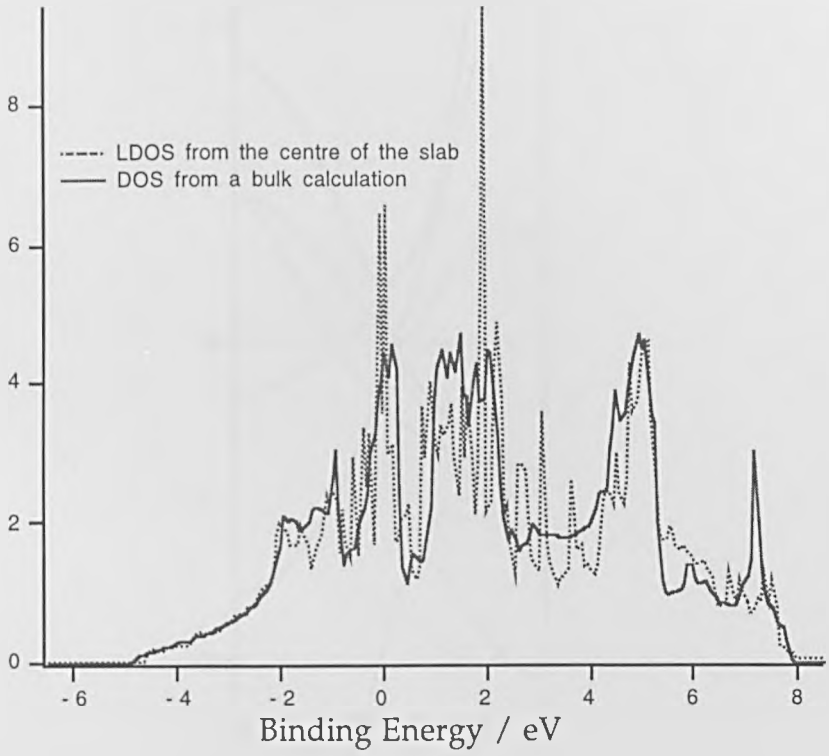

Figure 5. t. The similarities between the LDOS from the centre of a six-layered yttrium slab and the DOS from a bulk calculation.

5.6.2 Calculations for the W(110) surface.

It is, perhaps, a conceptual simplification to consider the presence on tungsten of a few monolayers of yttrium as equivalent to an immiscible tungsten-yttrium alloy, with the tungsten and yttrium possessing their own local density of states. Consequently, in anticipation of the calculated properties of the alloy structures, it will be helpful to examine the pure W(110) surface. The calculations have assumed bulk values for the lattice spacing and therefore no relaxation at the surface is considered.

Figure 5.u (below) shows the single-layer band structure calculation for tungsten, which displays the usual narrowing of the valence band.

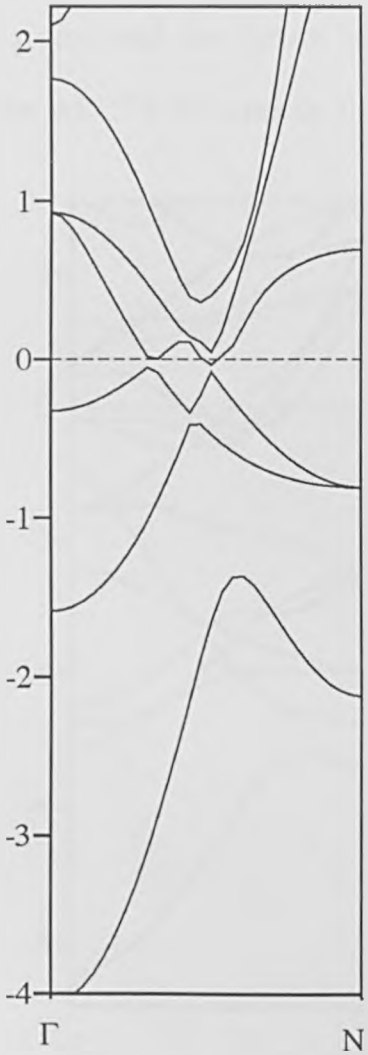

Figure 5.u. The band structure for a single layer of tungsten in the W(110) lattice.

Aside from the apparent degeneracy of the tungsten bands, a comparison with the single-layer FCT yttrium band structure (fig. 5.s) shows some interesting similarities in form, the most noteworthy being the state at the Γ point beneath the Fermi level which disperses weakly to a lower binding energy.

The band structure from a three-layered tungsten slab is shown in figure 5.v (below), and has twice the width of the valence band of the

single layer. Perhaps the most interesting aspect of this structure is the wealth of states between the Fermi level and - 5 eV, which disperse to both higher and lower energies from Γ to N. Amongst these, there are states close to the Γ point and the Fermi level which have the correct dispersive form for the ARUPS features in the ultra-thin film.

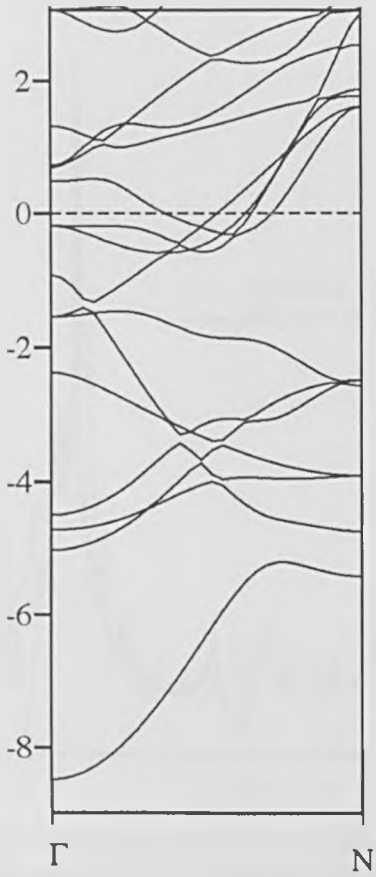

Figure 5.v. The band structure for a three-layered slab of tungsten in the FCT lattice.

5.6.3 Calculations for Y/W(110)

We have already remarked on the ultra-thin film system as being essentially an immiscible alloy. It will be helpful for the analysis of the ultra-thin film ARUPS data to examine the LDOS for the yttrium and tungsten in two different FCT slab configurations. The thicker slab comprises five filled layers having a Y-W1-W-W1-Y ordering, where W and W1 denote inequivalent lattice sites. The thinner slab is simply

ordered as Y-W-Y. Although these were not the only slab configurations calculated, they are the most relevant for this analysis.

Figures 5.w and 5.x (overleaf) show the LDOS for the central tungsten layer and the yttrium for the thicker slab. This slab, which is probably the more intuitive physical model, evidently shows too much tungsten character in the yttrium potentials at the edge of the slab.

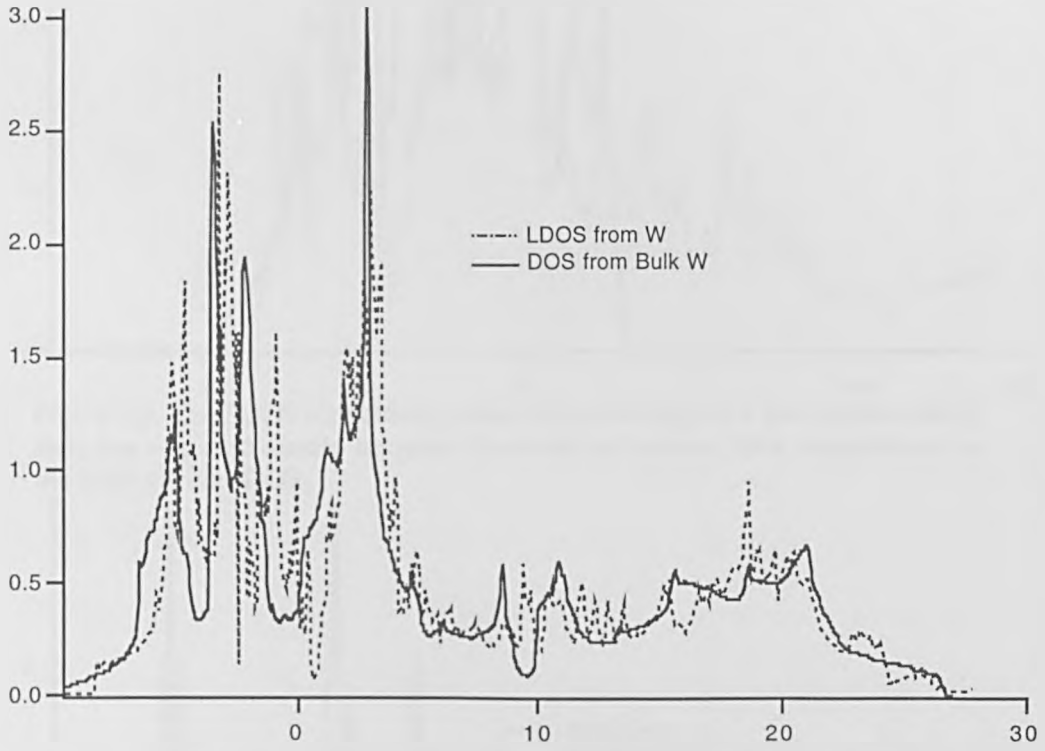

Figure 5.w. The LDOS for tungsten taken from the centre of a five-layered alloy slab compares favourably with the DOS from bulk tungsten.

The thinner (Y-W-Y) slab LDOS is shown in fig. 5.y, also overleaf, and displays a more amalgamated electronic structure; both yttrium and tungsten now share similar characteristics in their respective LDOS. The band structure for the Y-W-Y slab is shown in fig. 5.z (see page 110), and

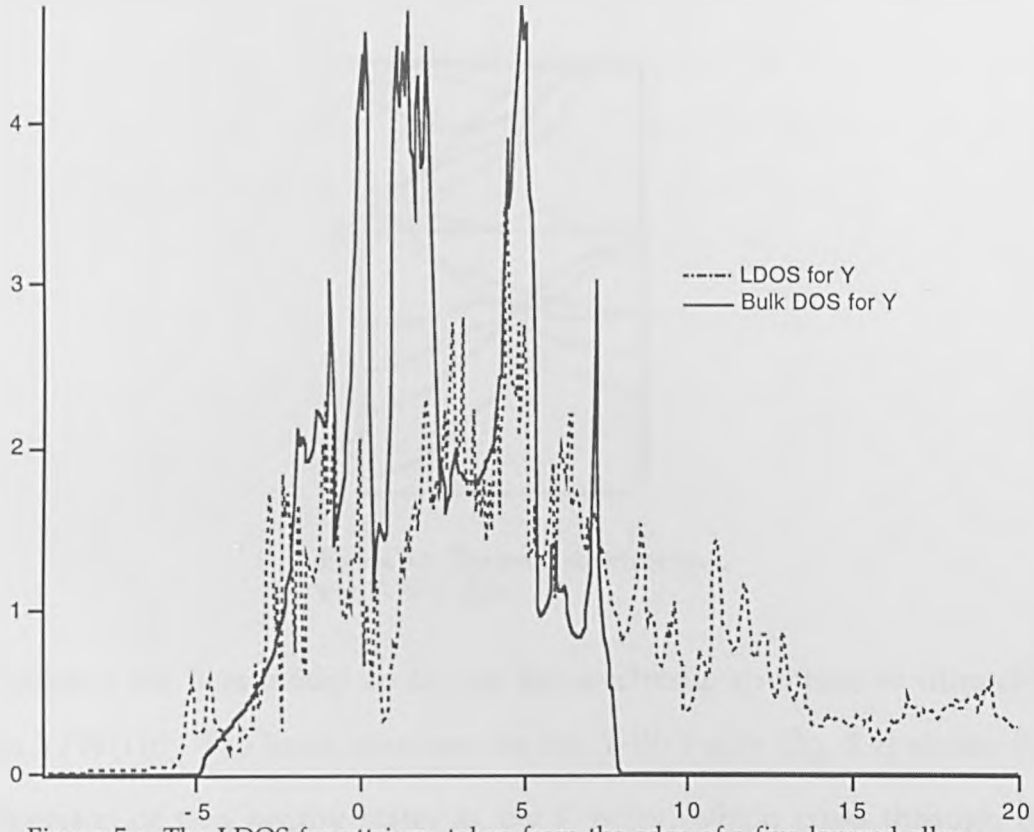

Figure 5.x. The LDOS for yttrium, taken from the edge of a five-layered alloy slab, has acquired mostly tungsten character and shows little resemblance to the bulk yttrium DOS.

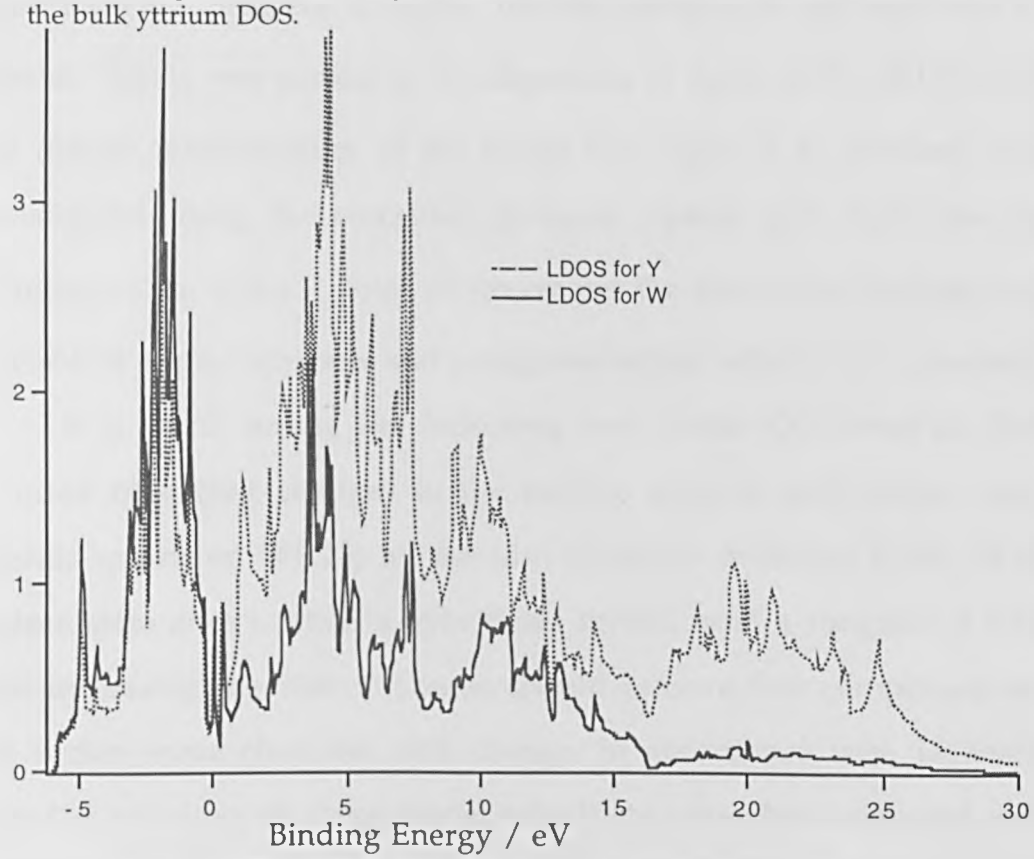

Figure 5.y. The Y-W-Y alloy slab shows a mixing of tungsten and yttrium characteristics in the LDOS.

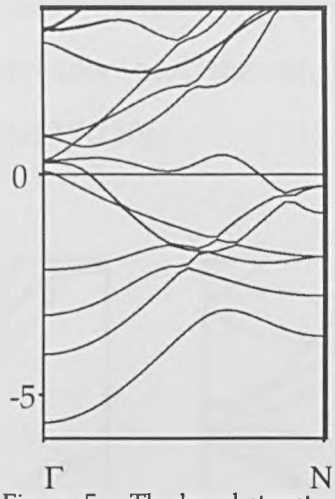

Figure 5.z. The band structure for the Y-W-Y slab.

represents the best model so far for the electronic structure of ultra-thin film Y/W(110). The band structure for the Y-W-Y slab (fig. 5.z) shows the dispersion of two nearby states at the Γ point, which cross through the Fermi level and progress to higher binding energies as they approach the N point. This is very similar to the dispersion of states in the ARUPS data. The orbital characteristics of the bands (see figure 5.A, overleaf) were investigated using the so-called 'fat-band' option and show that the prominent state at the Γ point which crosses the Fermi level derives from a hybrid of yttrium sp-states and a tungsten orbital with $(x^2 - y^2)$ symmetry.

It is worth noting the following two points. Dowben*et al.* have reported observing changes to the surface state of gadolinium single crystals grown on W(110) as the film thickness increases [5.34]. If the surface state does contain a hybridised orbital from a tungsten d-state, then increasing the film thickness should remove this component and the surface state character will change, in accordance with Dowben's report. Also, although these model calculations may be considered to be idealised, experiments investigating W-$f_{7/2}$ Auger decay channels [5.35]

have shown that the surface of W(110) permits decays more usually associated with the atomic state. Consequently, the surface is more 'atomic-like' than 'crystal-like' and the single-layer calculations above may be sufficient to model W(110).

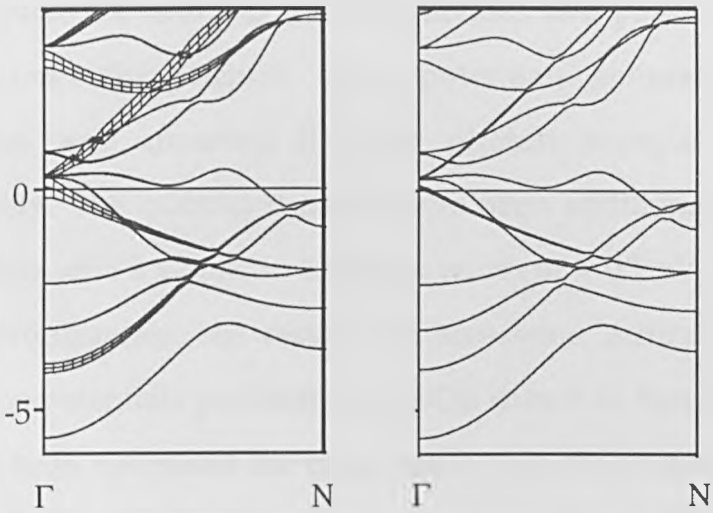

Figure 5.A. Plotting the orbital characteristics for the Y-W-Y slab shows that the Γ-point state at the Fermi level is hybridised, having the character mostly of yttrium sp-states (left) but also having the character of one of the tungsten states (right) with $(x^2 - y^2)$ symmetry.

5.7 Photocurrent Calculations

The photocurrent calculations presented below were performed using the scckkr code, written by Dr. A. Ernst at Daresbury Laboratory. Unfortunately, the code was still under development when the photocurrent calculations were being prepared, and a more complete suite of calculations could not be completed.

The calculation of a photocurrent using scckkr proceeds in two stages. First, supplying the input with structural information (unit cell dimensions and space group) and information on the atomic species allows the code to generate the necessary self-consistent potentials. The potentials can be checked for suitability through a DOS calculation. The potentials are then distributed throughout real-space in a crystalline

cluster. The real-space photocurrent equation (see section 4.6) can be calculated once additional information concerning the photon beam (energy, polarisation *etc.*) is supplied to the input. The calculations employ a final integration in the complex plane with a small imaginary component to the energy (~ 10^{-3} Rydbergs) to simulate spectral broadening.

Figures 5.C and 5.D (on the previous two pages) show calculated photocurrents for yttrium, using potentials generated from a bulk calculation and covering the two photon energies 33 and 40 eV respectively. The calculated peaks have been additionally broadened by convolution with a Gaussian having a width of ~ 0.1 eV.

Unfortunately, the results are somewhat difficult to understand, despite the potentials producing the DOS shown in figure 5. B below. The DOS has been optimised for calculations over the occupied states and so does not show the unoccupied states in any detail.

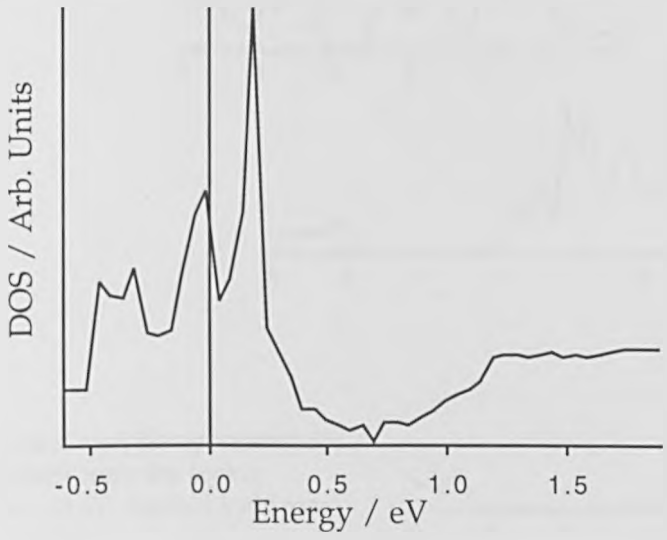

Figure 5.B. The DOS for yttrium, as calculated by the scckkr program.

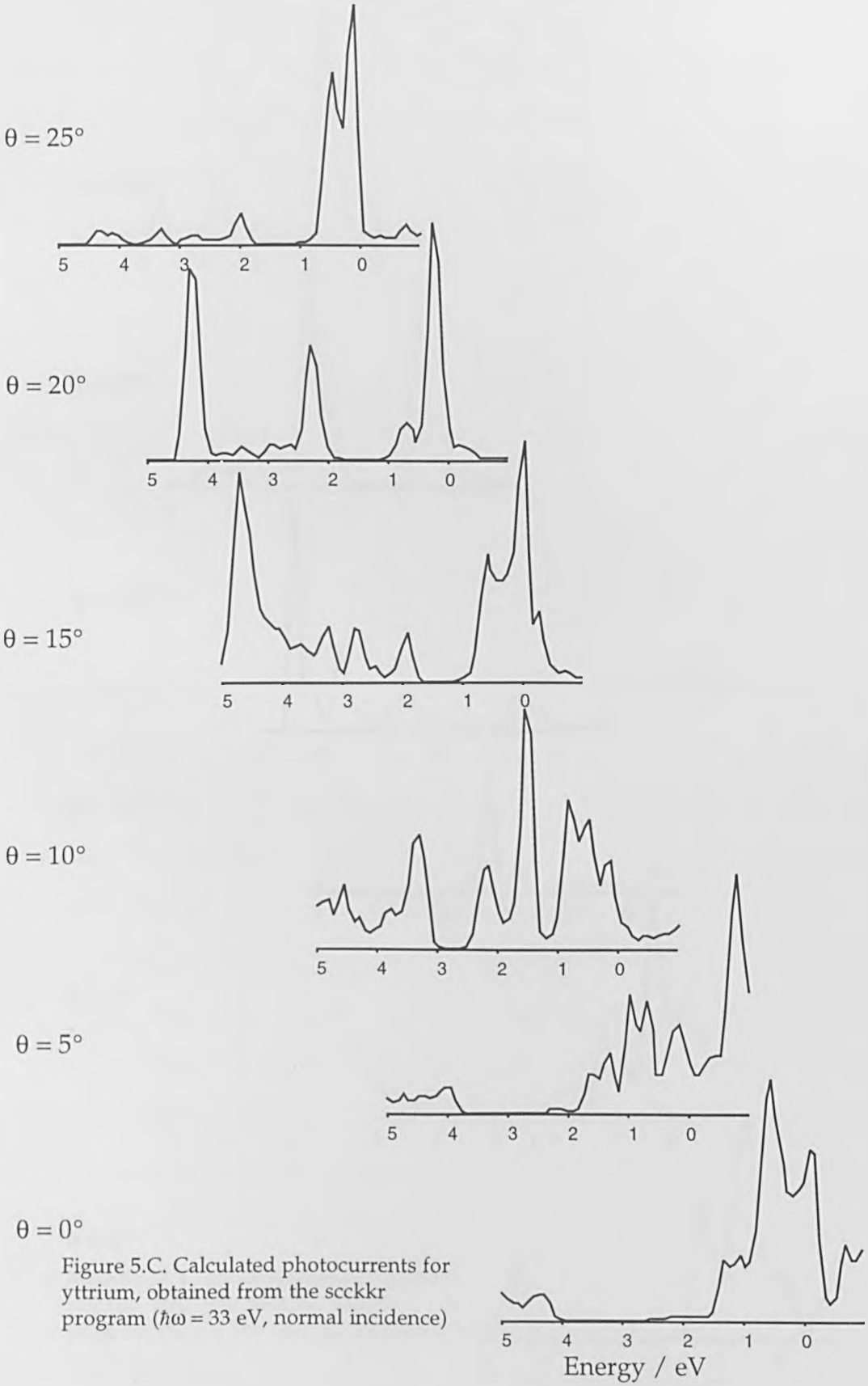

Figure 5.C. Calculated photocurrents for yttrium, obtained from the scckkr program ($\hbar\omega = 33$ eV, normal incidence)

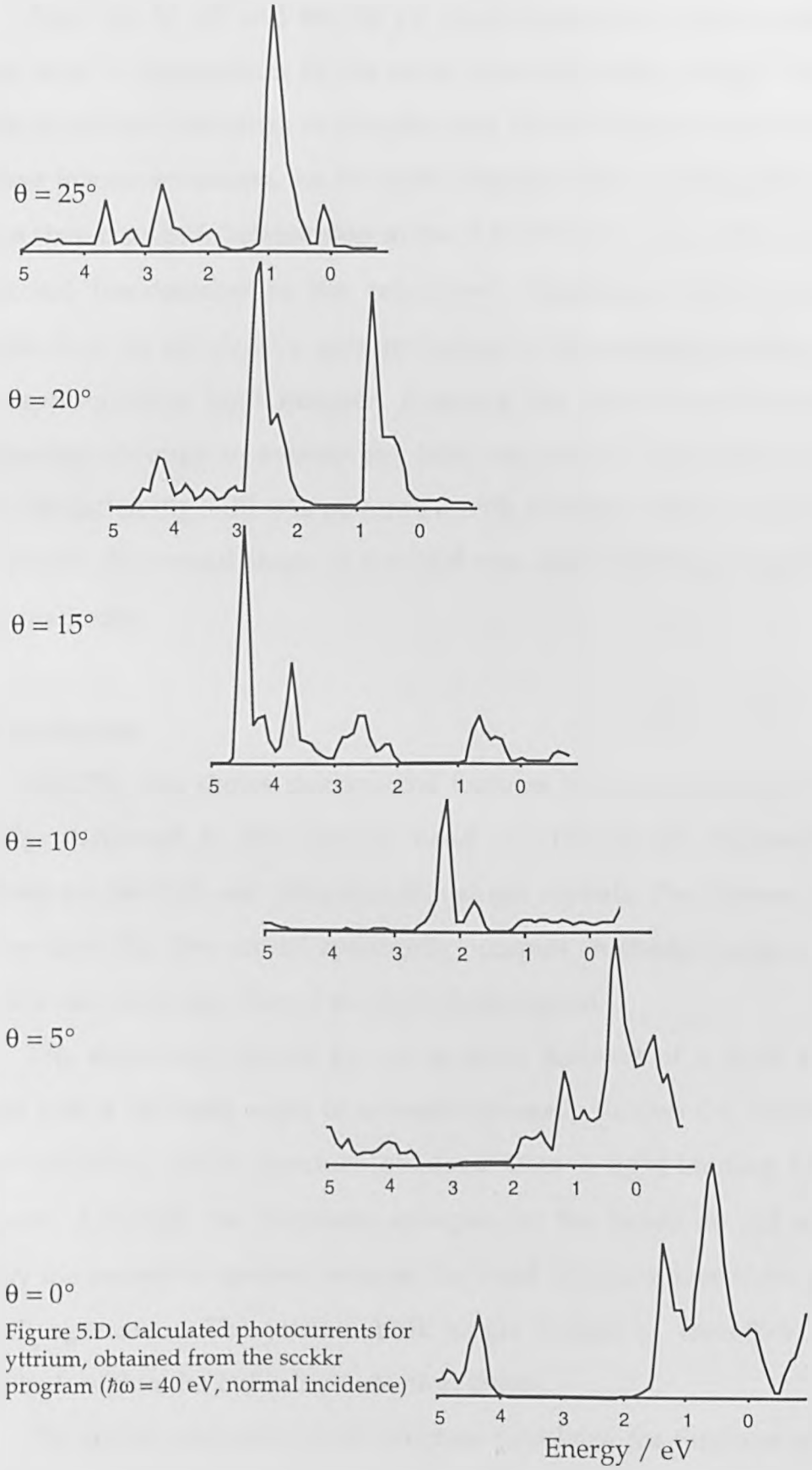

Figure 5.D. Calculated photocurrents for yttrium, obtained from the scckkr program ($\hbar\omega = 40$ eV, normal incidence)

Both the 33 eV and the 40 eV photocurrents on the preceeding pages show a suppression in the states over the energy range 2-4 eV, which is precisely the range of energies over which the bulk crystal shows its most intense emissions. As the states disperse with changing emission angles they bear little relationship to the ARUPS data - even allowing for numerical inaccuracies in the calculated intensities. It is, however, possible that the calculations were performed with the energy mesh set to an inappropriately high number, allowing too many inconsequential fluctuations through to swamp the final calculation. When the scckkr-DOS calculation (fig. 5.B) was performed with different numbers of energy grid points, the overall shape of the DOS was seen to change, sometimes quite markedly.

5.8 Conclusions

ARUPS data shows that spectral features within the energy range usually attributed to the valence band of yttrium are substantially different for the bulk and ultra-thin film single crystals. The valence band for the ultra-thin film crystal apparently occupies an energy range which is ~ 50% narrower than that of the bulk single crystal.

The dispersion shown by the spectral features of a bulk single crystal with a changing angle of emission generally follows the calculated scalar-relativistic band structure obtained from a tight-binding LMTO program. Although the calculated energies for the bands do not match exactly the measured spectral features, the band structure does show good overall agreement. The yttrium bulk single crystal is, therefore, well described within the bulk single-electron theory.

The scalar-relativistic band structure calculated for tungsten shows some discrepencies with fully-relativistic band structures previously

published, in that the band gap in the unoccupied states is not properly represented. The region of the occupied states probed by the photoemission experiments does, however, show dispersive characteristics with changing emission angle and these agree well with the general form of the scalar-relativistic band structure. Consequently, we can assert that the tungsten crystal in the direction ΓΣN is well described by the scalar-relativistic band structure, but we should not expect this to be the case across the entire Brillouin zone.

A series of surface band structure and LDOS calculations have been performed in an attempt to synthesise the electronic structure of the ultra-thin film. Yttrium slab calculations in the HCP symmetry and with increasing numbers of yttrium layers have failed to show any significant structure that can be allied with the dispersive behaviour of the ultra-thin film. In fact, the yttrium HCP slab calculations rapidly adopt a bulk-like electronic structure.

Within the symmetry constraints of the LMTO program, it was possible to estimate the effects of strain on the ultra-thin film by placing the yttrium in an FCT lattice. This band structure showed states within ΓΣN that had more of the dispersive character of the ultra-thin film than the HCP lattice, suggesting that strain may play an important part.

Immiscible alloys of tungsten and the yttrium in the FCT lattice were also investigated and showed that the presence of tungsten can force significant changes to the LDOS and to the development of the ΓΣN states. In particular, the LDOS for tungsten in the Y-W-Y slab shows a marked loss of unoccupied states, which may be attributed to a charge transfer from the yttrium and to the tungsten at the interface. Also, the band structure for the Y-W-Y slab possesses states that accord well with the

dispersive features in the ARUPS from ultra-thin film yttrium. One of these states has been examined to ascertain its orbital character, and has been shown to be due to mostly yttrium sp-states that have hybridised with a tungsten d-state having $(x^2 - y^2)$ symmetry.

Photocurrent calculations were also performed to investigate the effects of different photon energies on the emission features. The calculated photocurrents were, however, inconclusive.

We can conclude from these results that tungsten is not a passive substrate that simply supports a somewhat strained yttrium crystal but is, in fact, actively shaping the electronic structure of these ultra-thin films.

5.9 Directions for Future Work

The Rare Earth Group at Liverpool are currently planning a series of experiments on the growth of HCP rare earth ultra-thin films using the (112) surface of refractory metals. This follows a recently re-discovered paper by Du and Flynn [5.36] who claim to have grown $(10\bar{1}2)$ rare earths on W(112) without any lattice strain. Waldfried *et al.* [5.37] have also performed some initial studies on this system and suggest that the unstrained growth may only occur over a certain range of temperatures. If these studies prove to be reproducible, it may open a new field in the study of epitaxial rare earth systems. The prospect of calculating the electronic structure of an unstrained epitaxial lattice should also elucidate the role of the substrate in the complete alloyed electronic structure.

5.10 References

[5.1] T. L. Loucks, Phys. Rev., Vol. 144, 2, 504-511, (1966).

[5.2] P. G. Mattocks and R. C. Young, J. Phys. F. (Met. Phys.), Vol. 8, 1417-1426, (1978).

[5.3] S. D. Barrett and R. G. Jordan, Z. Phys. B - Condensed Matter, Vol. 66, 375-378, (1987).

[5.4] S. D. Barrett, Surface Science Reports, Volume 14, 7/8, 307-311, (1992) and references therein.

[5.5] R. I. R. Blyth, P. T. Andrews and S. D. Barrett, J. Phys.: Condens. Matter, Vol. 3, 2827-2831, (1991).

[5.6] P. Blaha, K. Schwarz, and P. H. Dederichs, Phys. Rev. B., Vol. 38, 9368-9374, (1988).

[5.7] R. I. R. Blyth, S. S. Dhesi, P.A. Gravil, R. Cosso, K. Newstead and S. D. Barrett, (unpublished).

[5.8] R. I. R. Blyth, Ph.D. Thesis, University of Liverpool, 1991.

[5.9] F. J. Himpsel and B. Reihl, Phys. Rev. B, Vol. 28, 574,(1983).

[5.10] D. A. Papaconstantopoulous, "Handbook of the Band Structures of the Elemental Solids", Plenum, New York, (1986).

[5.11] R. C. Young,J. Phys. (Paris) Colloq. 40, C5-71, (1979) and references therein.

[5.12] R. G. Jordan, Phys. Scr. T13, 22, (1986).

[5.13] A. J. Patchett, S. S. Dhesi, R. I. R. Blyth and S. D. Barrett, Surface Review and Letters, Vol. 1, 4, 649-653, (1994).

[5.14] S. D. Barrett, R. G. Jordan and A. M. Begley, J. Phys. F (Met.Phys.), Vol. 17., L145, (1987).

[5.15] R. G. White, Ph.D. Thesis, Chapter 7 and references therein, The University of Liverpool, (1996).

[5.16] F. P. Netzer and E. Bertel, in "Handbook on the physics and Chemistry of the Rare Earths", Vol. 5, Eds. K. A. Gschneider Jr., and L. Eyring, (North Holland, Amsterdam, 1982).

[5.17] D. Li, J. Zhang, P. A. Dowben, M. Onellion, Phys. Rev. B, Vol. 48, 5612, (1993).

[5.18] J. Osterwalder, Z. Phys. B - Condensed Matter, Vol. 61, 113-128, (1985).

[5.19] P. Vajda in "Handbook on the Physics and Chemistry of Rare Earths", Vol. 20, eds. K. A. Gschneider and L. Eyring, Elsevier, Amsterdam, (1995).

[5.20] B. Feuerbacher and B. Fitton, Phys. Rev. Lett., Vol. 29, 786, (1972).

[5.21] B. J. Waclawski and E. W. Plummer, Phys. Rev. Lett., Vol. 29, 783, (1972).

[5.22] L. Braicovich, M. Finazzi, Ch. Roth, F. U. Hillebrecht and E. Kisker, Sol. Stat. Comm.,Vol. 92, 3, 273-275, (1994).

[5.23] S. Raaen, C. Berg and N. A. Braaten, Surf. Sci., Vol. 269/270, 953-958, (1992).

[5.24] C. H. F. Peden and N. D. Shinn, Surf. Sci., Vol. 312, 151-156, (1994).

[5.25] M. W. Holmes and D. A. King, Proc. R. Soc. Lond. , Vol. A 376, 565-583, (1981).

[5.26] R. I. R. Blyth, M. H. Lee, C. Searle, N. P. Tucker, R. G. White and S. D. Barrett, (unpublished).

[5.27] D. M. Bylander and L. Kleinman, Phys. Rev. B., Vol. 29, 4, 1534-1539, (1984).

[5.28] B. Feuerbacher and N. E. Christensen, Phys. Rev. B, Vol. 10, 2373, (1974).

[5.29] I. R. Collins, A. D. Laine, P. T. Andrews and P. J. Durham, J. Phys.: Condens. Matter, Vol. 3, 5307-5321, (1991).

[5.30] P. A. Dowben, D. N. McIlroy and Dongqi Li, Handbook on the Physics and Chemistry of Rare Earths, Vol.24, eds. K. A. Gschneider and L. Eyring, North-Holland, Amsterdam, (1996).

[5.31] V. R. Dhanak and D. W. Bassett, J. Phys.: Condens. Matter, Vol. 3, 1505-1515, (1991).

[5.32] P. A. Dowben, D. LaGraffe and M. Onnelion, J. Phys. Condens. Matter, 6571, (1989).

[5.33] G. E. Rhead, M-G. Barthés and C. Argile, Thin Solid Films, Vol. 82, 201, (1981).

[5.34] D. Li, C. W. Hutchings, P. A. Dowben, C. Hwang, R. T. Wu, M. Onellion, B. Andrews and J. L. Erskine, J. Magn & Magn. Mat., Vol.99, 85,

(1991).

[5.35] D. M. Riffe, G. K. Wertheim and P. H. Citrin, Phys. Rev. Lett., Vol. 63, 18, 1976-1979, (1989).

[5.36] R. Du and C. P. Flynn, J. Phys.: Condens. Matter, Vol.2, 1335-1341, (1990).

[5.37] C. Waldfreid, O. Zeybek, T. Bertrams, S. D. Barrett and P. A. Dowben, Mat. Res. Soc. Symp. Proc., Vol.528, 147-151, (1998)